TWO MECHANISMS OF VORTICITY GENERATION IN COMBUSTING FLOW FIELDS

Thesis by

Gavin Julian Hendricks

In Partial Fulfillment of the

Requirements for the Degree of

Doctor of Philosophy

California Institute of Technology

Pasadena, California

1986

Submitted May 23, 1986

Acknowledgements

I wish to express my sincere appreciation to my advisor, Professor F.E. Marble for his guidance and inspiration throughout the course of my graduate studies. In addition, I am grateful for the illuminating discussions with Professor T. Kubota and the helpful comments of Professor E.E. Zukoski.

Discussions with Mr. J. Sterling also helped to clarify some ideas on my research work. Sincere thanks also to Dr. E. Baum for the use of the computational code which initiated the work discussed in Part 2 of the thesis.

I would like to express a special word of thanks to my parents for their moral support and encouragement. The support of my roommates and the words of encouragement from Ms. D. Eckerman were also appreciated.

My graduate studies were made possible by a Fulbright Scholarship, a Charles Lee Powel Fellowship as well as support from the California Institute of Technology. The research was supported by AFSOR Grant 84–0286.

Abstract

In Part 1 of the thesis the behavior of a diffusion flame in an unbounded flow with an imposed pressure gradient is analysed. The problem is formulated using the compressible boundary layer equations, and the assumption of infinite reaction kinetics is employed. The equations are transformed to the equivalent incompressible equations by the application of the Howarth transformation. Solutions to these equations are obtained for a functional form of the pressure gradient which admits similarity solutions. Two stoichiometric fuel–air ratios are considered, $\varphi = 1$ which yields a symmetric flow field about the flame, and $\varphi = 0.058$ which corresponds to the combustion of methane in air and yields an unsymmetric flow field.

For favorable pressure gradients the fluid in the vicinity of the flame is accelerated more than the fluid in the free stream. The acceleration of the fluid as it is convected downstream causes an augmentation in the fuel mass consumption rate, the mechanism of which is similar to that of a strained diffusion flame in an unbounded counterflow. For adverse pressure gradients a reverse flow develops in the vicinity of the flame which severely affects the mass consumption rate of fuel. For a flame with unit stoichiometry, recirculation zones develop on either side of the flame which eventually lead to extinction. For the stoichiometric ratio corresponding to the combustion of methane in air, the recirculation zones are situated on the fuel side of the flame and no tendency toward extinction is shown.

In Part 2 a numerical study is done to investigate the formation of large vortex structures observed in the combustion chambers of air breathing engines under certain conditions. It has been proposed that these vortex structures are formed by a surging flow over the flameholding device which exists when longitudinal modes of the combustion system are excited. In the present study the surging flow is generated by passing a weak shock wave over a rearward facing step. The fluid entering the chamber is of high

density (representing the cold fuel–air mixture) whereas the fluid in the chamber has a low density (the combustion products). The vortex formed by the surging flow induces a downward velocity in the high density fluid toward the lower wall. It is found that larger surge velocities result in the formation of stronger vortices (which induce higher downward velocities), whereas an increase in the mean velocity causes no significant change in the flow field. The time taken for the high density fluid to reach the lower wall is therefore decreased as the surge velocity is increased. By considering these results, a possible model for the sustenance of the vortex shedding mechanism is proposed.

Contents

List of Figures

Part 1

List of Tables

List of Symbols

Part 1

Symbol	Description
$A(x)$	Channel area for the outer flow field.
$A_t(x)$	Channel area for the flow field.
c_p	Specific heat at constant pressure.
D	Binary mass diffusion coefficient.
D_0	Binary mass diffusion coefficient at temperature T_0.
$f(\eta)$	Similarity stream function.
F	One mole of fuel.
$h(t)$	$\left(1 - \frac{\beta - 1}{\lambda} f'(0)\, u_0 \left(\frac{x_0}{\lambda}\right)^{\beta - 1} t\right)$.
k	Thermal conductivity.
k_0	Thermal conductivity at temperature t_0.
Le	Lewis number.
$\dot{m}$	Mass consumption rate.
$\dot{m}_f$	Fuel mass consumption rate for a diffusion flame in a pressure gradient.
$\dot{m}_{\varepsilon_0}$	Fuel mass consumption rate for a diffusion flame undergoing a constant strain rate.
$\dot{m}_{str}$	Fuel mass consumption rate for a diffusion flame undergoing an arbitrary strain rate.
O	One mole of oxidizer.
P	One mole of product.
Pr	Prandtl number.
Q	Heat released by the reaction of one mole of fuel.
q	Heat released per unit mass of fuel.
Sc	Schmidt number.

t	Time.
T	Temperature.
T_0	Temperature in the far field.
T_f	Flame temperature.
u	Horizontal velocity.
u_0	Horizontal scale velocity.
$\overline{u}$	Horizontal velocity after Howarth transformation.
u_e	Horizontal velocity of a flame element.
u_f	Horizontal velocity at the flame.
x	Horizontal spatial coordinate.
x_0	Initial position of a flame element.
$\overline{x}$	Horizontal spatial coordinate after Howarth transformation.
x_e	Position of a flame element.
y	Vertical spatial coordinate.
$\overline{y}$	Vertical spatial coordinate after Howarth transformation.
β	Velocity index.
β_{min}	Minimum value of the velocity index.
δ^*	Displacement thickness.
ε	Strain rate.
ε_0	Constant strain rate.
η	Similarity variable.
η_f	Value of the similarity variable at the flame.
ϑ	Non–dimensional temperature.
K	Mass fraction.
K_1	Mass fraction of fuel.
K_2	Mass fraction of oxidizer.
λ	Horizontal length scale.

μ Dynamic viscosity.

μ_0 Dynamic viscosity at temperature T_0.

ν Kinematic viscosity.

ν_0 Kinematic viscosity at temperature T_0.

ρ Fluid density.

ρ_0 Fluid density at temperature T_0.

τ $\displaystyle\int_0^t \left(e^{2\int_0^{t_2} \varepsilon(t_1)dt_1} \right) dt_2$

ϕ Moles of oxidizer consumed by the reaction of one mole of fuel.

φ Stoiciometric fuel–air ratio.

χ Moles of product produced by the reaction of one mole of fuel.

ψ Stream function.

Part 2

c_0 Speed of sound in the high density fluid.

e Energy per unit mass.

l Scale length.

l^* Position of the lower extremity of the high density fluid.

P Pressure.

t Time.

u Horizontal velocity.

u_n Velocity normal to a boundary.

v Vertical velocity.

v^* Vertical velocity of the lower extremity of the high density fluid.

x Horizontal spatial coordinate.

y Vertical spatial coordinate.

γ Ratio of specific heats.

ρ Density

Superscript

–	Non–dimensionalized quantities.

Subscripts

0	Conditions in the high density fluid ahead of the shock wave.
1	Conditions in the high density fluid behind the shock wave.
2	Conditions in the low density fluid.

Part 1

The Behavior of a Diffusion Flame in a Pressure Gradient.

Chapter 1

Introduction

The analytical study of combusting flow fields is complicated by the complex interaction which exists between the fluid mechanics of the flow field under consideration, and the chemistry of the reaction in the combustion zones of the flow field. For a certain class of combusting flow fields, one in which the reactants are initially unmixed, Burke and Schumann (1928) recognized the important fact that the diffusion of reactants toward the combustion zone is much more important than the chemical reaction in determining the rate of the combustion process and hence its effect on the flow field. This implies that the reaction rate can be assumed infinite, the rate of combustion of the reactants being determined entirely by their transport towards the reaction zone by the diffusion process. A further implication is that the reaction zone is limited to a zone of infinitesmal thickness. By employing this assumption in the formulation of combustion problems in which the reactants are initially unmixed, the details of the chemical reaction are effectively decoupled from the fluid mechanics. The details of the chemical reaction become important only when the time scale associated with the transport of reactants toward the flame zone is of the same order of magnitude as that associated with the chemical reaction.

By utilizing the thin flame, infinite reaction rate model, relatively complex flow fields involving combustion can be studied. An example is the buoyant diffusion flame which has been extensively studied. A brief literature survey on this problem appears in Chapter 2. Most of the analytical effort, however, has gone into the study of the time dependent, strained diffusion flame in an unbounded counterflow. This problem has been studied extensively, not only in the limit of infinite reaction rates, but also in cases where reaction rates are important (eg. high straining rates). Apart from being of interest as a combustion problem in its own right, it forms a building block for more

for more complicated, turbulent combusting flow fields. This has resulted from the experimental observation that turbulent flames consist of a collection of laminar flame surfaces in which the laminar flame structure retains its identity, but is severely strained and distorted by the turbulent fluid motion. This idea is employed, and the results of the strained diffusion flame analysis utilized in the studies of turbulent diffusion flames by Carrier, Fendell and Marble (1975), Bush, Feldman and Fendell (1976) and Marble and Broadwell (1977). The results of the strained diffusion flame are also used by Karagozian (1982) in the analysis of combustion in vortex structures. In these studies the effects of pressure gradients which exist in the flow field are not taken into account.

In the present study an attempt is made to gain some insight into the effect that pressure gradients, aligned with the flame zone, have on the behavior of diffusion flames. Because the density gradient (resulting from the temperature gradient) is perpendicular to the flame and therefore to the pressure gradient, a powerful mechanism for the production of vorticity exists in the flow field. This mechanism, described by the Helmholtz vorticity equation, results in a rate of vorticity production within an element of fluid proportional to $\nabla\rho \times \nabla p$. The vorticity created in this manner can be a major contributing factor to the transition of a flow field from laminar to turbulent, or, in a turbulent combusting flow field, can lead to an augmentation in the degree of turbulence existing in the flow field.

In Chapter 2 the problem is formulated utilizing the thin flame, infinite reaction rate model. The partial differential equations describing the flow field are reduced to ordinary differential equations by using a functional form for the pressure gradient that yields similarity solutions. The numerical method used to solved the ordinary differential equations generated by the analysis is also outlined in this chapter. Two stoichiometric fuel–air ratios are considered; a ratio of 1 which generates a symmetric flow field about the flame, and a ratio of 0.058, corresponding to the combustion of methane in air, which

yields an unsymmetric flow field.

The solutions to the equations can be divided into two classes, those which correspond to favorable pressure gradients (and therefore accelerating flow fields) and those which correspond to adverse pressure gradients (decelerating flow fields). The solutions corresponding to favorable pressure gradients are discussed in Chapter 3. Because the solutions show a similarity to those produced by the analysis of the strained diffusion flame in an unbounded counterflow, a comparative study of the results produced by the two situations is done. In Chapter 4 the results corresponding to adverse pressure gradients are discussed. In this case the two stoichiometric ratios considered produce results which differ markedly, and yield fuel mass consumption rates which show a qualitative difference in behavior as the pressure gradient is varied.

Chapter 2

Mathematical Formulation

The bouyant diffusion flame, a problem related qualitatively to the diffusion flame in a pressure gradient, has been the subject of intensive study. Kosdon, Williams and Buman (1969) initiated these studies with their investigation of the combustion of vertical cellulosic cylinders in air. Kim, De Ris and Kroesser (1971) followed up on this analysis with their treatment of vertical, inclined and horizontal burning fuel surfaces.

Various other aspects of bouyant diffusion flames were considered in subsequent studies. The overfire region above burning surfaces was studied by Pagni and Shih (1977), Ahmad and Faeth (1978), and Groff and Faeth (1978) using various methods of solution for the field equations. Kinoshita and Pagni (1980) studied forced, free, and mixed mode diffusion flames adjacent to finite fuel slabs. The structure and stability of bouyant diffusion flames was studied for various fuel–air combinations by Fleming (1982).

All of the above analyses utilized the assumption of infinite chemical reaction rates introduced by Burke and Schumann (1928). Unit Lewis number and transport properties independent of composition were also assumed in these calculations. Despite these assumptions the analyses produced results that compared favorably with experiments. The above assumptions led to significant simplifications in the mathematical formulation of the field equations and are thus employed in the present analysis.

As in the study of buoyant flames, the present analysis follows three steps. The boundary layer field equations are transformed to a set of equivalent constant density equations by the use of the Howarth transformation (1948). The equations obtained admit similarity solutions for a certain functional form of the pressure gradient. The equations are then transformed using a similarity transformation which, in this case, resembles that of Falkner and Skan (1931) in their treatment of boundary layers sub-

ject to pressure gradients. The similarity transformation yields two coupled, nonlinear differential equations with boundary conditions specified at three points. This three point boundary value problem is solved using a shooting method which has been used extensively for the solution of boundary layer problems.

2.1 The Governing Field Equations

Consider a flow nearly parallel to the horizontal x-axis, the upper half-plane consisting of a fuel, the lower of oxidizer. Further, let the gas velocity in the far field of each stream be $u_1(x)$, and the density constant, uniform, and equal to ρ_0. Because the undisturbed far field flow is assumed to be irrotational, the Bernoulli equation

$$p + \tfrac{1}{2}\rho_0 {u_1}^2(x) = c \tag{2.1}$$

holds. The pressure in the far field is therefore dependent only on x and the pressure gradient is given by

$$\frac{\partial p}{\partial x} = -\rho_0 u_1 \frac{du_1}{dx} \quad . \tag{2.2}$$

Now let the two streams interact at the interface between the fuel and oxidizer (located at $y = 0$) as a diffusion flame with infinitely fast kinetics. The chemical reactions are therefore confined to a sheet of negligible thickness. If we assume that the effect of the chemical reaction is confined to a thin region around the flame, the flow field is well described using the boundary layer approximation and is governed by the field equations:

$$\frac{\partial \rho u}{\partial x} + \frac{\partial \rho v}{\partial y} = 0 \tag{2.3}$$

$$\rho u \frac{\partial u}{\partial x} + \rho v \frac{\partial v}{\partial y} = -\frac{\partial p}{\partial x} + \frac{\partial}{\partial y}\left(\mu \frac{\partial u}{\partial y}\right) \tag{2.4}$$

where $\dfrac{\partial p}{\partial x}$ is given by (2.2).

The chemical reaction is given by:

$$F + \phi O \rightarrow \chi P + Q \tag{2.5}$$

where F, O, and P represent one mole each of fuel, oxidizer and product. ϕ Represents the number of moles of oxidizer consumed by one mole of fuel and χ represents the number of moles of product generated by the reaction. Q represents the amount of heat produced by the reaction.

In cases of non-unit stoichiometry, the flame sheet will be situated in the lower half plane for the stoichiometric fuel–air ratio $\varphi < 1$, and in the upper half plane for $\varphi > 1$. In order to make the problem more tractable mathematically, we locate the flame sheet along the x–axis, effectively imposing an artificial vertical velocity on the flow field.

Because of the infinitely fast chemistry, the two reactants cannot coexist and, moreover, must both vanish at the flame front. It is also, therefore, not possible for the reactants to cross the flame front. As a result, the fuel, of mass fraction K_1, is contained in the upper half plane whereas the oxidizer, of mass fraction K_2, is contained in the lower half plane. The entire region of chemical reaction is confined to the horizontal axis so that species concentrations in both the upper and lower half planes are described by concentration relations with no production terms:

$$\rho u \frac{\partial K_{1,2}}{\partial x} + \rho v \frac{\partial K_{1,2}}{\partial y} = \frac{\partial}{\partial y}\left(\rho D \frac{\partial K_{1,2}}{\partial y}\right) \tag{2.6}$$

where D is the molecular diffusivity.

In each region the remaining gas mass fraction consists of combustion products. Similarly the conservation of enthalpy:

$$\rho u c_p \frac{\partial T}{\partial x} + \rho v c_p \frac{\partial T}{\partial y} = \frac{\partial}{\partial y}\left(k \frac{\partial T}{\partial y}\right) \tag{2.7}$$

holds everywhere except at the flame on the horizontal axis where a heat source due to the chemical reaction exists. In the above equation k is the thermal conductivity and c_p is the specific heat at constant pressure which is assumed to be constant.

The conditions in the far field for the reactant concentrations and the gas temper-

atures are

$$K_1(x,\infty) = K_2(x,-\infty) = 1 \tag{2.8}$$

and

$$T(x,\infty) = T(x,-\infty) = T_0 \quad . \tag{2.9}$$

The species and temperature functions are analytic in the upper and lower half planes, but discontinuities may occur in the slopes of these functions at the flame sheet due to the consumption of reactants and the subsequent heat release. The chemical reaction provides the conditions for matching the analytic functions for temperature and species at the flame sheet. In addition to the conditions

$$K_1(x,0) = K_2(x,0) = 0 \quad , \tag{2.10}$$

it is required that the two reactants be transported to the flame zone in the stoichiometric ratio φ. The bulk velocity through the flame cannot contribute to the net transport of reactants because the concentrations of both reactants must vanish at the flame, and therefore the species transport to the flame is due entirely to diffusion. This condition gives

$$\frac{\partial K_1}{\partial y}(x,0^+) = -\varphi \frac{\partial K_2}{\partial y}(x,0^-) \quad . \tag{2.11}$$

The sensible heat released by the chemical reaction has to be conducted into the upper and lower gas regions, the bulk velocity through the flame again making no contribution because the temperature is continuous at the flame. This gives

$$-k\frac{\partial T}{\partial y}(x,0^+) + k\frac{\partial T}{\partial y}(x,0_-) = q\left[\rho D \frac{\partial K_1}{\partial y}(x,0^+)\right] \tag{2.12}$$

where q is the heat of reaction per unit mass of fuel.

Because the pressure variations in the x-direction are assumed to be small, the equation of state for the gas is

$$\rho T = \rho_0 T_0 \quad . \tag{2.13}$$

2.2 The Howarth Transformation

Due to the heat release at the flame, large density variations are expected in the vicinity of the flame. Since the incompressible boundary layer equations are easier to solve, it is desirable to relate the equations in **2.1** to the equivalent incompressible boundary layer equations. This is accomplished by the use of the Howarth transformation which introduces a new vertical length scale

$$\overline{y} = \int_0^y \left(\frac{\rho}{\rho_0}\right) dy \tag{2.14}$$

while retaining the original horizontal scale

$$\overline{x} = x \quad . \tag{2.15}$$

Under this transformation the horizontal velocity component remains unchanged

$$\overline{u} = u \quad , \tag{2.16}$$

but the vertical velocity component is transformed to

$$\overline{v} = \left(\frac{\rho}{\rho_0}\right) v + u \int_0^y \frac{\partial}{\partial x}\left(\frac{\rho}{\rho_0}\right) dy \quad . \tag{2.17}$$

As is common in combustion analyses, the following approximations for the variation of viscosity, thermal conductivity, and molecular diffusivity are made when applying the Howarth transformation to the boundary layer equations:

$$\rho\mu = \rho_0\mu_0 \quad , \qquad \rho k = \rho_0 k_0 \quad , \qquad \rho^2 D = {\rho_0}^2 {D_0}^2 \quad . \tag{2.18}$$

After application of the Howarth transformation and the incorporation of the equation of state (2.13) into the momentum equation, equations (2.3),(2.4),(2.7), and (2.8) reduce to:

$$\frac{\partial \overline{u}}{\partial \overline{x}} + \frac{\partial \overline{v}}{\partial \overline{y}} = 0 \tag{2.19}$$

$$\overline{u}\frac{\partial \overline{u}}{\partial \overline{x}} + \overline{v}\frac{\partial \overline{u}}{\partial \overline{y}} = \frac{T}{T_0}u_1\frac{du_1}{dx} + \nu_0\frac{\partial^2 \overline{u}}{\partial \overline{y}^2} \tag{2.20}$$

$$\overline{u}\frac{\partial K_{1,2}}{\partial \overline{x}} + \overline{v}\frac{\partial K_{1,2}}{\partial \overline{y}} = D_0\frac{\partial^2 K_{1,2}}{\partial \overline{y}^2} \tag{2.21}$$

$$\overline{u}\frac{\partial T}{\partial \overline{x}} + \overline{v}\frac{\partial T}{\partial \overline{y}} = \frac{\nu_0}{Pr}\frac{\partial^2 T}{\partial \overline{y}^2} \tag{2.22}$$

where

$$Pr = \frac{c_p\mu_0}{k_0} \quad . \tag{2.23}$$

The above equations are identical to the constant density boundary layer equations except for the coupling that exists between the momentum and temperature equations, which is responsible for the vorticity generation in the flow field.

It will be shown that the flame temperature is constant, which makes convenient to introduce a dimensionless temperature variable

$$\vartheta = \frac{T - T_0}{T_f - T_0} \tag{2.24}$$

which satisfies the differential equation

$$\overline{u}\frac{\partial \vartheta}{\partial \overline{x}} + \overline{v}\frac{\partial \vartheta}{\partial \overline{y}} = \frac{\nu_0}{Pr}\frac{\partial^2 \vartheta}{\partial \overline{y}^2} \tag{2.25}$$

with boundary conditions

$$\vartheta(\overline{x},\infty) = \vartheta(\overline{x},-\infty) = 0 \quad , \qquad \vartheta(\overline{x},o) = 1 \quad . \tag{2.26}$$

After the application of the Howarth transformation, the matching conditions (2.11), (2.12) become

$$\frac{\partial K_1}{\partial \overline{y}}(\overline{x},0^+) = -\varphi\frac{\partial K_2}{\partial \overline{y}}(\overline{x},0^-) \tag{2.27}$$

$$-\frac{\partial \vartheta}{\partial \overline{y}}(\overline{x},0^+) + \frac{\partial \vartheta}{\partial \overline{y}}(\overline{x},0^-) = \frac{\left(\frac{q}{c_pT_0}\right)\left(\frac{\rho_0 c_p D_0}{k_0}\right)\frac{\partial K_1}{\partial \overline{y}}(\overline{x},0^+)}{\left(\frac{T_f}{T_0} - 1\right)} \quad . \tag{2.28}$$

In the subsequent calculations it will be assumed that

$$Le = \frac{Pr}{Sc} = 1 \tag{2.29}$$

which holds for most gases. This leads to a significant simplification in the solution of the problem since the species and normalized temperature variables are described by the same differential equation. Because K_1 and K_2 are defined in different planes, a single function

$$K = \begin{cases} K_1 & \overline{y} > 0 \\ K_2 & \overline{y} < 0 \end{cases} \tag{2.30}$$

can be used to describe the gas composition over the entire plane. The functions ϑ and $(1 - K)$ satisfy the same differential equation and have the same boundary conditions, so they must have the same solution. This reduces the number of differential equations to be solved from four to three. The matching conditions (2.27) and (2.28) thus become

$$\frac{\partial \vartheta}{\partial \overline{y}}(\overline{x}, 0^+) = -\varphi \frac{\partial \vartheta}{\partial \overline{y}}(\overline{x}, 0^-) \tag{2.31}$$

and

$$\begin{aligned} \left(\frac{T_f}{T_0} - 1\right) &= \frac{\dfrac{q}{c_p T_0} \dfrac{\partial K_1}{\partial \overline{y}}(\overline{x}, 0^+)}{\dfrac{\partial \vartheta}{\partial \overline{y}}(\overline{x}, 0^-) - \dfrac{\partial \vartheta}{\partial \overline{y}}(\overline{x}, 0^+)} \\ &= \frac{\dfrac{q}{c_p T_0} \varphi}{1 + \varphi} \end{aligned} \tag{2.32}$$

which is constant.

The system of equations to be solved is therefore

$$\frac{\partial \overline{u}}{\partial \overline{x}} + \frac{\partial \overline{v}}{\partial \overline{y}} = 0 \tag{2.33}$$

$$\overline{u} \frac{\partial \overline{u}}{\partial \overline{x}} + \overline{v} \frac{\partial \overline{v}}{\partial \overline{y}} = \left[\left(\frac{T_f}{T_0} - 1\right) \vartheta + 1\right] u_1 \frac{du_1}{d\overline{x}} + \nu_0 \frac{\partial^2 \overline{u}}{\partial \overline{y}^2} \tag{2.34}$$

$$\overline{u} \frac{\partial \vartheta}{\partial \overline{x}} + \overline{v} \frac{\partial \vartheta}{\partial \overline{y}} = \frac{\nu_0}{Pr} \frac{\partial^2 \vartheta}{\partial \overline{y}^2} \tag{2.35}$$

$$K = (1 - \vartheta) \tag{2.36}$$

with boundary conditions

$$\begin{aligned} \overline{u}(\overline{x}, \infty) = \overline{u}(\overline{x}, -\infty) = u_1(\overline{x}) \\ \vartheta(\overline{x}, \infty) = \vartheta(\overline{x}, -\infty) = 0 \\ \vartheta(\overline{x}, 0) = 1 \end{aligned} \tag{2.37}$$

and matching condition

$$\frac{\partial \vartheta}{\partial \overline{y}}(\overline{x}, 0^+) = -\varphi \frac{\partial \vartheta}{\partial \overline{y}}(\overline{x}, 0^-) \tag{2.38}$$

with

$$\left(\frac{T_f}{T_0} - 1\right) = \frac{\frac{q}{c_p T_0}\varphi}{1 + \varphi} \quad . \tag{2.39}$$

2.3 The Similarity Transformation

If the undisturbed gas velocity in the far field is

$$u_1(\overline{x}) = u_0 \left(\frac{\overline{x}}{\lambda}\right)^{\beta} \quad , \tag{2.40}$$

a similarity solution similar to the Falkner-Skan solution for boundary layers exists for the equations describing the flow field. In (2.40) λ is a suitable length scale and u_0 is a constant. The pressure gradient parameter β is positive for accelerating flows (favorable pressure gradient) and negative for decelerating flows (adverse pressure gradient). The solution of the equations is made possible by the introduction of the similarity variable

$$\eta = \frac{\overline{y}}{\sqrt{\nu_0 \overline{x}/u_1}} \tag{2.41}$$

and the stream function

$$\psi = \sqrt{\nu_0 u_1 \overline{x}}\, f(\eta) \tag{2.42}$$

where

$$\overline{u} = \frac{\partial \psi}{\partial \overline{y}} \qquad \text{and} \qquad \overline{v} = -\frac{\partial \psi}{\partial \overline{x}} \quad . \tag{2.43}$$

Expressed in terms of the similarity variables, the horizontal and vertical velocities are

$$\begin{aligned} \overline{u} &= u_1 f' \\ \overline{v} &= -\sqrt{\frac{\nu_0 u_1}{\overline{x}}}\left[\frac{\beta+1}{2} f + \frac{\beta-1}{2}\eta f'\right] \quad , \end{aligned} \tag{2.44}$$

and the governing equations are transformed to

$$\begin{aligned} f''' + \tfrac{1}{2}(\beta+1) f f'' + \beta\left[\left(\left(\frac{T_f}{T_0} - 1\right)\vartheta + 1\right) - (f')^2\right] &= 0 \\ \vartheta'' + \tfrac{1}{2}(\beta+1) Pr\, f\, \vartheta' &= 0 \\ K &= (1-\vartheta) \end{aligned} \tag{2.45}$$

with boundary and matching conditions

$$\begin{aligned} f'(\infty) = f'(-\infty) &= 1 \\ \vartheta(\infty) = \vartheta(-\infty) &= 0 \\ \vartheta(0) &= 1 \\ \vartheta'(0^+) &= -\varphi\, \vartheta'(0^-) \quad , \end{aligned} \tag{2.46}$$

with

$$\left(\frac{T_f}{T_0} - 1\right) = \frac{\dfrac{q}{c_p T_0}\varphi}{1 + \varphi} \quad . \tag{2.47}$$

Because the differential equations are highly nonlinear and a closed form solution is not known, a numerical scheme has to be employed for their solution.

2.4 The Numerical Method

Because the boundary conditions are specified at three different locations, $\eta = -\infty$, 0, and ∞, a shooting method is employed for the solution of the field equations. The method of solution follows the scheme described by Cebeci and Keller (1971).

For favorable pressure gradients ($\beta > 0$) the so called "simple shooting" method is used. For adverse pressure gradients ($\beta < 0$), two solution branches exist, which, for some values of β, necessitates the use of the "nonlinear eigenvalue" shooting method outlined by Cebeci and Keller.

The simple shooting method involves the following. $\eta = 0$ Is used as the starting point for the integration of the differential equations. Because only one boundary condition, $\vartheta(0) = 0$, is known at this point, estimates for the values of $f(0)$, $f'(0)$, $f''(0)$, and $\vartheta'(0)$ have to be made to start the integration procedure. The equations are integrated outwards in either direction to sufficiently large positive and negative values of η, $\eta = \eta_\infty$ and $\eta = \eta_{-\infty}$ respectively. The calculated values for f' and ϑ are compared with the boundary values for these variables at the respective limit points. New values for the initial estimates are calculated if the error is not within a specified tolerance. Newton's method, or any nonlinear algebraic equation solver can be used to calculate improved values for the initial estimates. This process is repeated until the solution converges. The differential equations were integrated using an Adams-Moulton predictor-corrector method with an initial Runge-Kutta step. A nonlinear algebraic equation solver was used to calculate new iterates for the initial conditions.

For the "nonlinear eigenvalue" problem $\vartheta'(0)$ is fixed and β, together with $f(0)$, $f'(0)$, and $f''(0)$ are taken as parameters which are varied until the far field boundary conditions are satisfied. New iterates for the variable parameters are calculated by the same method that was used for the simple shooting procedure.

Chapter 3

The Structure of a Diffusion Flame in a Favorable Pressure Gradient

The transformed field equations (2.45) were solved for $\frac{T_f}{T_0} = 7$ and $Pr = 0.72$. Two stoichiometric fuel–air ratios were considered, $\varphi = 1$ which yields a symmetric flow field about the flame, and $\varphi = 0.058$ which corresponds to the combustion of methane in air. The latter yields an asymmetric flow field which is characteristic of the combustion of hydrocarbons in air. The pressure gradient parameter β was varied from zero to four for each of the two stoichiometric fuel–air ratios.

Figs(3.1)–(3.5) ($\varphi = 1$) and (3.6)–(3.10) ($\varphi = 0.058$) show all the significant flow field properties ; the distribution of fuel and oxidizer mass fractions, K_1 and K_2 ,normalized temperature ϑ, streamwise velocity ratio $f' = \frac{\overline{u}}{u_1}$, cross stream velocity $\overline{v}$ and the similarity streamfunction f plotted against the similarity variable η. From these figures it can be seen that the hot, low density fluid produced by the combustion process responds more readily to the imposed pressure gradient, resulting in higher streamwise fluid velocities in the vicinity of the flame. For the symmetric flame $\eta = 0$ is the center of the high temperature, low density region so the highest streamwise velocities are encountered here. For the case $\varphi = 0.058$ the flame moves into the oxidizer, steepening the oxidizer concentration gradient $\frac{\partial K_2}{\partial \eta}$ and decreasing the fuel concentration gradient $\frac{\partial K_1}{\partial \eta}$ in such a way that the reactants diffuse to the flame in the correct stoichiometric fuel–air ratio. Because we have chosen a coordinate system in which the flame is fixed along the horizontal axis, this phenomenon manifests itself as a cross stream velocity through the flame. Combustion products are thus transported from the flame into the fuel stream in the upper half plane, in effect diluting the fuel and hence decreasing its concentration gradient. In the oxidizer the opposite is true. Fresh oxidizer from the far field is transported toward the flame by the cross stream velocity, increasing $\frac{\partial K_2}{\partial \eta}$. The decreased fuel and enhanced oxidizer gradients cause diffusion of the reactants towards

the flame in the correct ratio.

As the pressure gradient parameter β is increased, the maximum value of f' (the ratio of streamwise velocity to the free stream streamwise velocity) increases, at first rapidly between $\beta = 0$ and 0.5, and then at a slower rate between $\beta = 0.5$ and 4 (fig(3.21)). One expects the maximum horizontal velocity to increase as the pressure gradient is increased, but applying the pressure gradient on the flow field has other effects which account for the observed behavior of the maximum horizontal velocity. Increasing the value of β has the effect of increasing the entrainment velocities of both the fuel and oxidizer towards the flame. This effect can be seen clearly for $\varphi = 1$, $\beta = 0 \rightarrow 4$ (figs(3.1)–(3.5)). This has the effect of narrowing the diffusion zones of both fuel and oxidizer and thus creating steeper concentration gradients. This has two opposing effects on the maximum streamwise velocity. Narrowing the width of the thermal layer has the effect of decreasing the maximum streamwise velocity for a fixed pressure gradient (it will be seen that adverse pressure gradients widen the thermal layer with the result that small pressure gradients have a large effect on the streamwise velocity). However, the increased heat release caused by the enhanced fuel mass consumption has the effect of increasing the streamwise velocity. Close to $\beta = 0$ the thermal layer is relatively wide, so increasing the value of β has a significant effect on the streamwise velocity. However, between $\beta = 0$ and $\beta = 0.5$ the width of the thermal layer decreases rapidly, with the result that, for values of β larger than 0.5, an increase in the pressure gradient does not cause the equivalent expected rise in the maximum horizontal velocity. For values of β larger than 0.5 the width of the layer decreases slowly, but this is more than compensated for by the increasing pressure gradient and the enhanced heat release at the flame. The effect of the applied pressure gradient on the entrainment of fuel and oxidizer towards the flame is depicted more clearly in the figures showing the streamlines of the flowfields (figs(3.11)–(3.20)). The dark lines are the streamlines, the lighter lines

are constant values of the similarity variable η in increments of 1.0; $\eta = 0$ corresponds to the horizontal axis where the flame is located, positive values of η are in the upper half plane and negative values in the lower half plane. Since the flow is steady, the streamlines correspond to particle paths in the flow field. In the absence of a pressure gradient ($\beta = 0$, fig(3.11)), the reactants in the far field move parallel to the flame. When the pressure gradient is applied, however, fluid particles that are far from the flame for small values of $\frac{\overline{x}}{\lambda}$ are entrained towards the flame as they are convected downstream (figs(3.11)–(3.15)).

The fuel mass consumption rate per unit area at a location x along the horizontal axis is

$$\dot{m}_f = \rho D \frac{\partial K_1}{\partial y}(x, 0^+) \tag{3.1}$$

or, in terms of the similarity variable

$$\dot{m}_f = \rho_0 D_0 \left(\frac{u_1(x)}{\nu_0\, x}\right)^{\frac{1}{2}} \frac{\partial K_1}{\partial \eta}(0^+) \tag{3.2}$$

The normalized mass consumption rate

$$\frac{\dot{m}_f}{\rho_0 D_0 \left(\frac{u_1(x)}{\nu_0\, x}\right)^{\frac{1}{2}}}$$

is plotted against β for $\varphi = 1$ and $\varphi = 0.058$ in figs(3.22) and (3.23) respectively.

In order to acquire a better understanding of the mass consumption augmentation for increasing β, it is useful to compare the problem under consideration to the time dependent, strained diffusion flame which has been the subject of intensive study and is therefore well understood. Because the streamwise velocity at the flame

$$u_f = f'(0)\, u_0 \left(\frac{x}{\lambda}\right)^{\beta} \tag{3.3}$$

is an increasing function of $\frac{x}{\lambda}$ for positive β, a flame element moving along the horizontal axis encounters a strain field

$$\varepsilon(x) = \frac{du_f}{dx} = \frac{\beta\, f'(0)\, u_0}{\lambda} \left(\frac{x}{\lambda}\right)^{\beta-1} \tag{3.4}$$

A diffusion flame undergoing a steady strain rate ε_0 attains a steady mass consumption rate

$$\dot{m}_{\varepsilon_0} = \rho_0 D_0 \left(\frac{2D_0\varepsilon_0}{\pi}\right)^{\frac{1}{2}} \left(\frac{1+\varphi}{2}\right) e^{-\eta_f{}^2} \quad . \tag{3.5}$$

where

$$\operatorname{erf}\eta_f = -\left(\frac{1-\varphi}{1+\varphi}\right) \tag{3.6}$$

(See Carrier, Fendell and Marble (1975) or Karagozian (1982)). Utilizing (3.4) and (3.5) one obtains, in terms of the flow field variables:

$$\dot{m}_{\varepsilon_0} = \rho_0 D_0 \left(\frac{u_1(x)}{\nu_0\, x}\right)^{\frac{1}{2}} \left(\frac{2\,\beta\, f'(0)\, Sc}{\pi}\right)^{\frac{1}{2}} \left(\frac{1+\varphi}{2}\right) e^{-\eta_f{}^2} \tag{3.7}$$

which has the same functional form as (3.2). The mass consumption rates for the above approximate calculation are compared to the actual mass consumption rates for $\varphi = 1$ and $\varphi = 0.058$ in tables (3.1) and (3.2) respectively. Agreement between the two is not good, except for the case $\beta = 1$ which corresponds to a constant strain rate. This suggests that non–steady effects are probably important (ie. that the mass consumption probably does not reach the steady value corresponding to the applied strain rate).

By integrating (3.3), the position of a flame element x_e can be found:

$$\left(\frac{x_e}{\lambda}\right) = \left(\left(\frac{x_0}{\lambda}\right)^{1-\beta} - \frac{(\beta-1)f'(0)u_0 t}{\lambda}\right)^{\frac{1}{1-\beta}} \qquad \beta \neq 1 \tag{3.8}$$

where x_0 is the initial position of the flame element. Now since both the position as a function of time of the flame element and the strain as a function of position are known, the strain rate of the flame element as a function of time can be obtained:

$$\varepsilon(t) = \frac{1}{\dfrac{\lambda}{\beta\, f'(0)\, u_0}\left(\dfrac{x_0}{\lambda}\right)^{1-\beta} - \dfrac{\beta-1}{\beta}\, t} \quad . \tag{3.9}$$

The mass consumption rate as a function of time for a diffusion flame undergoing this strain rate is obtained in Appendix A. After converting back to the spatial coordinate,

the mass consumption rate is given by the expression

$$\dot{m}_{str}(x) = \rho_0 D_0 \left(\frac{u_1}{\nu_0\, x}\right)^{\frac{1}{2}} \left(\frac{(1+\beta)\, f'(0)\, Sc}{\pi}\right)^{\frac{1}{2}} \left(\frac{1+\varphi}{2}\right) e^{-\eta_f{}^2} \quad . \tag{3.10}$$

Case 1: $\varphi = 1$

The mass consumption rates for the strained flame approximations are compared to the actual mass consumption rates for $\varphi = 1$ in table (3.1). Agreement is good, the actual value being consistently between 93% and 96% of the approximate value. The approximate calculation is expected to yield higher mass consumption rates since the strain field is assumed to be independent of y and equal to $\frac{\beta f'(0) u_1}{x}$. In the actual flow field the strain field has a maximum of $\frac{\beta f'(0) u_1}{x}$ at the flame and it drops off to $\frac{1}{f'(0)}$ of this value in the far field. The approximate calculation therefore generates higher entrainment velocities than are present in the actual flow field. The diffusion zones are therefore thinner and the mass consumption rates consequently higher. This effect can clearly be seen in table (3.1). As β increases, so does the value of $f'(0)$. The value of $f'(0)$ is a measure of the ratio of the strain rate at the flame to that in the far field. For $\beta = 0.1$, the value of $f'(0)$ is 1.481 and the mass consumption is 96% of the approximate value. As β is increased to 4 from 0.1, the value of $f'(0)$ increases to 2.177 and the value of the mass consumption rate falls from 96% to 93% of the approximate value. If an appropriately averaged value for the the strain rate is used in the approximate calculation, better results would be obtained.

Case 2: $\varphi = 0.058$

Table (3.2) shows the comparison of the strained flame approximation to the actual mass consumption for $\varphi = 0.058$. Here the actual value of the fuel mass consumption rate is between 87% and 89% of the approximate value. The difference can again be ascribed to the assumption of a strain field independent of y in the approximate calculation.

Because the results for the diffusion flame in a pressure gradient compare favorably

with those for the strained diffusion flame for infinite reaction rates, we can expect the two cases to exhibit a similar behavior for finite reaction rates. The strained flame with finite reaction rates has been widely studied. Carrier, Fendell and Marble (1976) studied the structure of the reaction zone for diffusion flames subject to both steady and unsteady strain rates. Liñán (1974) studied the structure and stability (with an emphasis on ignition and extinction phenomena) of diffusion flames subject to constant strain rates.

The Damköhler number for the flow field (the ratio of characteristic flow time to chemical reaction time which $\sim \frac{1}{\varepsilon}$ for the strained diffusion flame) is an important parameter determining the structure of the reaction zone. With infinite reaction rates the fuel mass consumption rate is enhanced by an increase in the strain rate because of the increased entrainment of reactants towards the flame zone. With finite reaction rates, however, the rapid inflow of cool reactants towards the flame might quench the flame and cause extinction at a certain, critical Damköhler number (corresponding to a critical strain rate).

Consider now the expression for the strain rate of a flame element travelling along the diffusion flame in a pressure gradient

$$\varepsilon(t) = \frac{1}{\frac{\lambda}{\beta\, f'(0)\, u_0}\left(\frac{x_0}{\lambda}\right)^{1-\beta} - \frac{\beta-1}{\beta}\, t} \quad . \tag{3.9}$$

For $\beta < 1$ the strain rate decreases for increasing time and $\varepsilon \to 0$ as $t \to \infty$. This implies that, if a flame exists at some position $\frac{x_0}{\lambda}$, a flame element moving in the direction of increasing $\frac{x}{\lambda}$ will not show a tendency towards extinction. For $\beta > 1$, however, the strain rate increases for increasing time and becomes unbounded after a certain critical time (corresponding to the flame element moving to infinite values of $\frac{x}{\lambda}$). A flame element starting off at position $\frac{x_0}{\lambda}$ therefore experiences an increasing strain rate as it moves downstream. As it approaches the point corresponding to the limiting Damköhler num-

ber (and hence limiting strain rate) at which extinction occurs, finite reaction rate effects become important and extinction eventually occurs. The similarity solution therefore becomes invalid. However, since the boundary layer equations are parabolic in nature (and it is assumed that the thin combustion boundary layer has little effect on the outer flow which is described by elliptic equations), it is expected that the similarity solution would hold up to the point where finite reaction rates become important, since information about the flow field downstream of this point cannot be propagated upstream.

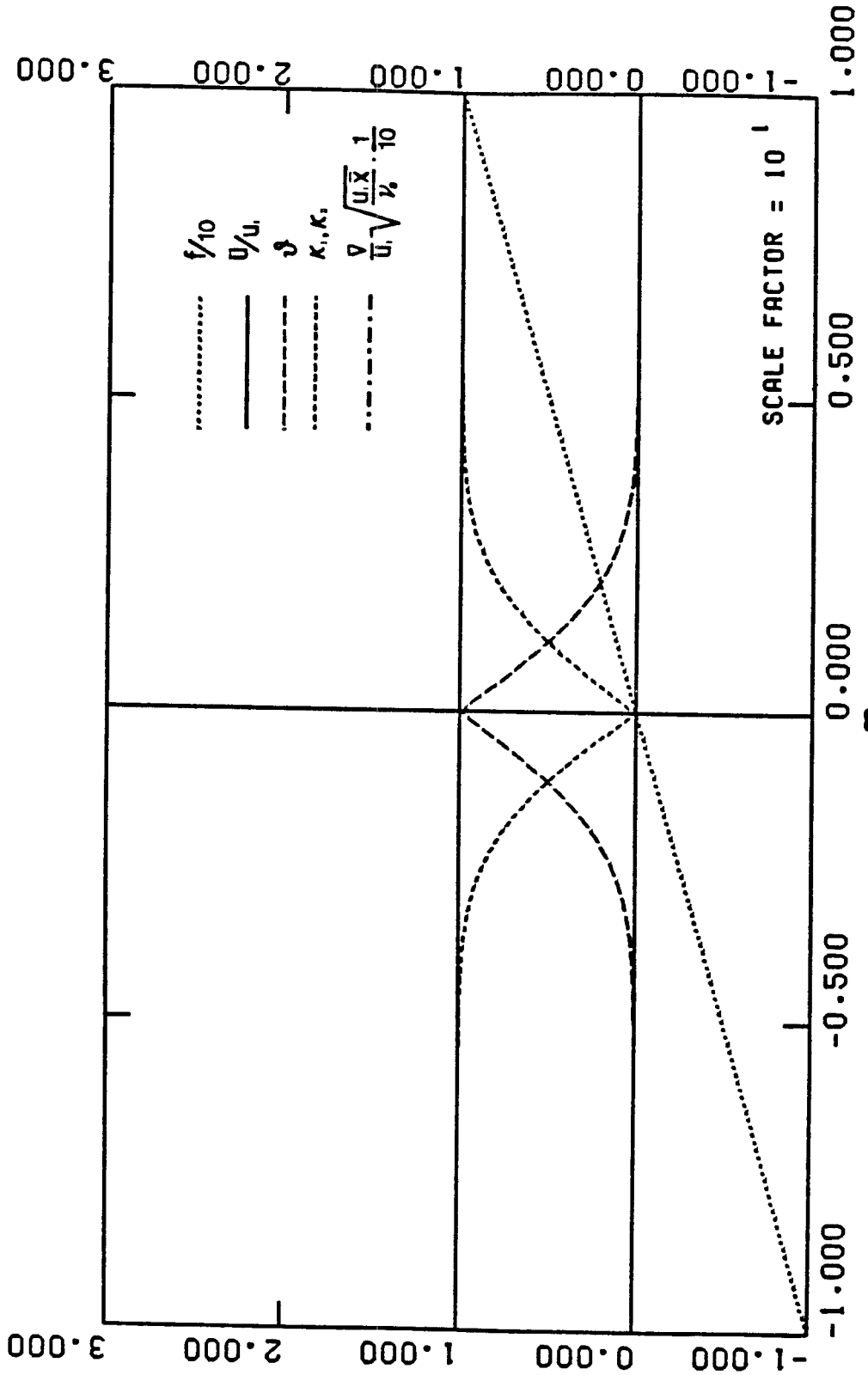

Figure (3.1) Distribution of Properties for a Diffusion Flame with $\varphi = 1.0$, $\beta = 0.0$ $(K'(0^+) = 0.478)$.

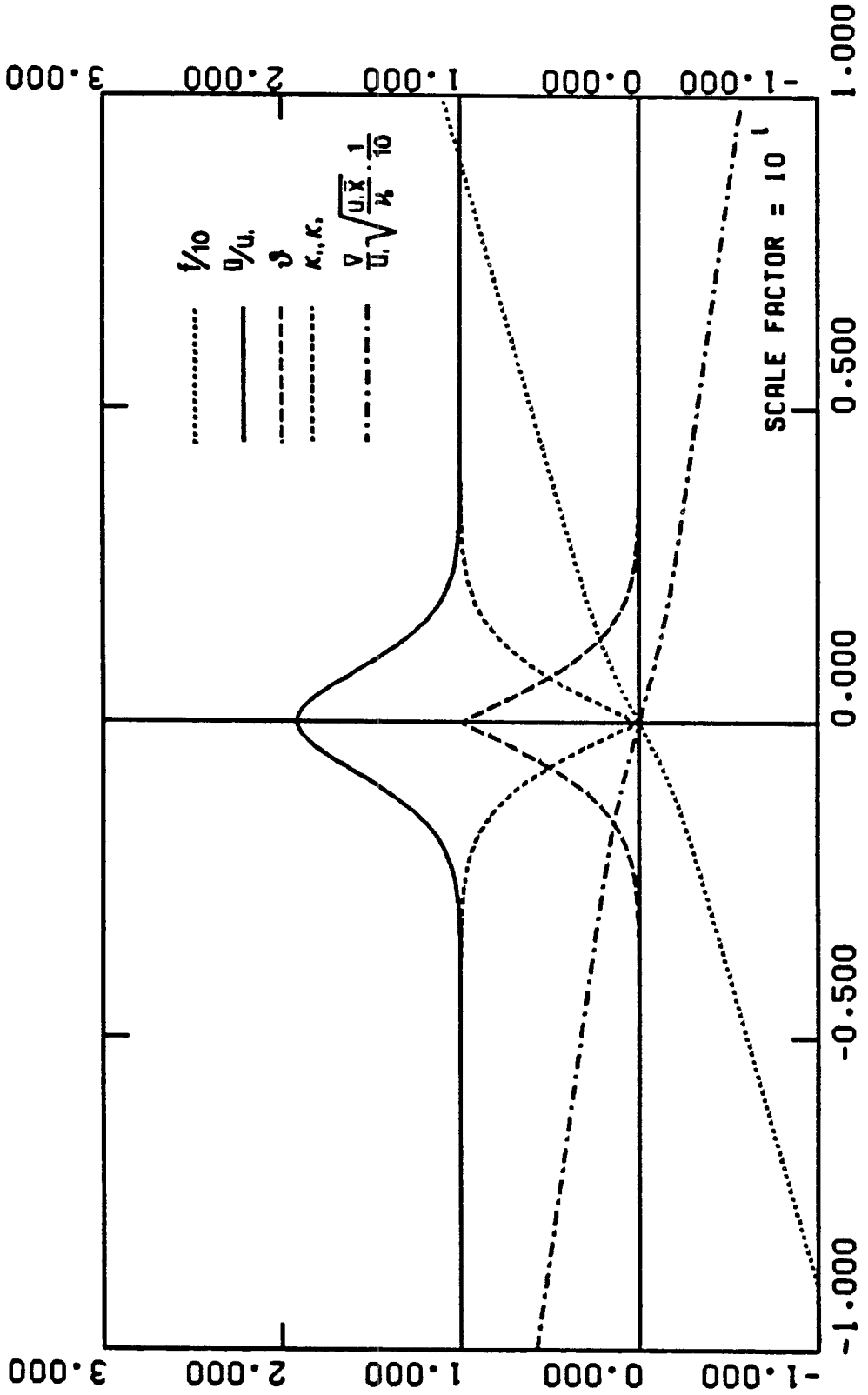

Figure (3.2) Distribution of Properties for a Diffusion Flame with $\varphi = 1.0$, $\beta = 0.5$ $(K'(0^+) = 0.764)$.

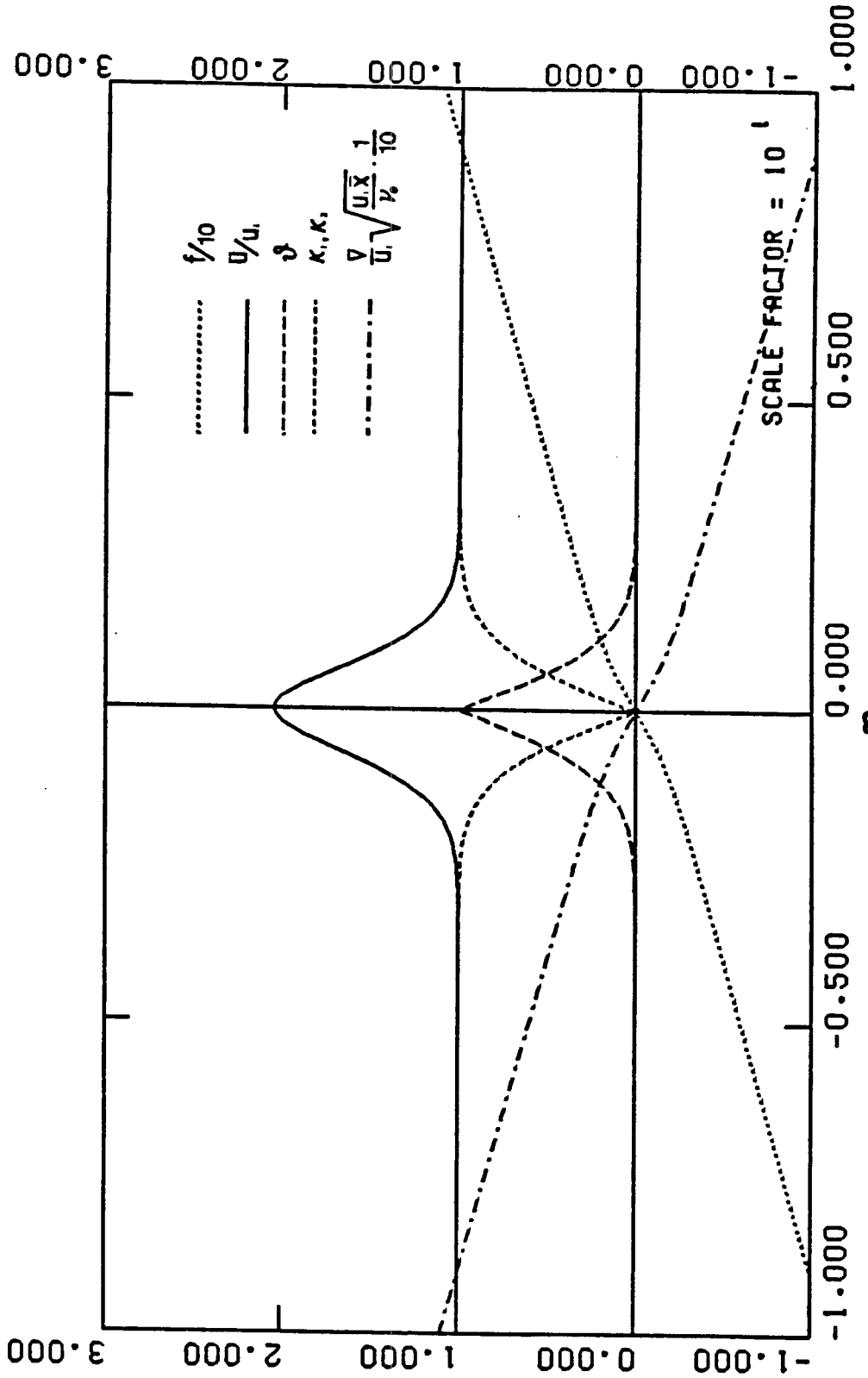

Figure (3.3) Distribution of Properties for a Diffusion Flame with $\varphi = 1.0$, $\beta = 1.0$ $(K'(0^+) = 0.907)$.

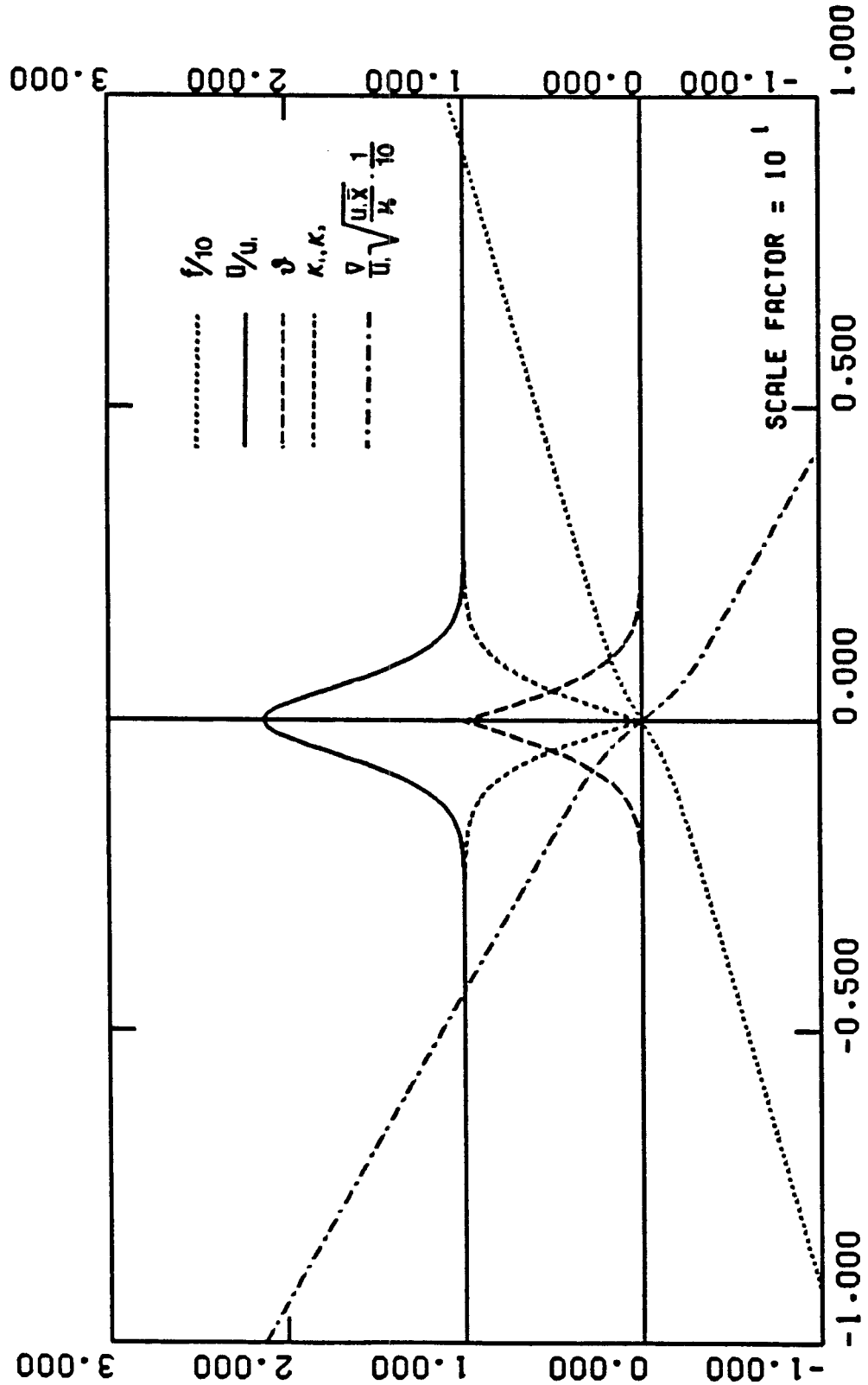

Figure (3.4) Distribution of Properties for a Diffusion Flame with $\varphi = 1.0$, $\beta = 2.0$ $(K'(0^+) = 1.130)$.

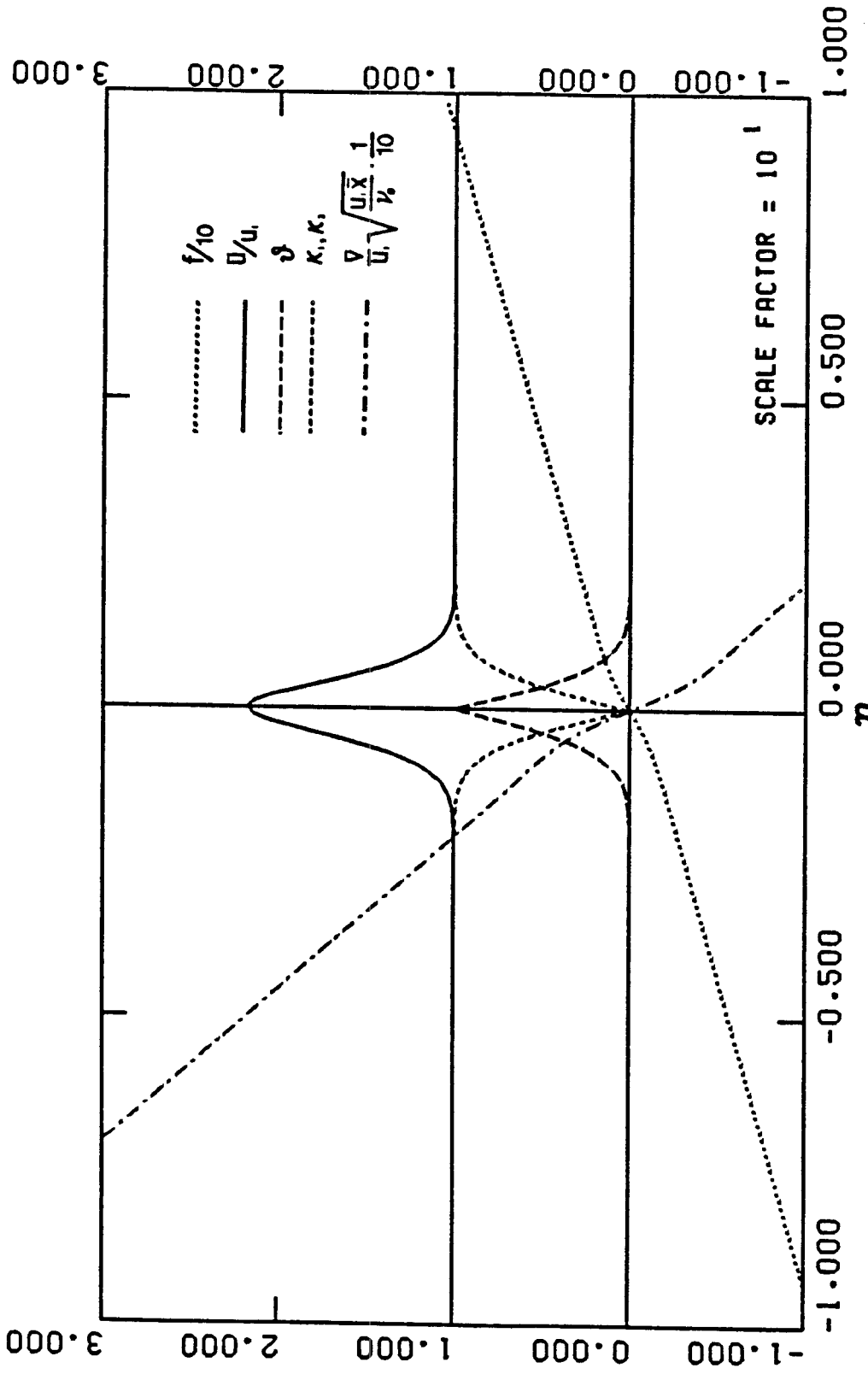

Figure (3.5) Distribution of Properties for a Diffusion Flame with $\varphi = 1.0$, $\beta = 4.0$ $(K'(0^+) = 1.473)$.

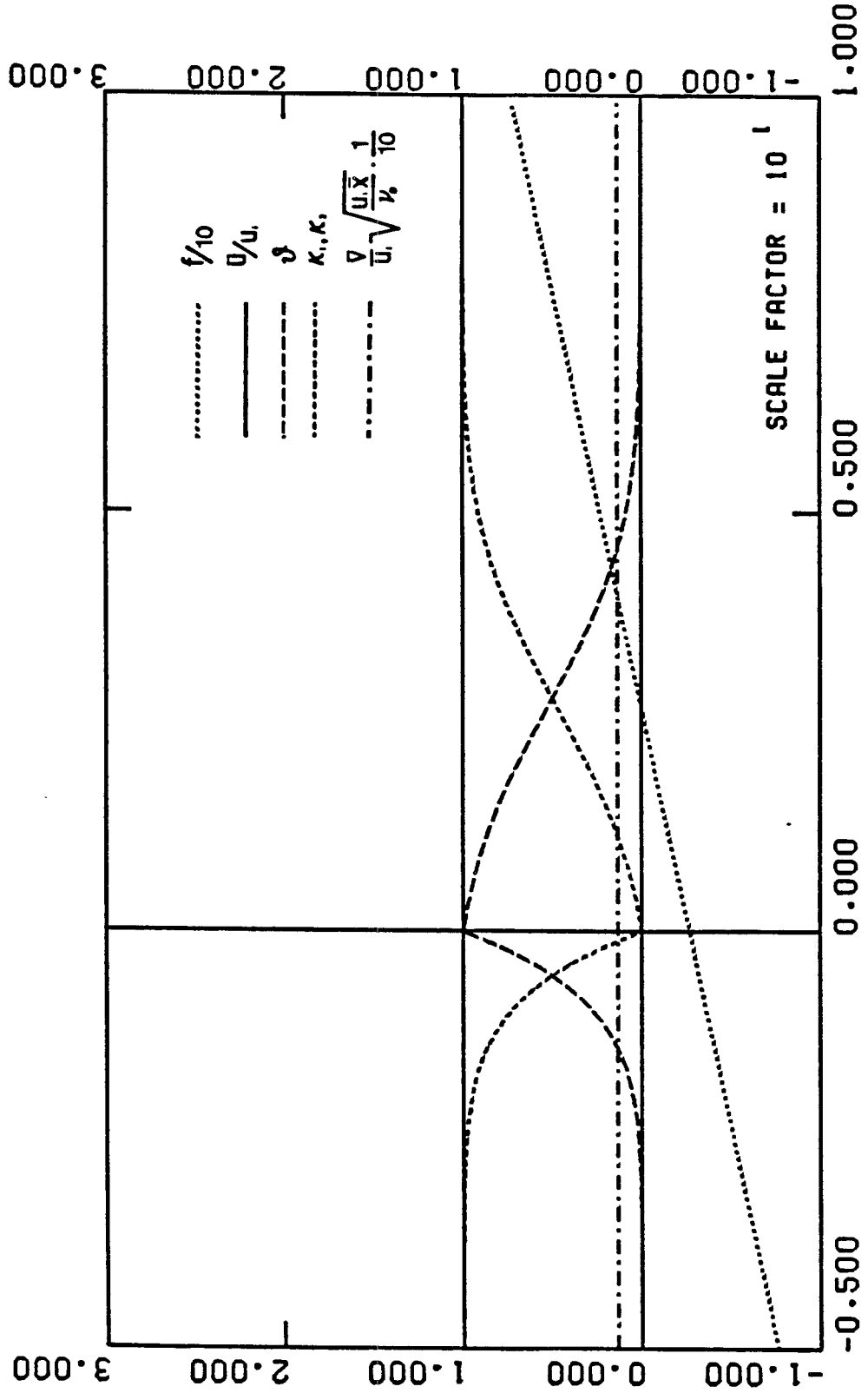

Figure (3.6) Distribution of Properties for a Diffusion Flame with $\varphi = 0.058$, $\beta = 0.0$ $(K'(0^+) = 0.071)$.

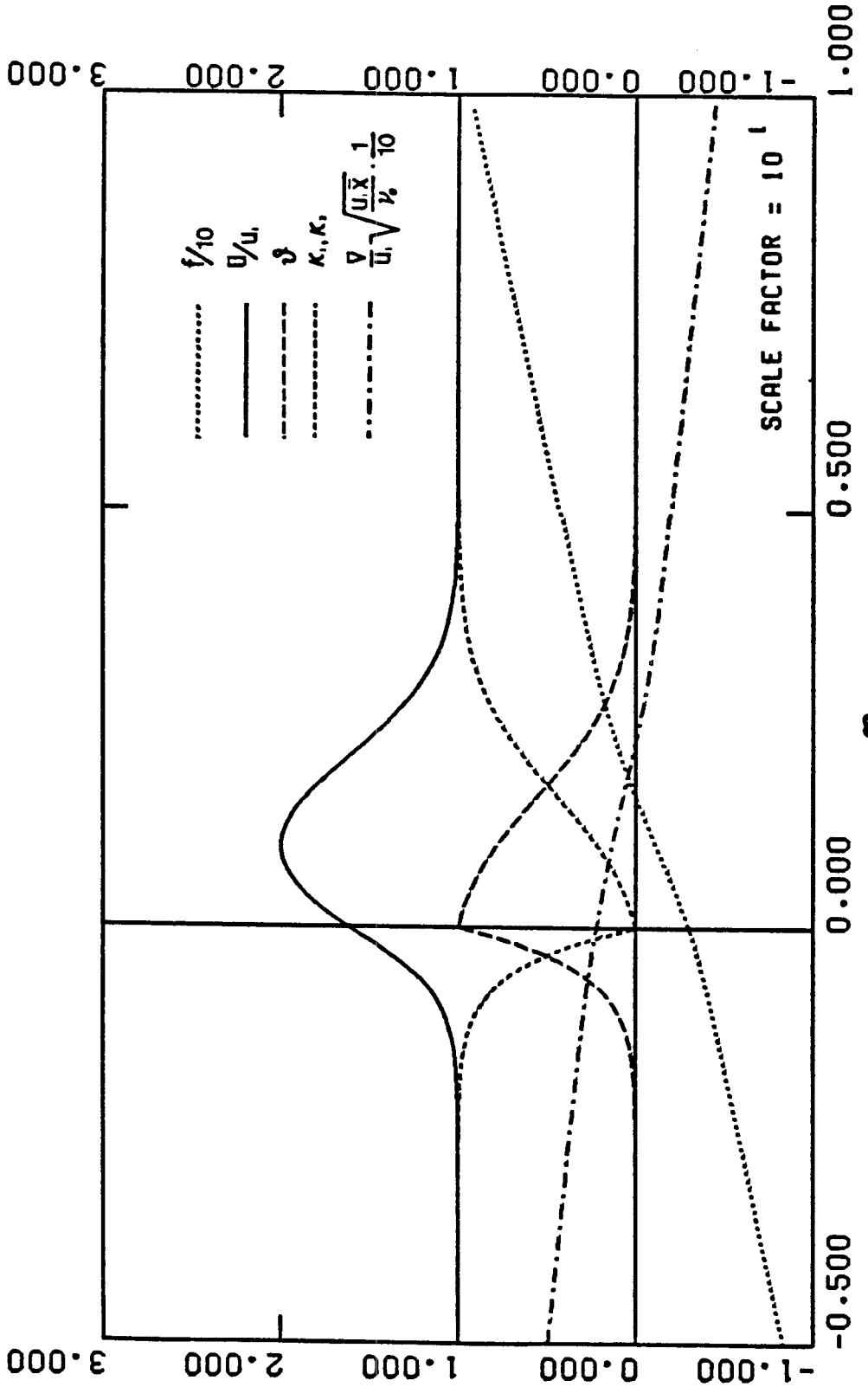

Figure (3.7) Distribution of Properties for a Diffusion Flame with $\varphi = 0.058$, $\beta = 0.5$ $(K'(0^+) = 0.113)$.

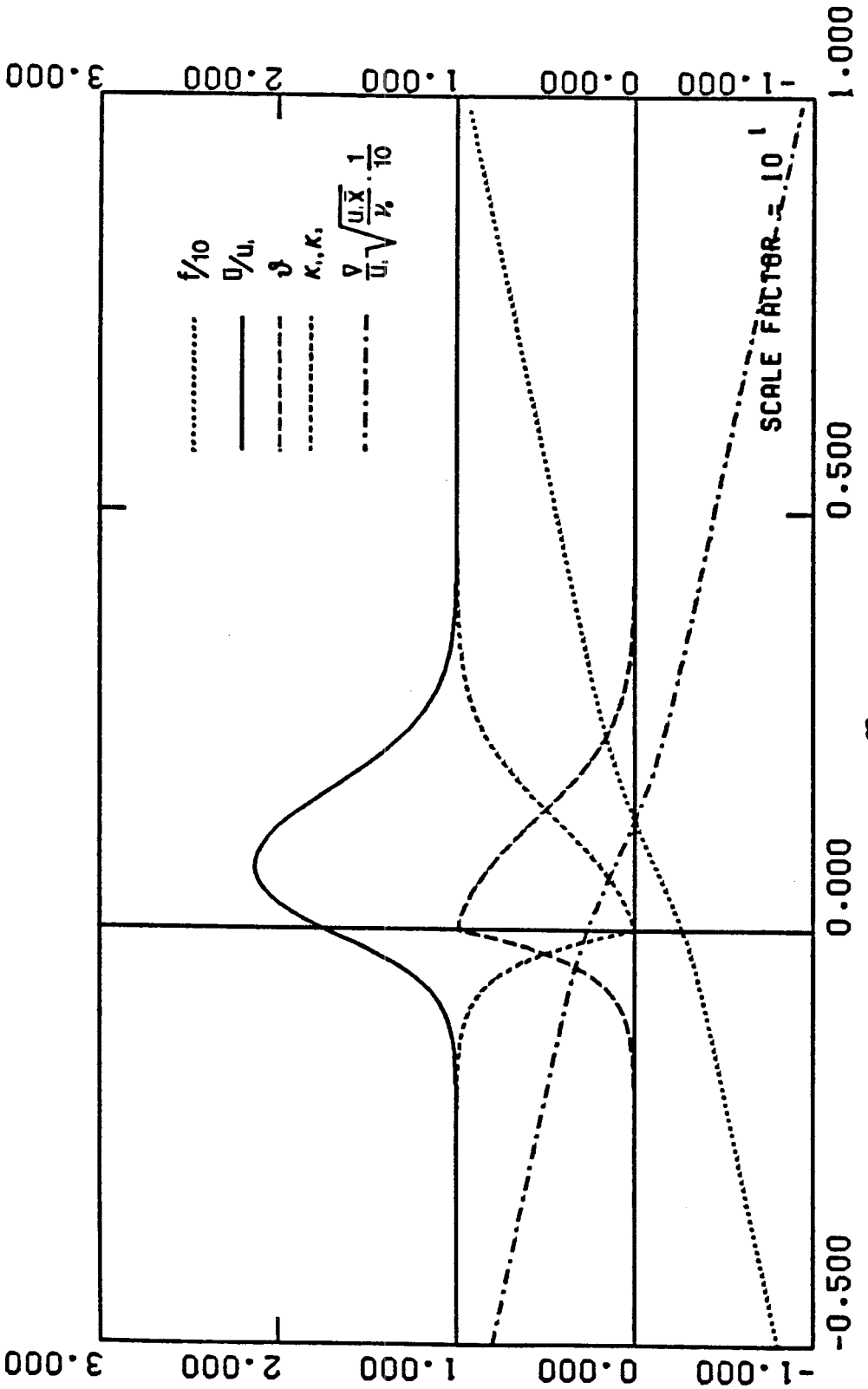

Figure (3.8) Distribution of Properties for a Diffusion Flame with $\varphi = 0.058$, $\beta = 1.0$ $(K'(0^+) = 0.134)$.

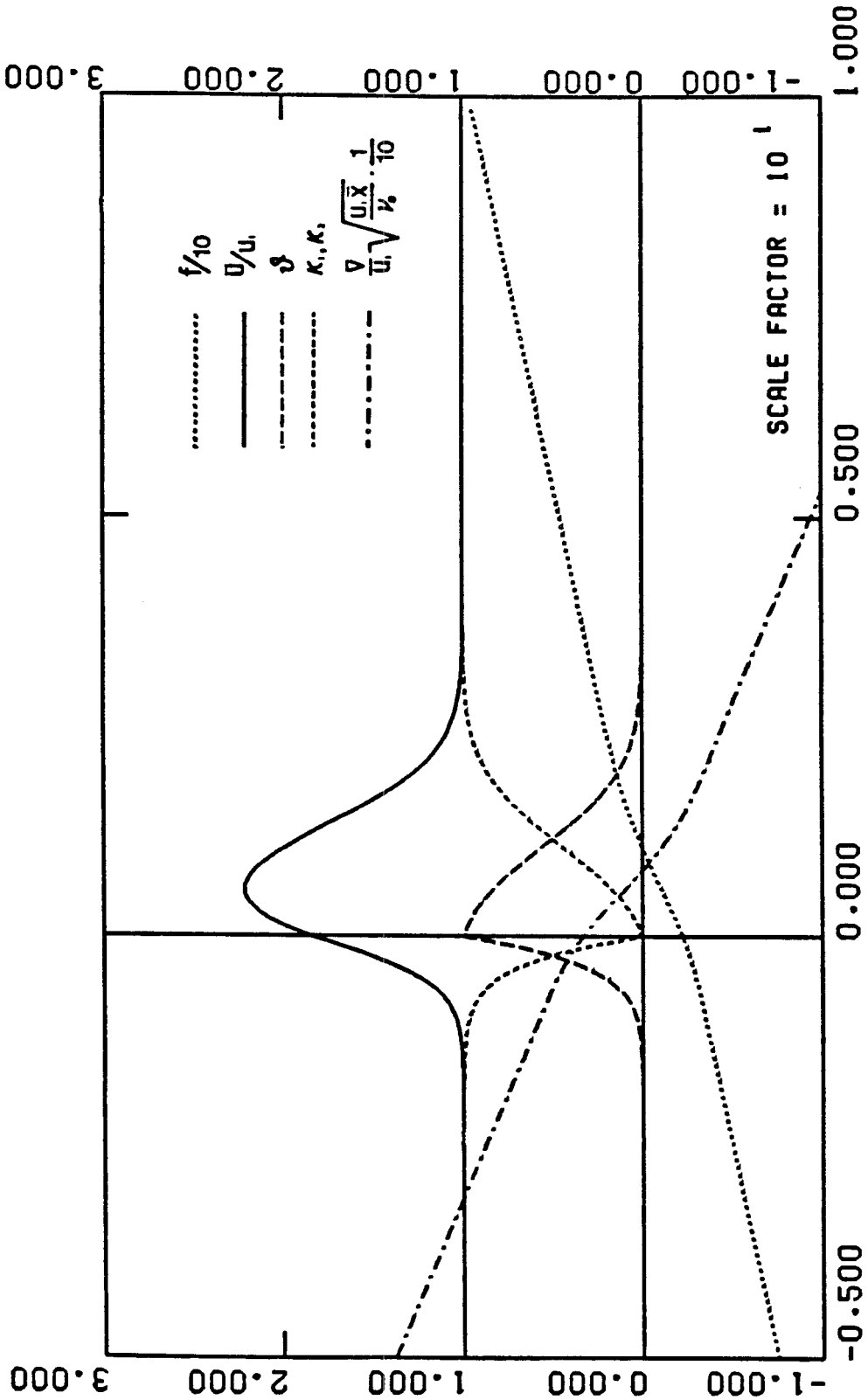

Figure (3.9) Distribution of Properties for a Diffusion Flame with $\varphi = 0.058$, $\beta = 2.0$ $(K'(0^+) = 0.168)$.

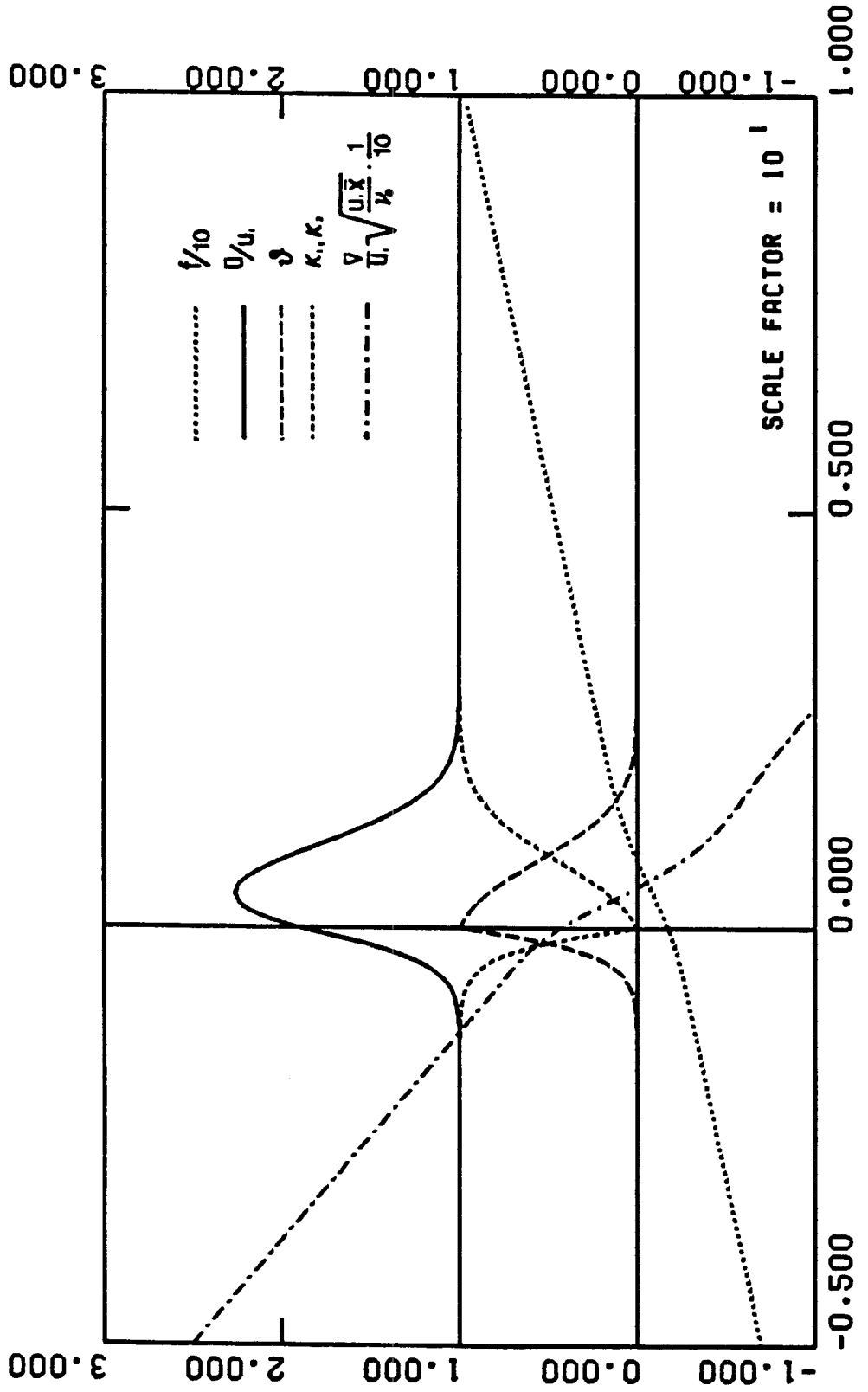

Figure (3.10) Distribution of Properties for a Diffusion Flame with $\varphi = 0.058$, $\beta = 4.0$ $(K'(0^+) = 0.219)$.

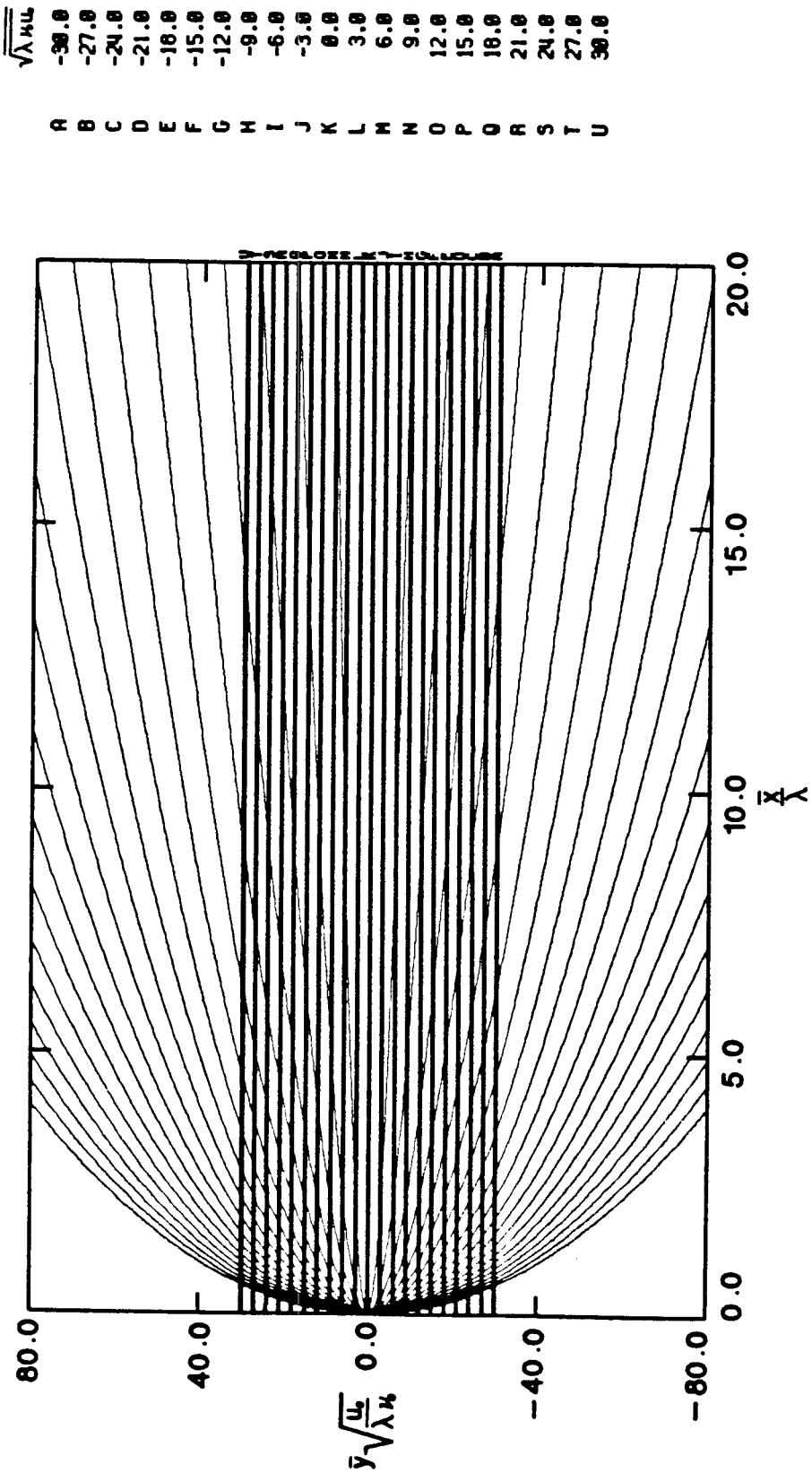

Figure (3.11) Streamline Patterns for a Diffusion Flame with $\varphi = 1.0$, $\beta = 0.0$ $(K'(0^+) = 0.478)$.

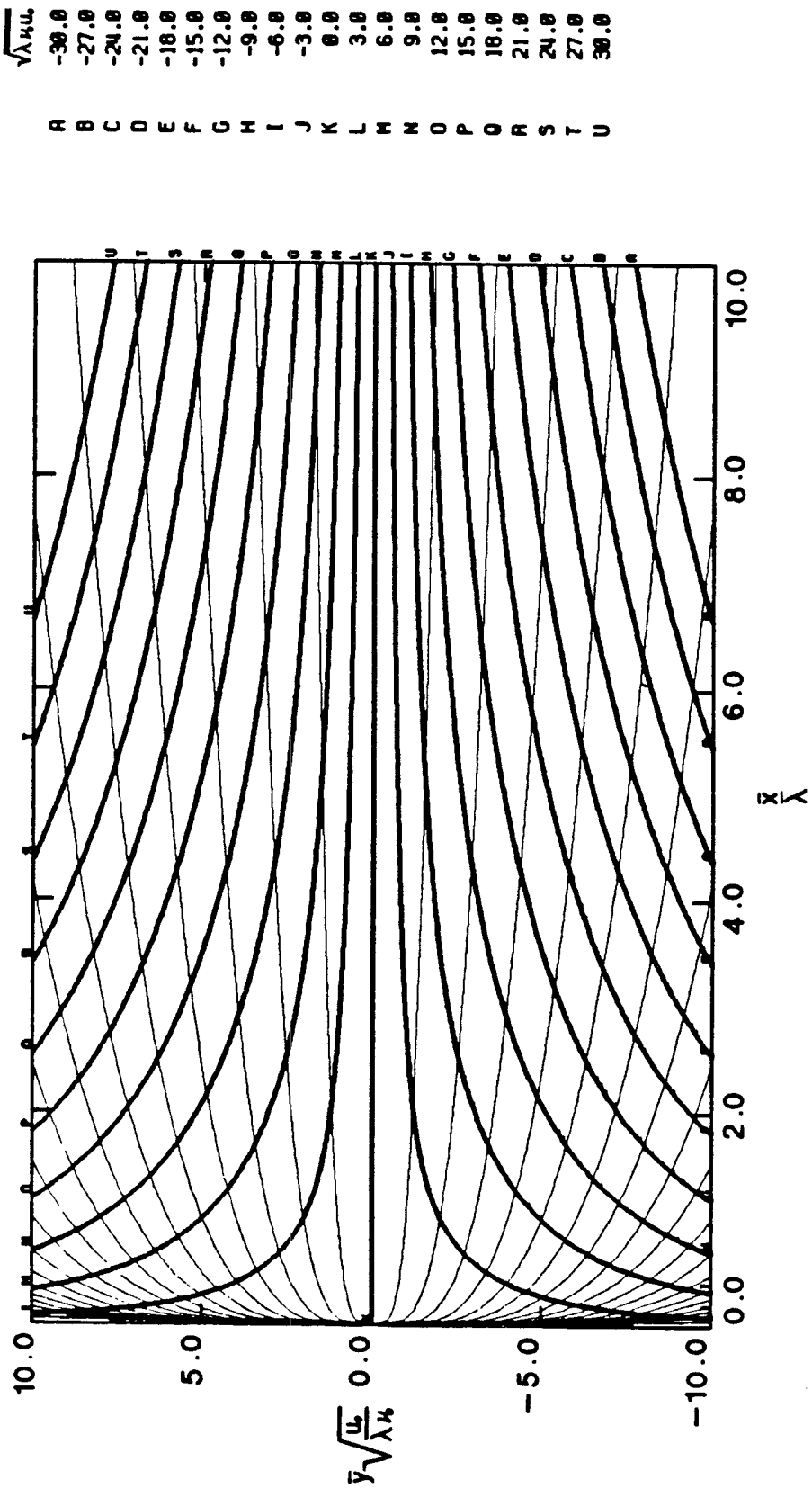

Figure (3.12) Streamline Patterns for a Diffusion Flame with $\varphi = 1.0$, $\beta = 0.5$ $(K'(0^+) = 0.764)$.

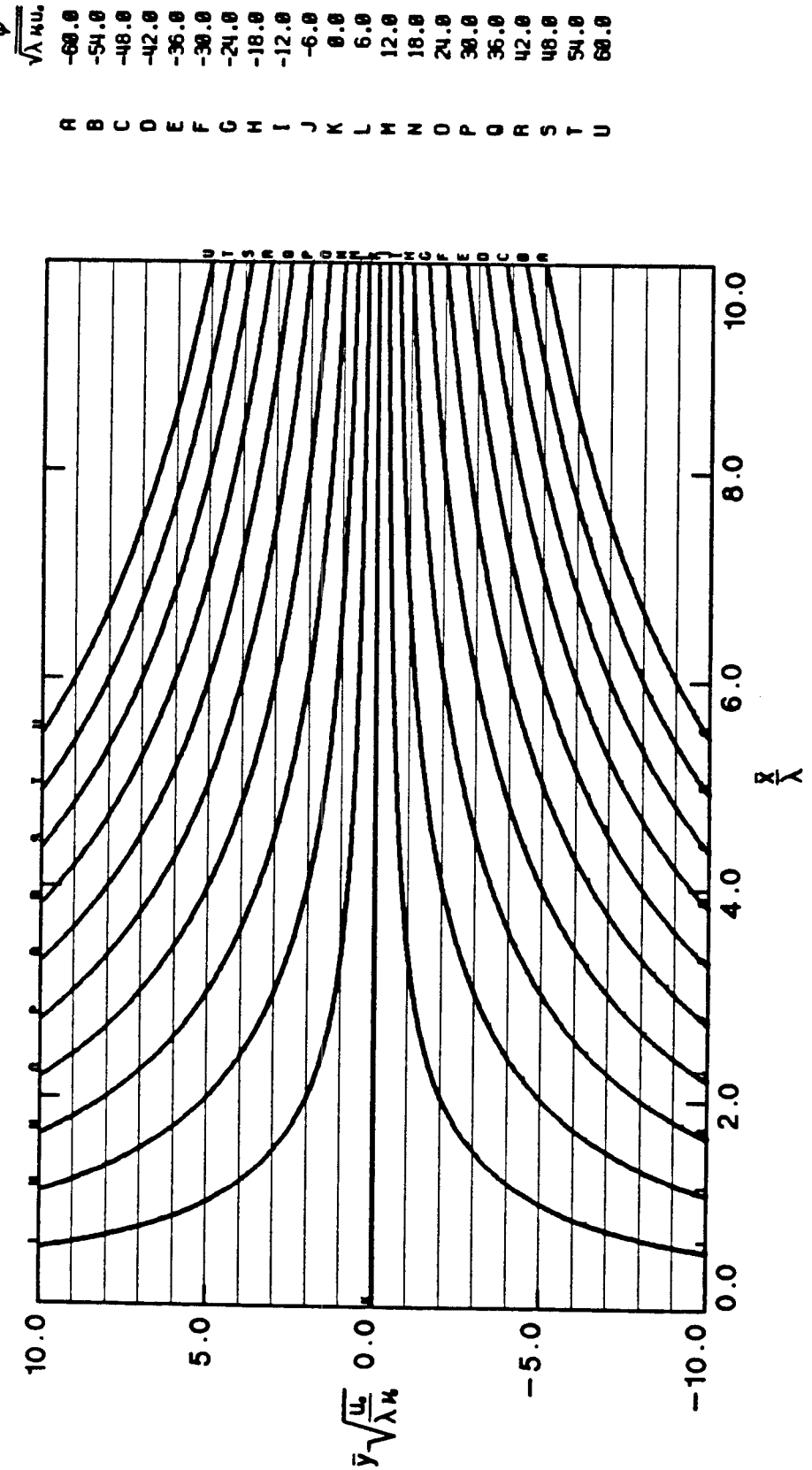

Figure (3.13) Streamline Patterns for a Diffusion Flame with $\varphi = 1.0$, $\beta = 1.0$ $(K'(0^+) = 0.907)$.

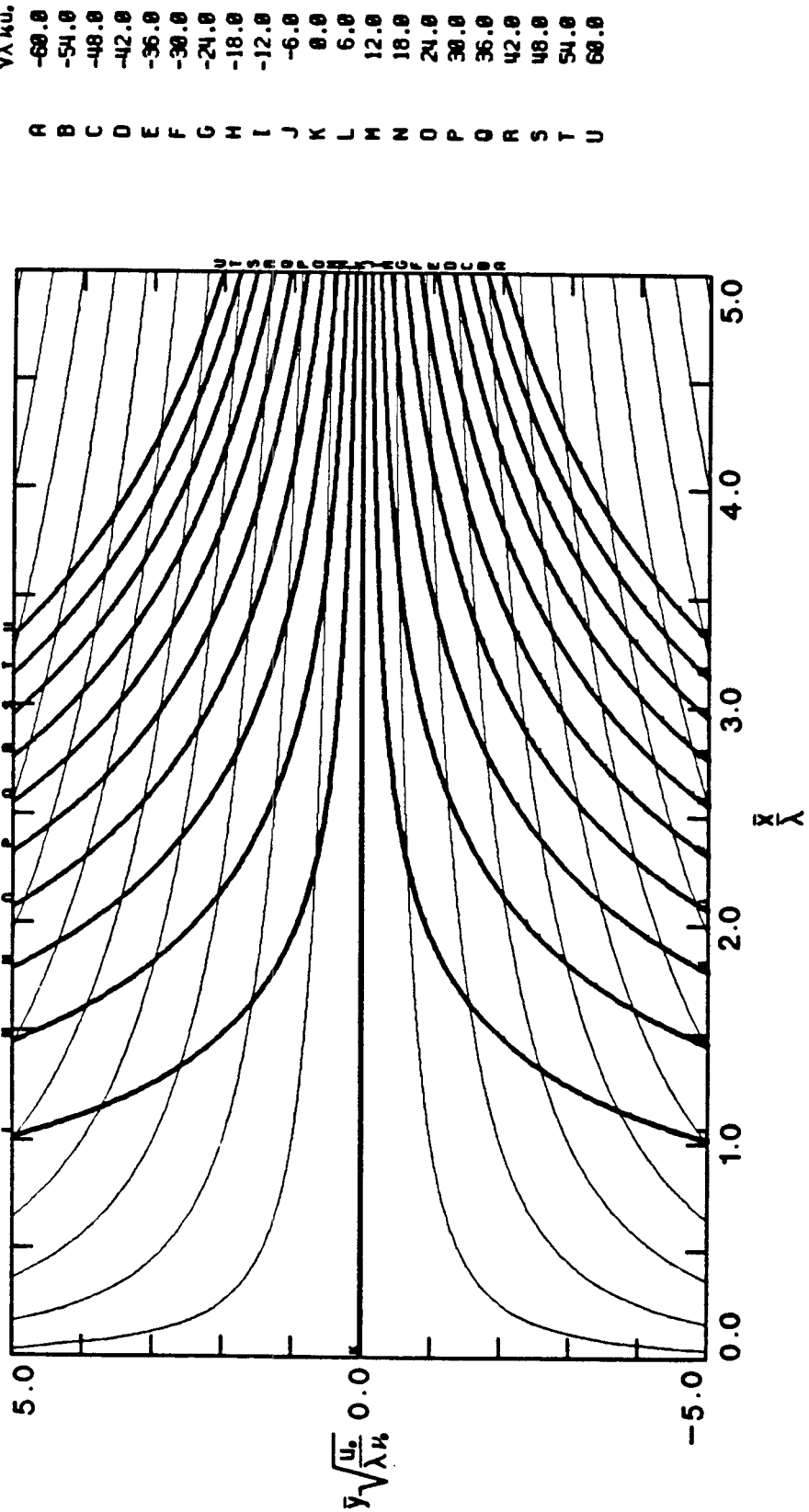

Figure (3.14) Streamline Patterns for a Diffusion Flame with $\varphi = 1.0$, $\beta = 2.0$ $(K'(0^+) = 1.130)$.

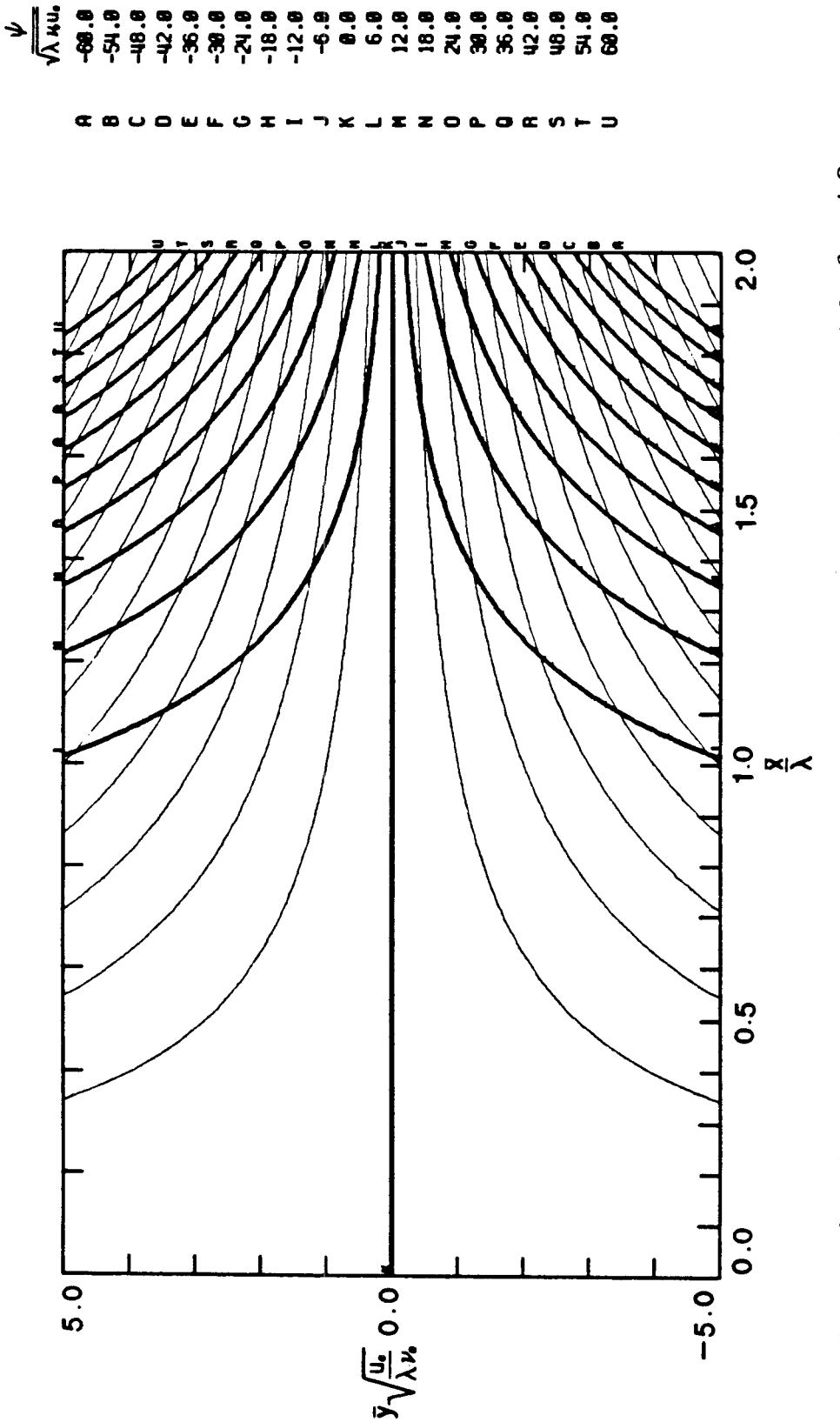

Figure (3.15) Streamline Patterns for a Diffusion Flame with $\varphi = 1.0$, $\beta = 4.0$ ($K'(0^+) = 1.473$).

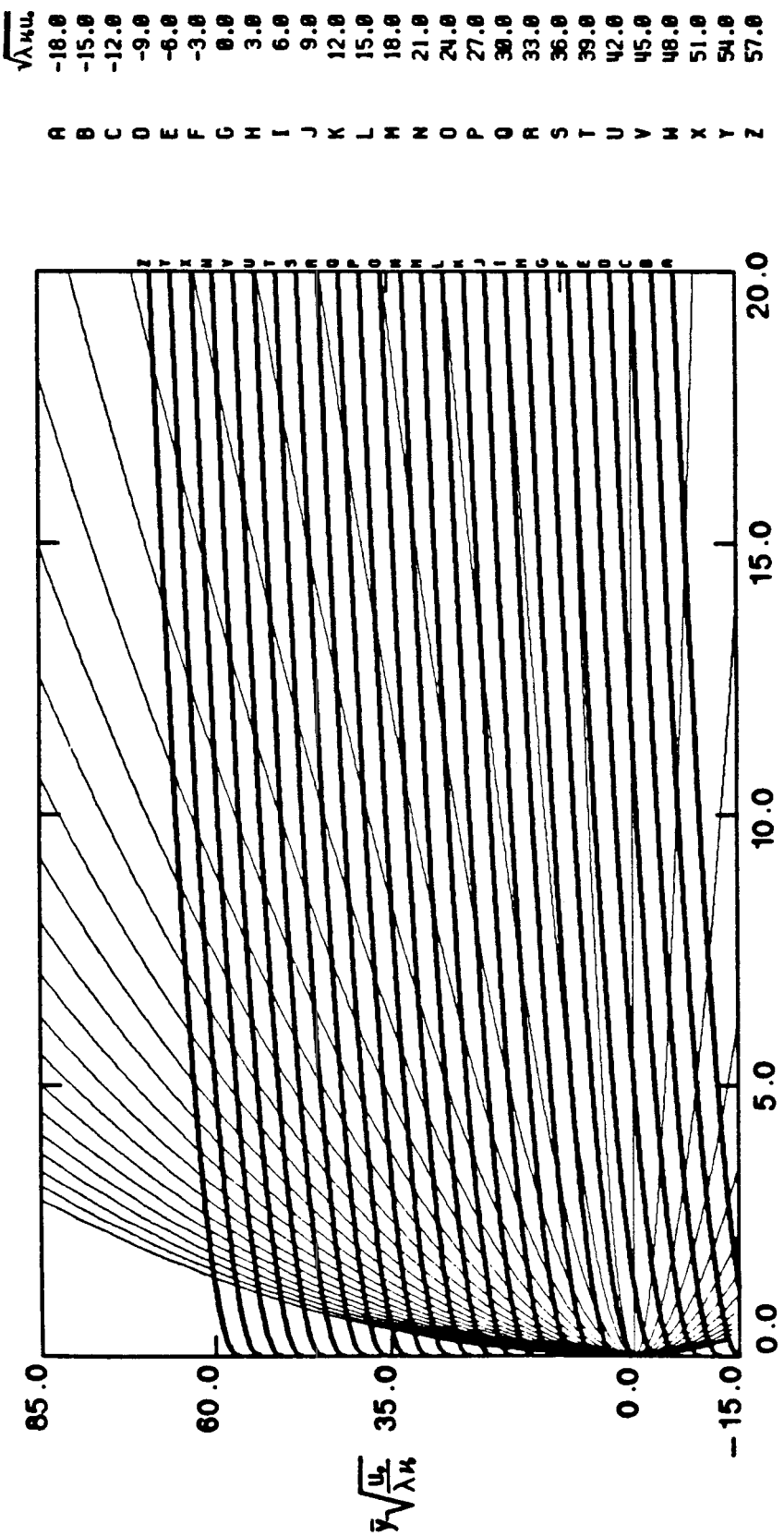

Figure (3.16) Streamline Patterns for a Diffusion Flame with $\varphi = 0.058$, $\beta = 0.0$ $(K'(0^+) = 0.071)$.

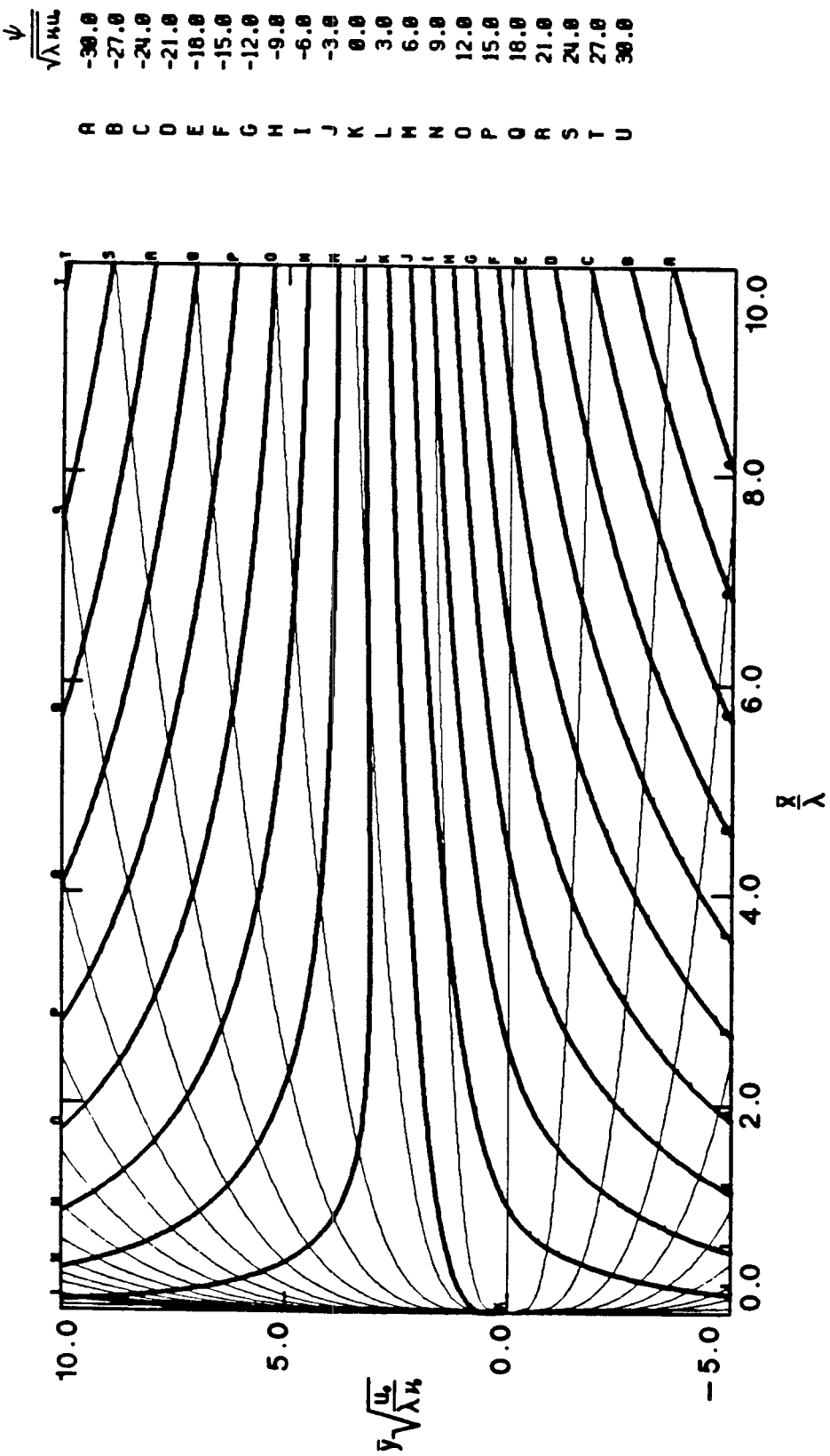

Figure (3.17) Streamline Patterns for a Diffusion Flame with $\varphi = 0.058$, $\beta = 0.5$ $(K'(0^+) = 0.113)$.

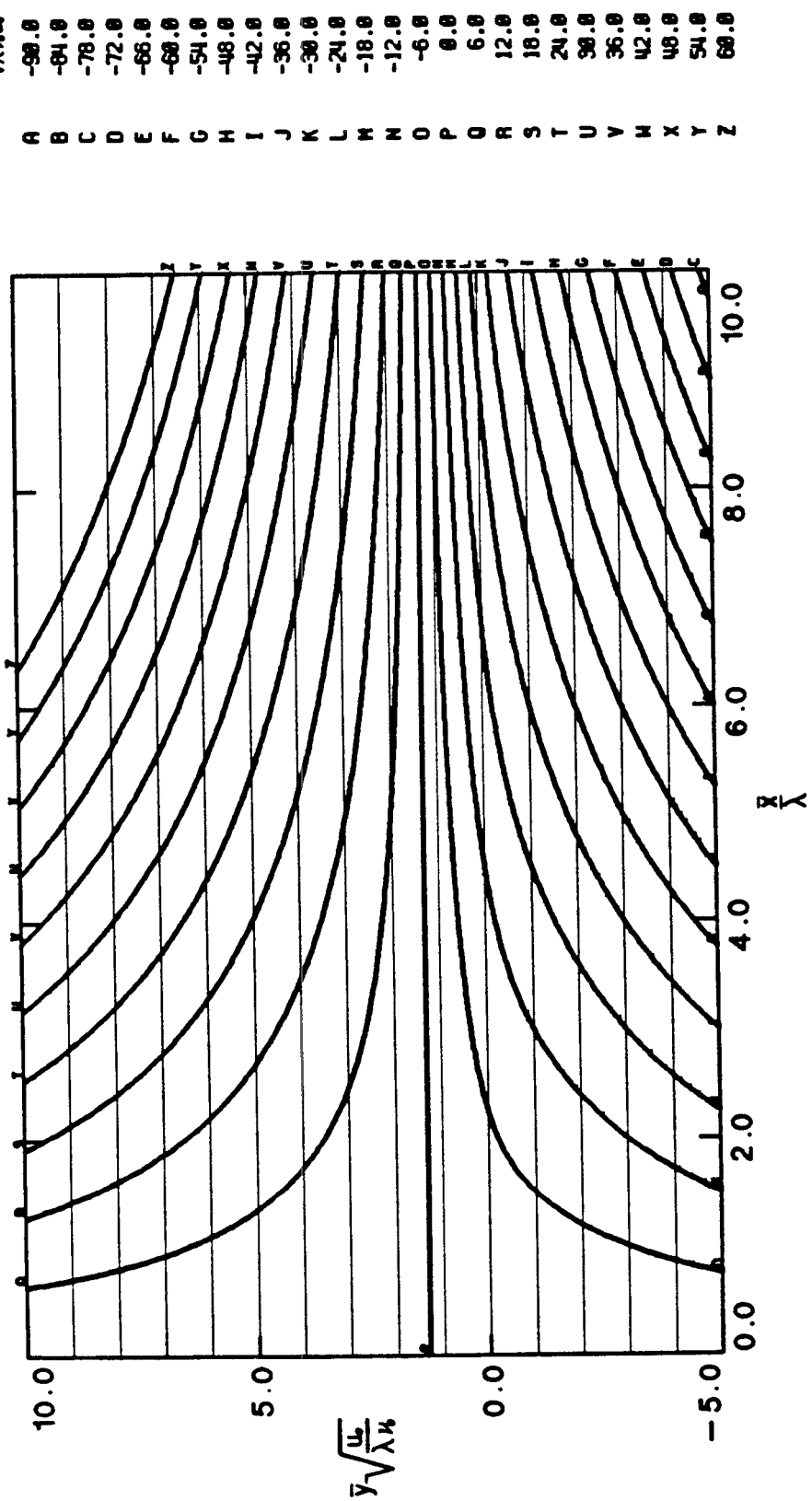

Figure (3.18) Streamline Patterns for a Diffusion Flame with $\varphi = 0.058$, $\beta = 1.0$ $(K'(0^+) = 0.134)$.

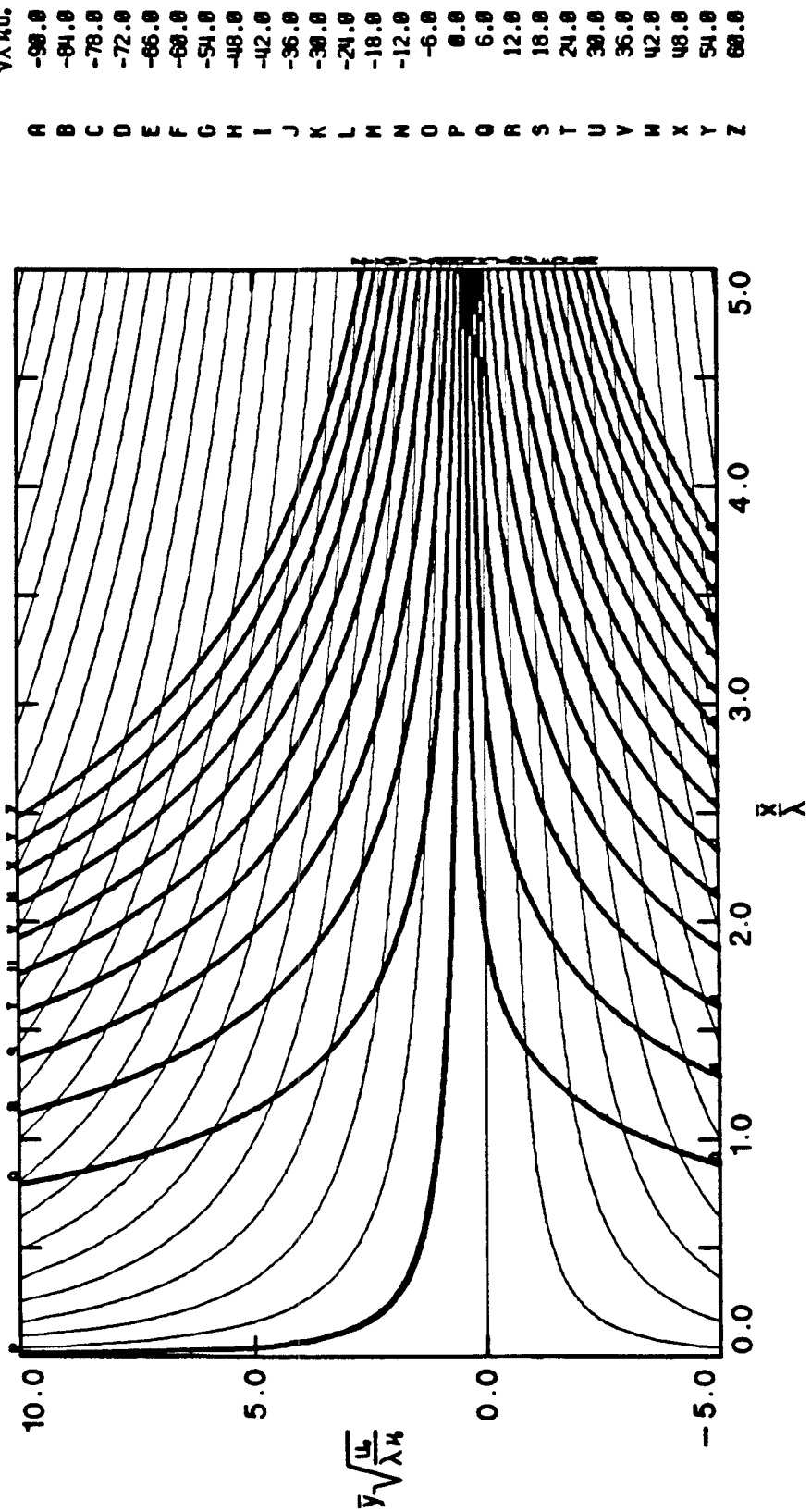

Figure (3.19) Streamline Patterns for a Diffusion Flame with $\varphi = 0.058$, $\beta = 2.0$ $(K'(0^+) = 0.168)$.

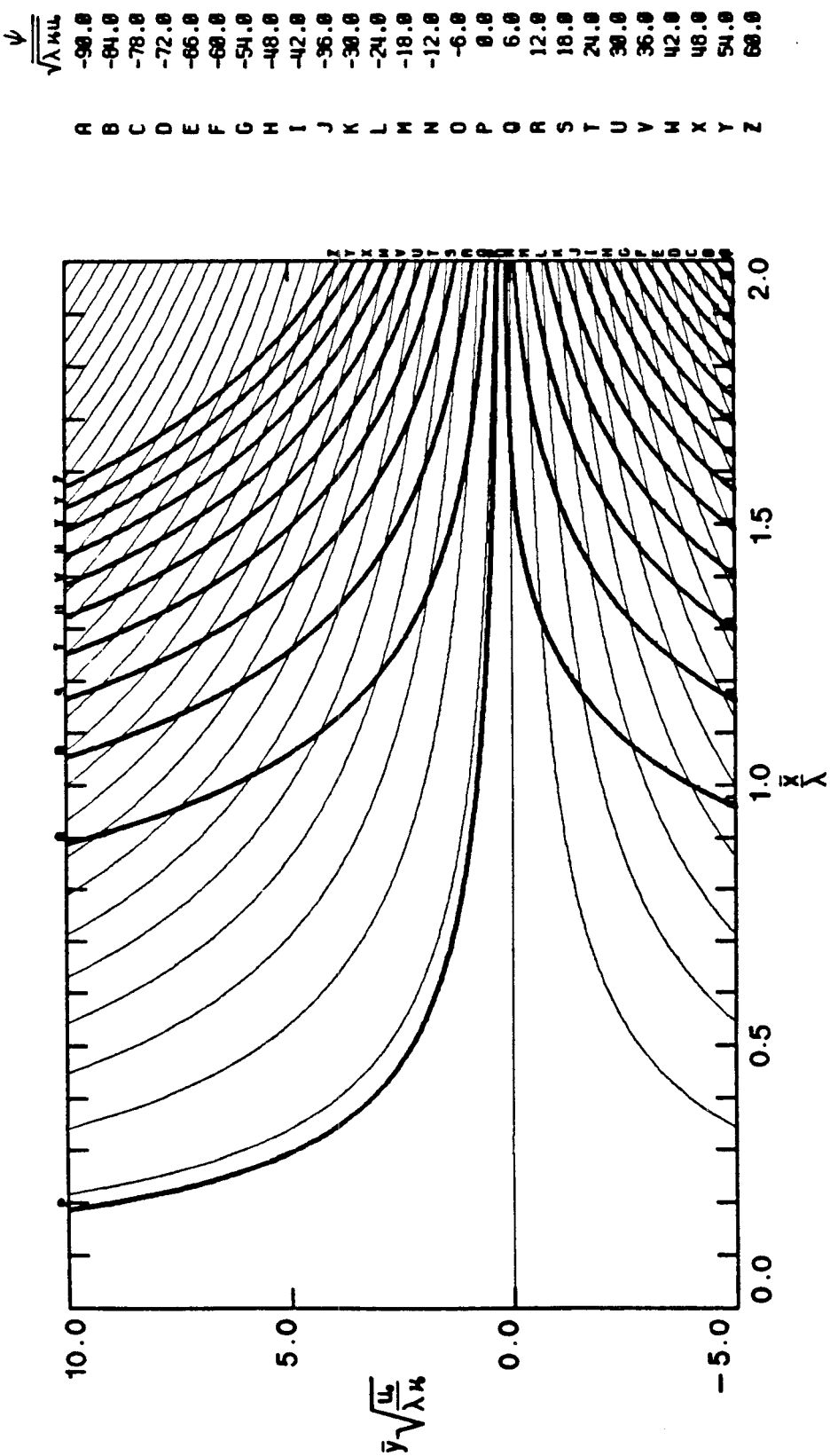

Figure (3.20) Streamline Patterns for a Diffusion Flame with $\varphi = 0.058$, $\beta = 4.0$ $(K'(0^+) = 0.219)$.

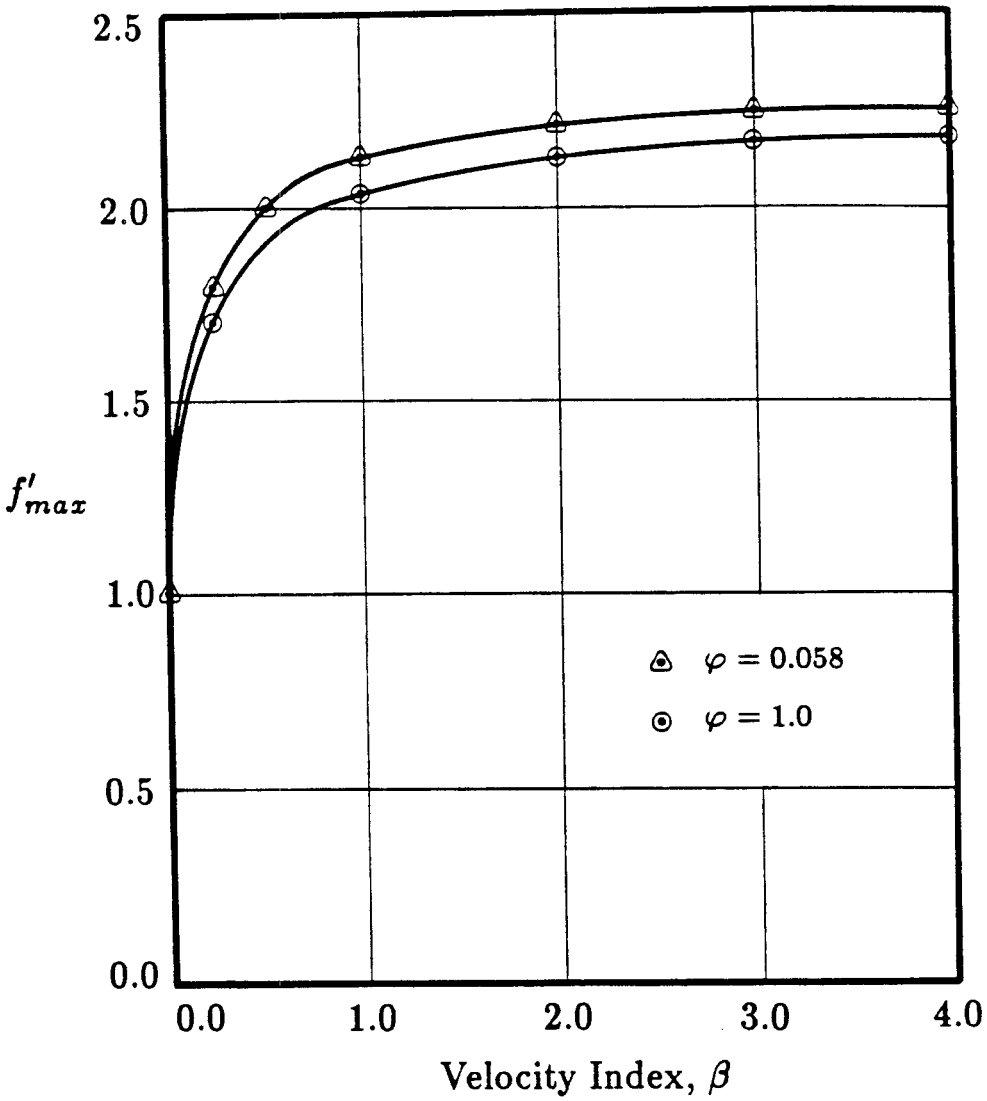

Figure (3.21) Maximum Value of the Dimensionless Streamwise Velocity (f'_{max}) as a Function of the Velocity Index, β.

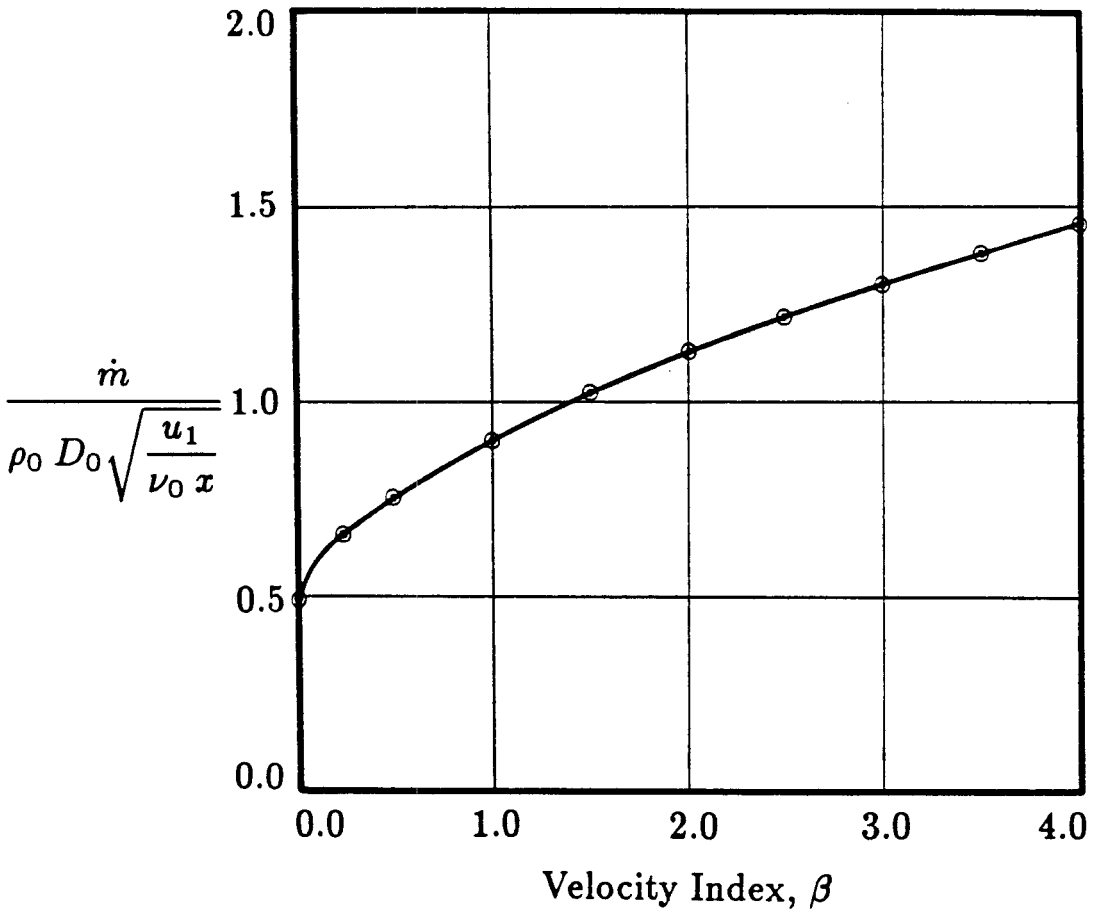

Figure (3.22) Dimensionless Fuel Mass Consumption Rate as a Function of the Velocity Index, β $(\varphi = 1.0)$.

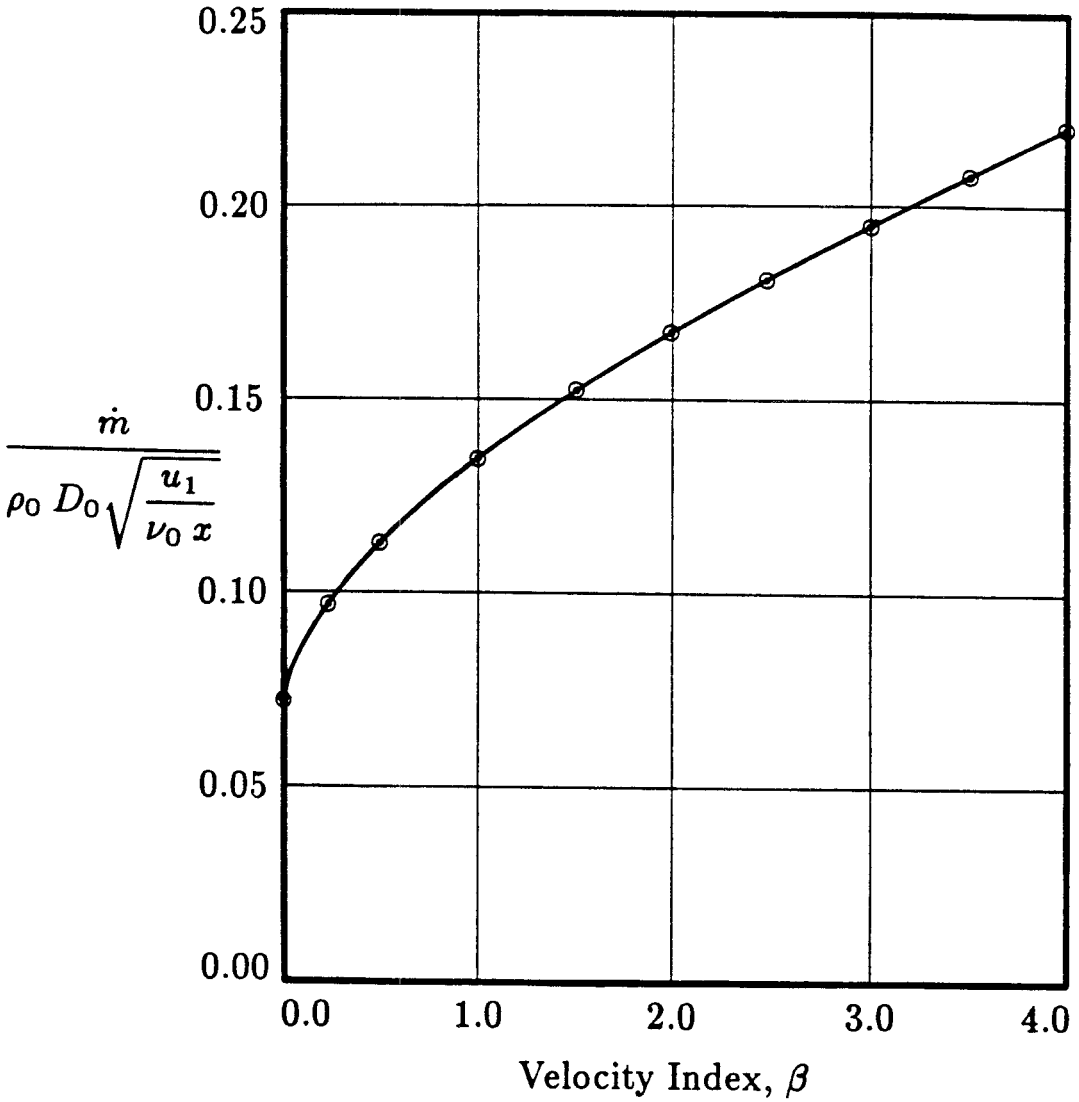

Figure (3.23) Dimensionless Fuel Mass Consumption Rate as a Function of the Velocity Index, β $(\varphi = 0.058)$.

β	$\frac{\dot{m}_f}{\rho_0 D_0 \sqrt{\frac{u_1}{\nu_0 x}}}$	$\frac{\dot{m}_{\varepsilon_0}}{\rho_0 D_0 \sqrt{\frac{u_1}{\nu_0 x}}}$	$\frac{\dot{m}_f}{\dot{m}_{\varepsilon_0}}$	$\frac{\dot{m}_{str}}{\rho_0 D_0 \sqrt{\frac{u_1}{\nu_0 x}}}$	$\frac{\dot{m}_f}{\dot{m}_{str}}$
0.10	0.587	0.261	2.25	0.611	0.96
0.25	0.670	0.446	1.50	0.706	0.95
0.50	0.764	0.662	1.15	0.811	0.94
0.75	0.840	0.811	1.04	0.895	0.94
1.00	0.907	0.968	0.94	0.968	0.94
1.50	1.026	1.201	0.85	1.097	0.94
2.00	1.130	1.397	0.81	1.210	0.93
2.50	1.225	1.569	0.78	1.313	0.93
3.00	1.313	1.724	0.76	1.407	0.93
3.50	1.396	1.866	0.75	1.496	0.93
4.00	1.473	1.998	0.74	1.580	0.93

Table 3.1 **Comparison of the Fuel Mass Consumption Rate of a Diffusion Flame in a Favorable Pressure Gradient with that of the Strained Flame Approximation, $\varphi = 1.0$.**

β	$\frac{\dot{m}_f}{\rho_0 D_0 \sqrt{\frac{u_1}{\nu_0 x}}}$	$\frac{\dot{m}_{\varepsilon_0}}{\rho_0 D_0 \sqrt{\frac{u_1}{\nu_0 x}}}$	$\frac{\dot{m}_f}{\dot{m}_{\varepsilon_0}}$	$\frac{\dot{m}_{str}}{\rho_0 D_0 \sqrt{\frac{u_1}{\nu_0 x}}}$	$\frac{\dot{m}_f}{\dot{m}_{str}}$
0.25	0.098	0.070	1.40	0.110	0.89
0.50	0.113	0.103	1.10	0.127	0.89
0.75	0.124	0.130	0.95	0.140	0.89
1.00	0.134	0.152	0.88	0.152	0.88
1.50	0.152	0.189	0.80	0.173	0.88
2.00	0.168	0.221	0.76	0.191	0.88
2.50	0.182	0.248	0.73	0.208	0.88
3.00	0.195	0.273	0.71	0.223	0.88
3.50	0.208	0.296	0.70	0.237	0.88
4.00	0.219	0.317	0.69	0.251	0.87

Table 3.2 **Comparison of the Fuel Mass Consumption Rate of a Diffusion Flame in a Favorable Pressure Gradient with that of the Strained Flame Approximation, $\varphi = 0.058$.**

Chapter 4

The Structure of a Diffusion Flame in an Adverse Pressure Gradient

The diffusion flame in an adverse pressure gradient exhibits features qualitatively similar to other, related boundary layer flows which have been studied before. Hartree (1937) found that the incompressible boundary layer equations have no solutions for the pressure gradient parameter $\beta < -0.0904$, this value corresponding to the point at which the shear stress at the surface vanishes (which is an indication of separation of the boundary layer for steady flows).

Stewartson (1954) found a second branch of solutions to the equations for $-0.0904 < \beta < 0$, these solutions corresponding to separated flows for which the shear stress at the surface is negative (implying that the velocity of the fluid close to the surface is opposite in direction to that of the free stream). Cohen and Reshotko (1955) found a similar situation in their studies of compressible boundary layers with heat transfer. They found that, with heat addition, separation occurred sooner (ie. for values of $\beta > -0.0904$) than in boundary layers without heat addition. This happens because, as in boundary layers with combustion, the high temperature, low density fluid in the vicinity of the surface responds more readily to the applied pressure gradient. The opposite effect is true when heat is transfered from the fluid into the surface.

As for the diffusion flame in a favorable pressure gradient, solutions to the field equations for adverse pressure gradients were obtained for $\frac{T_f}{T_0} = 7$,$Pr = 0.72$, $\varphi = 1$ and 0.058. Plots for all the significant flow field variables are shown in figs(4.1)–(4.6) for $\varphi = 1$ and figs(4.7)–(4.14) for $\varphi = 0.058$.

Now even though the flow field being considered extends from $y = -\infty$ to $y = +\infty$, it is more convenient to think of the pressure gradient as being imposed on the flow field by a channel of increasing area. The flow field consists of a viscous/thermal layer in the vicinity of the flame, and outer, irrotational fuel and oxidizer fields. Streamlines for the

flow fields are shown in figs(4.15)–(4.28), the dark lines being the streamlines and the lighter lines constant values of the similarity variable η. The line $\eta = 0$ corresponds to the horizontal axis (where the flame is located), positive values of η in increments of 2 are located in the upper half plane and negative values in the lower half plane. The channel walls would correspond to streamlines, the lower wall corresponding to a free streamline in the outer oxidizer field and the upper corresponding to a free streamline in the outer fuel flow field (eg. streamlines A and U in figs(4.15)–(4.19)). If the flame were absent, the entire flow field would be irrotational and of constant density so that the channel area needed to produce the required pressure gradient could be obtained from mass conservation

$$A(x) = \frac{\dot{m}}{\rho_0 \, u_0 \, \left(\frac{\overline{x}}{\lambda}\right)^{\beta}} \quad . \tag{4.1}$$

Both the velocity deficit and the high temperature in the vicinity of the flame tend to increase the channel area required to contain the flow field for a specified pressure gradient. The viscous/thermal layer can be replaced by an equivalent body of thickness δ^*, the displacement thickness, where

$$\delta^*(x) = \int_{y_a}^{y_b} \left(1 - \frac{\rho u}{\rho_0 u_0}\right) \, dy' \tag{4.2}$$

(where y_a and y_b are the channel boundaries or any two points, one in the oxidizer free stream, the other in the fuel free stream, since the integrand is zero here) or in terms of the similarity variables

$$\delta^*(x) = \left(\frac{\nu_0 \, \overline{x}}{u_1}\right) \int_{-\infty}^{\infty} \left(\left(\left(\frac{T_f}{T_0} - 1\right) \vartheta + 1\right) - f'\right) \, d\eta' \tag{4.3}$$

The total channel area required to contain the flow field with chemical reaction is therefore

$$A_t(x) = A(x) + \delta^*(x) \tag{4.4}$$

where $A(x)$ is now the equivalent channel area "felt" by the outer, irrotational flow field (see fig(4.29)). This equivalent representation of the flow field will be used in an attempt

to explain its behavior as the pressure gradient parameter β (or the channel area $A_t(x)$) is varied.

Fig(4.2) ($\varphi = 1$, $\beta = -0.0248$) shows that the high temperature, low density fluid in the vicinity of the flame is retarded more than the high density fluid in the free stream. Because $Pr = Sc = 0.72$ (which is close to 1.0) the viscous, diffusion and thermal zones have similar thicknesses. An increase in the width of the viscous layer is therefore accompanied by increases in the widths of the diffusion zones, decreasing the concentration gradients of both fuel and oxidizer and hence decreasing the fuel mass consumption rate at the flame. The non–dimensional mass consumption rate of fuel

$$\frac{\dot{m}_f}{\rho_0 D_0 \left(\frac{u_1}{\nu_0 x}\right)^{\frac{1}{2}}} = \frac{\partial K_1}{\partial \eta}(0^+) \tag{4.5}$$

is plotted against the pressure gradient parameter β for $\varphi = 1$ in fig(4.30). Here it can clearly be seen that as β is decreased from 0.0 to -0.0248, a decrease in fuel consumption occurs.

The displacement thickness of the layer

$$\frac{\delta^*}{\left(\frac{\nu_0 \, \overline{x}}{u_1}\right)^{\frac{1}{2}}} = \int_{-\infty}^{\infty} \left(\left(\left(\frac{T_f}{T_0} - 1 \right) \vartheta + 1 \right) - f' \right) \, d\eta' \tag{4.6}$$

is plotted against β for $\varphi = 1$ in fig(4.32). Decreasing the value of β from 0.0 to -0.0248 has the effect of increasing the widths of both the viscous and thermal layers, both of which have the effect of increasing the displacement thickness. Because the value of β has decreased from 0.0 to -0.0248, the area $A(x)$ "felt" by the outer, irrotational fluid has increased. This implies that the increase in the total area $A_t(x)$ more than compensates for the increase in the displacement thickness δ^*.

Because the curve of δ^* agianst β has a vertical tangent in the vicinity of $\beta = -0.0283$, an increase in the channel area $A_t(x)$ is accompanied by an increase of equal

magnitude in the displacement thickness, leaving $A(x)$ unchanged. The irrotational outer flow field therefore remains unchanged and the value of β remains constant. The curve of the normalized fuel mass consumption rate against β also has a vertical tangent since the widths of the diffusion zones are increasing but the value of β remains constant. As δ^* increases above its value at $\beta = -0.0283$, the graph of δ^* against β curves back toward larger values of β. This implies that the increase in the displacement thickness is larger than the increase in the total channel area, resulting in a smaller equivalent channel area for the outer, irrotational flow field and hence the increased value for β. This trend continues as δ^* increases and β eventually tends to zero as δ^* becomes large. Each value of the pressure gradient parameter β therefore has two solutions to the equations associated with it. One solution (the lower branch of the δ^* vs. β curve) corresponds to a flow field with a narrow viscous/thermal layer and therefore high mass consumption rate (and therefore corresponds to the upper branch of the mass consumption vs. β curve). The other corresponds to a wider viscous/thermal layer and therefore has a lower fuel mass consumption associated with it (the lower branch of the mass consumption curve).

Consider now the behavior of the viscous layer on the upper and lower branches of the mass consumption vs. β curve. Fig(4.2) shows a typical solution of the flow field variables on the upper branch. As is expected, the minimum streamwise velocity decreases as the strength of the adverse pressure gradient is increased to its limiting value. However, even when the adverse pressure gradient has increased to its limiting strength, the minimum streamwise velocity is still significantly positive. This is different from the incompressible boundary layer in which the point of minimum β corresponds to the point of separation. The reason for this is probably that significant growth of the incompressible boundary layer occurs only close to the point of separation. It is therefore only close to this critical point that the boundary layer can affect the external stream. In the case of the the diffusion flame, significant boundary layer growth occurs

long before separation, and this has the observed effect on β.

On the lower branch, the minimum streamwise velocity continues to decrease even though the strength of the adverse pressure gradient is decreasing (i.e. β is increasing). This happens because the layer of hot gas is increasing in width, so it responds more readily to the applied pressure gradient. The effect of the increase in width of the layer more than compensates for the decrease in strength of the pressure gradient. It should also remembered that on the lower branch, even though β is increasing, the channel walls are being opened up (i.e. $A_t(x)$ is increasing). This can clearly be seen from the behavior of the outer streamlines in the flowfield as the value of β is increased. The value of the minimum streamwise velocity continues to decrease until the fluid at the flame stagnates at a value of $\beta = -0.0209$ (fig(4.4)). If β is increased above -0.0209, the fluid at the flame reverses in direction (fig(4.5),$\beta = -0.0197$). Increasing β increases the width of the region of reversed flow; fig(4.6), $\beta = -0.00014$ is a typical solution.

Fig(4.30) shows that the fuel mass consumption rate drops to zero as β goes to zero on the lower branch. This is due to two effects. The first is the expected drop in mass consumption as the width of the diffusion zone is increased. The second becomes clear when one considers the formation and development of the two reciculation zones surrounding the flame.

In order to understand the formation of the two recirculation zones, it is useful to consider simultaneously the behavior of the similarity stream function $f(\eta)$ depicted in figs(4.1)–(4.6) as β is increased. When the fluid at the flame stagnates (fig(4.4), $\beta = -0.0209$), the similarity stream function has a horizontal slope at $\eta = 0$. As β is increased above this value and the region of backflow is formed, the slope of $f(\eta)$ goes negative at $\eta = 0$. As one therefore goes through the point of "internal separation", the nature of the curve of $f(\eta)$ changes. Before separation $f(\eta)$ has one zero but after separation the function has three zeroes, the two additional zeroes located on either side

of $\eta = 0$. Now since the stream function for the flow field is given by the formula

$$\frac{\psi}{(\nu_0\, u_0\, \lambda)^{\frac{1}{2}}} = \left(\frac{\overline{x}}{\lambda}\right)^{\frac{\beta+1}{2}} f(\eta) \tag{4.7}$$

the two additional zero streamlines resulting from the additional zeroes of $f(\eta)$ will be located along the constant values of the similarity variable corresponding to the location of the zeroes of $f(\eta)$. The two additional zero streamlines formed are the boundaries which separate the recirculation zones from the outer, forward moving fluid (streamlines M in fig (4.20)).

Now, in order to understand the second mechanism of fuel mass consumption reduction mentioned earlier, it is useful to consider a fluid particle close to the flame entering the flow field depicted in fig(4.20) from a value of $\frac{\overline{x}}{\lambda}$ downstream of $\frac{\overline{x}}{\lambda} = 20$, say along streamline L. As the fluid particle moves along the streamline towards the origin, it encounters increasing values of η, the similarity variable. From the similarity plot corresponding to this flow field (fig(4.6)), it can be observed that increasing values of η correspond to larger vertical and smaller horizontal velocities. The particle continues to move in the direction of decreasing $\frac{\overline{x}}{\lambda}$ until it encounters the value of η corresponding to zero horizontal velocity. At this point, however, the vertical velocity is still positive, so the particle is carried into the the upper shear layer (where the horizontal velocity is positive) and convected downstream. The recirculation zone therefore convects partially reacted fluid outward, in opposition to the diffusion of reactants from the free stream toward the flame, resulting in the fuel mass consumption being driven to zero as the recirculation zone grows in size.

The presence of the recirculation zone has a different effect on the mass consumption rate for values of the stoichiometric fuel–air ratio other than unity (which are of more practical significance). Consider the graph of fuel mass consumption rate against the pressure gradient parameter for $\varphi = 0.058$ depicted in fig(4.31). The upper branch of

the curve resembles that for the case $\varphi = 1$ since the mechanism of mass consumption reduction is the same for the two cases (ie. the decrease in the species concentration gradients due to the widening of the viscous/diffusion zones). After separation on the lower branch the two curves exhibit different features. Whereas the curve for $\varphi = 1$ tends to zero as β goes to zero, the curve for $\varphi = 0.058$ reaches a minimum value at $\beta = -0.01$ and then increases as β goes to zero. By using the graphs showing the streamlines for the flow field (figs(4.21)–(4.28)) this behavior of the curve will be explained.

First consider fig(4.23) ($\beta = \beta_{min} = -0.025$) which is a solution typical of the lower branch of the mass consumption curve before separation occurs. A particle starting off close to $\frac{\overline{x}}{\lambda} = 0$ in the lower half plane (say on streamline F) moves toward the flame as it is convected downstream, reacts at the flame and moves into the upper half plane into the region of low streamwise velocity signified, in this diagram, by the region in which the streamlines are widely separated. Fig(4.10) shows the equivalent streamline diagram corresponding to a value of β slightly larger than that at which the streamwise velocity goes to zero. As in the previous case, consider a particle starting off close to $\frac{\overline{x}}{\lambda} = 0$ in the lower half plane. Again the particle is convected through the flame into the upper half plane. The particle continues to move forward and upward, encountering increasing values of the similarity variable η. It continues moving in this fashion until it encounters the value of η at which the horizontal velocity goes to zero ($\eta \approx 4$). At this point the vertical velocity is still positive, so the particle is transported into the the region of reversed flow between $\eta = 4$ and $\eta = 5$. The streamline along which the particle moves therefore curves backward until it encounters the value of η at which the streamwise velocity again goes to zero. Since the vertical velocity is still positive, the particle is transported into the region of positive streamwise velocity and is then convected downstream in the shear layer furthest from the flame. Fig(4.11) shows the streamline plot for a case in which the reversed flow region is wider than in the case described

before. The streamlines show the same behavior as before, the effects of stagnation and reversed flow being more exagerated. If one now considers the similarity streamfunction corresponding to these flow fields, one observes that even though the streamwise velocity has gone to zero, the similarity streamfunction still has only one zero, unlike the case $\varphi = 1$. However, as β is increased and the region of backflow increases, the portion of the similarity streamfunction curve between $\eta = 3$ and 6 moves upward until a new zero of $f(\eta)$ is generated when the curve touches the horizontal axis. By considering, in sequence, the streamline plots fig(4.24)–(4.28) for increasing β, the effect of the above mentioned behavior of the similarity streamfunction on the flowfield can be observed. The point at which a particular streamline curves backward into the region of reversed flow moves downstream as β is increased. In fig(4.26) this distance has increased to such an extent that a particle on streamline I moves downstream to values of $\frac{\overline{x}}{\lambda} > 20$ (and therefore out of the range of the graph) before it eventually curves back. At a critical value of β corresponding to the point at which the function $f(\eta)$ touches the horizontal axis and a new zero of $f(\eta)$ is generated, a particle moving along streamline I continues to move downstream and does not change direction at all. The new zero streamline generated separates the lower, forward moving stream from the upper, single region of recirculation. Now, as β is increased , this single new zero streamline bifurcates, the two new streamlines forming the boundaries of a second recirculation zone, the initiation of which can be observed in fig(4.27) ($\beta = -0.01$). As β is increased above this value, the second recirculation zone grows in size until it is fully developed as depicted in fig(4.28).

The formation of the second recirculation zone accounts for the observed increase in the mass consumption rate for values of β between -0.01 and 0.0 on the lower branch. Consider fig(4.28) which shows the lower recirculation zone in fully developed form. This recirculation zone convects fluid from a region corresponding to a large value of the similarity variable (at which the fluid has a high concentration of fuel) toward the

flame, aiding the diffusion process in transporting fuel toward the flame, and therefore increasing the mass consumption of fuel at the flame. Even though the width of the diffusion zone for the fuel is increasing, the augmentation of the mass consumption rate by convection in the recirculation zone more than compensates for the loss due to the former. The asymmetric orientation of the recirculation zones therefore has an effect opposite to that of the symmetric recirculation zones for $\varphi = 1$. In the symmetric case it is the upper recirculation zone that causes the outward convection of partially reacted gases. In the asymmetric case this is still true, but the vertical velocity through the flame is large enough to displace the lower recirculation zone into the fuel side of the flow field. This location of the lower recirculation zone counteracts the effect of the upper zone on the mass consumption rate.

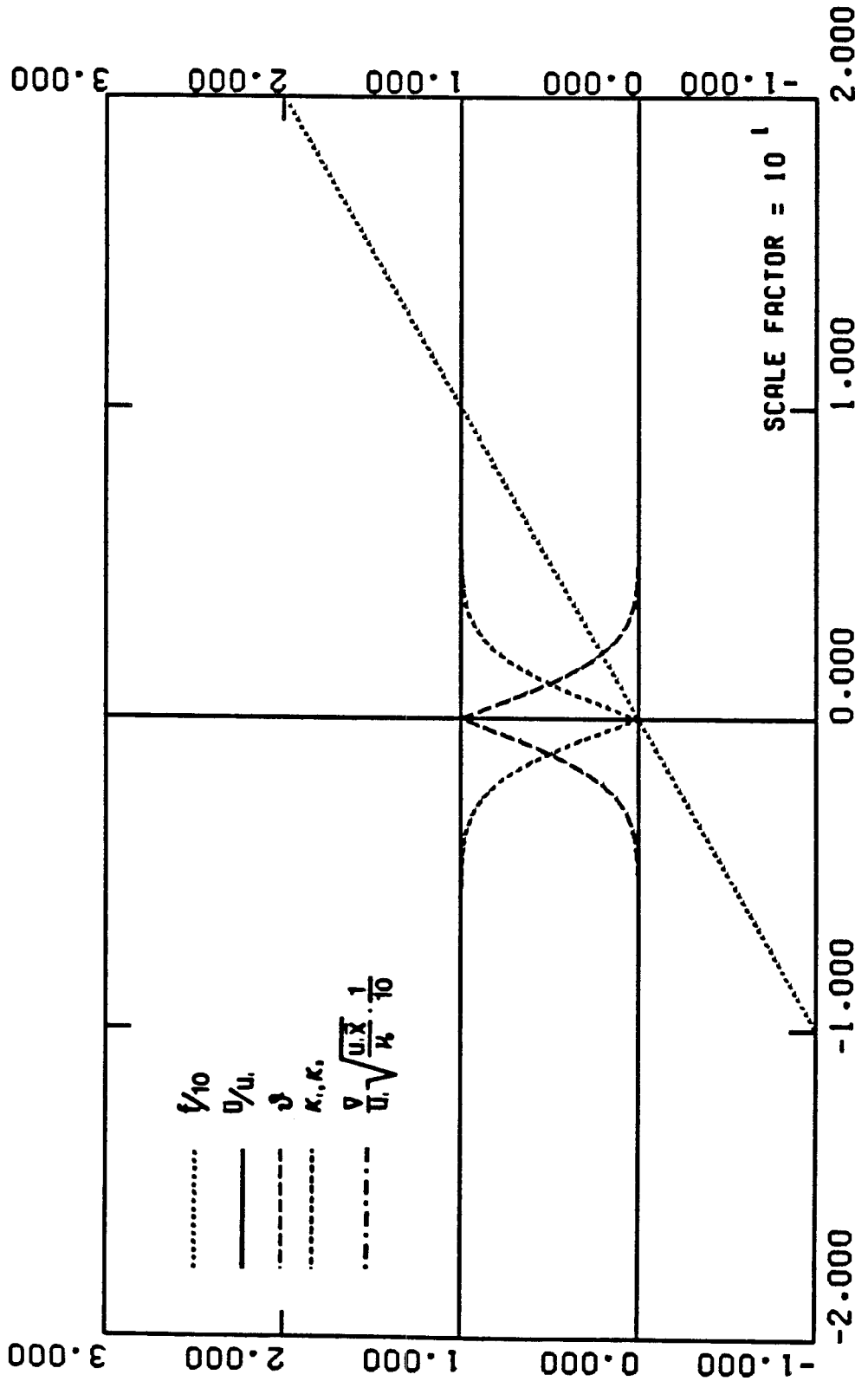

Figure (4.1) Distribution of Properties for a Diffusion Flame with $\varphi = 1.0$, $\beta = 0.0$ $(K'(0^+) = 0.478)$.

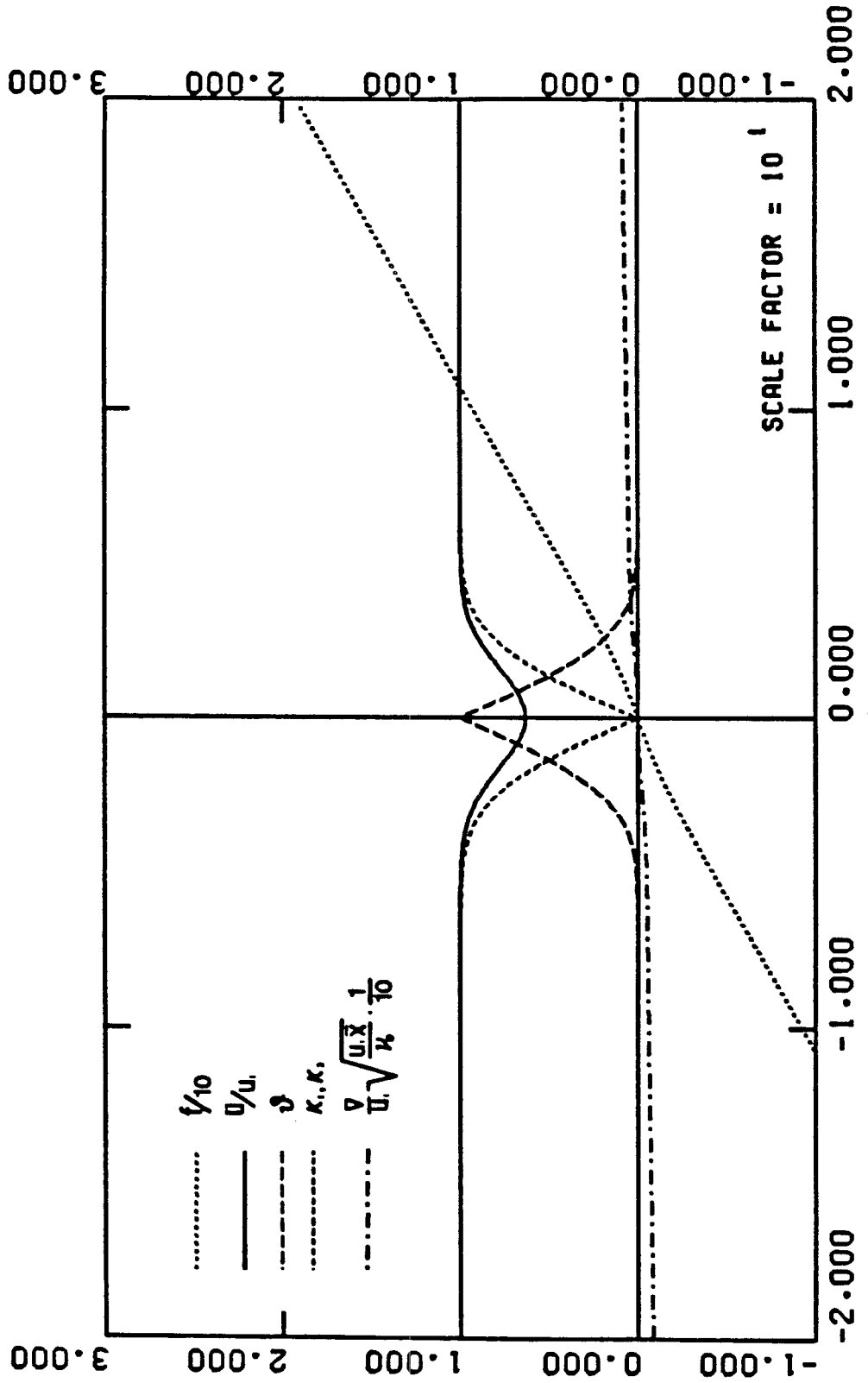

Figure (4.2) Distribution of Properties for a Diffusion Flame with $\varphi = 1.0$, $\beta = -0.0248$ $(K'(0^+) = 0.400)$.

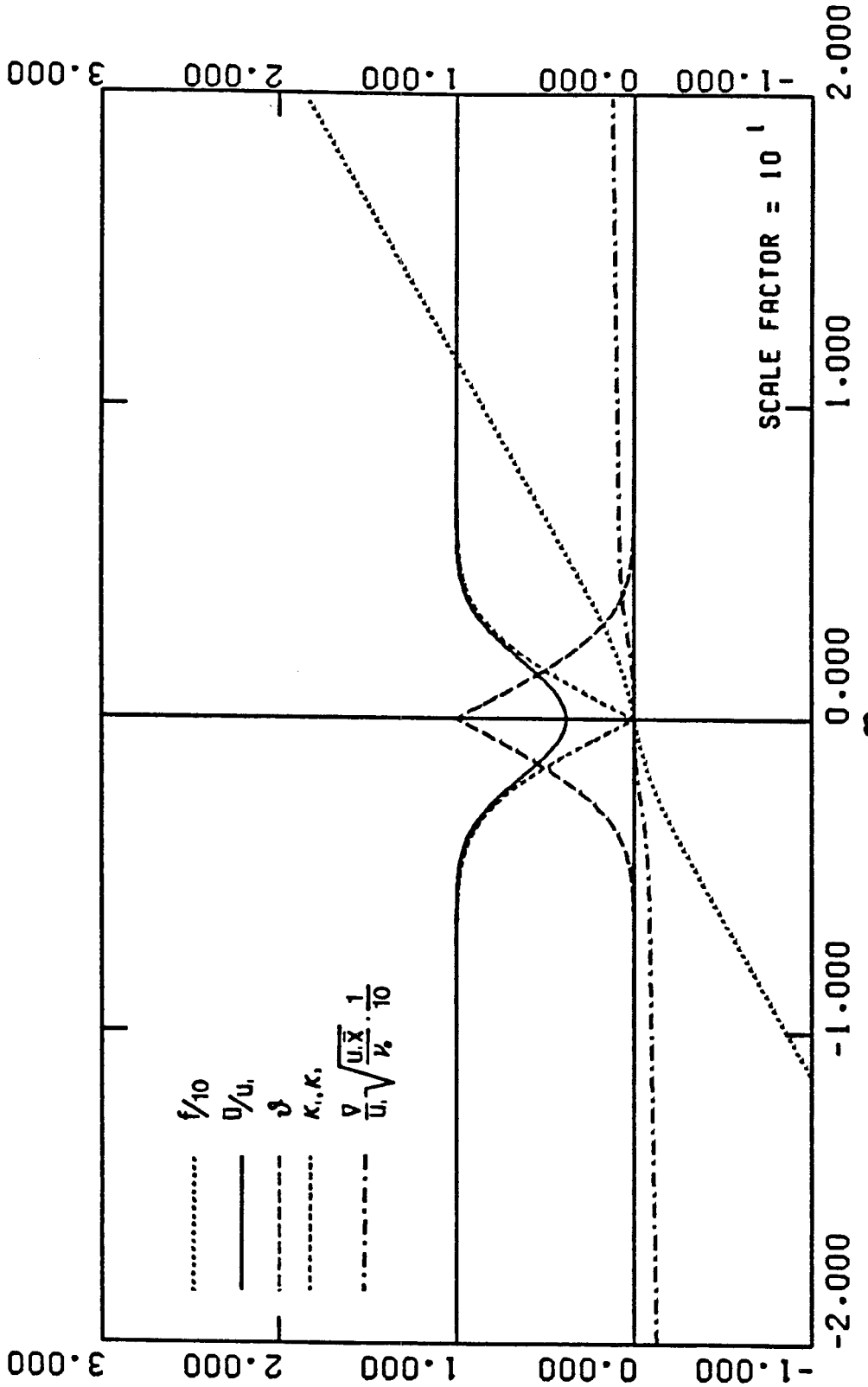

Figure (4.3) Distribution of Properties for a Diffusion Flame with $\varphi = 1.0$, $\beta = -0.0283$ $(K'(0^+) = 0.300)$.

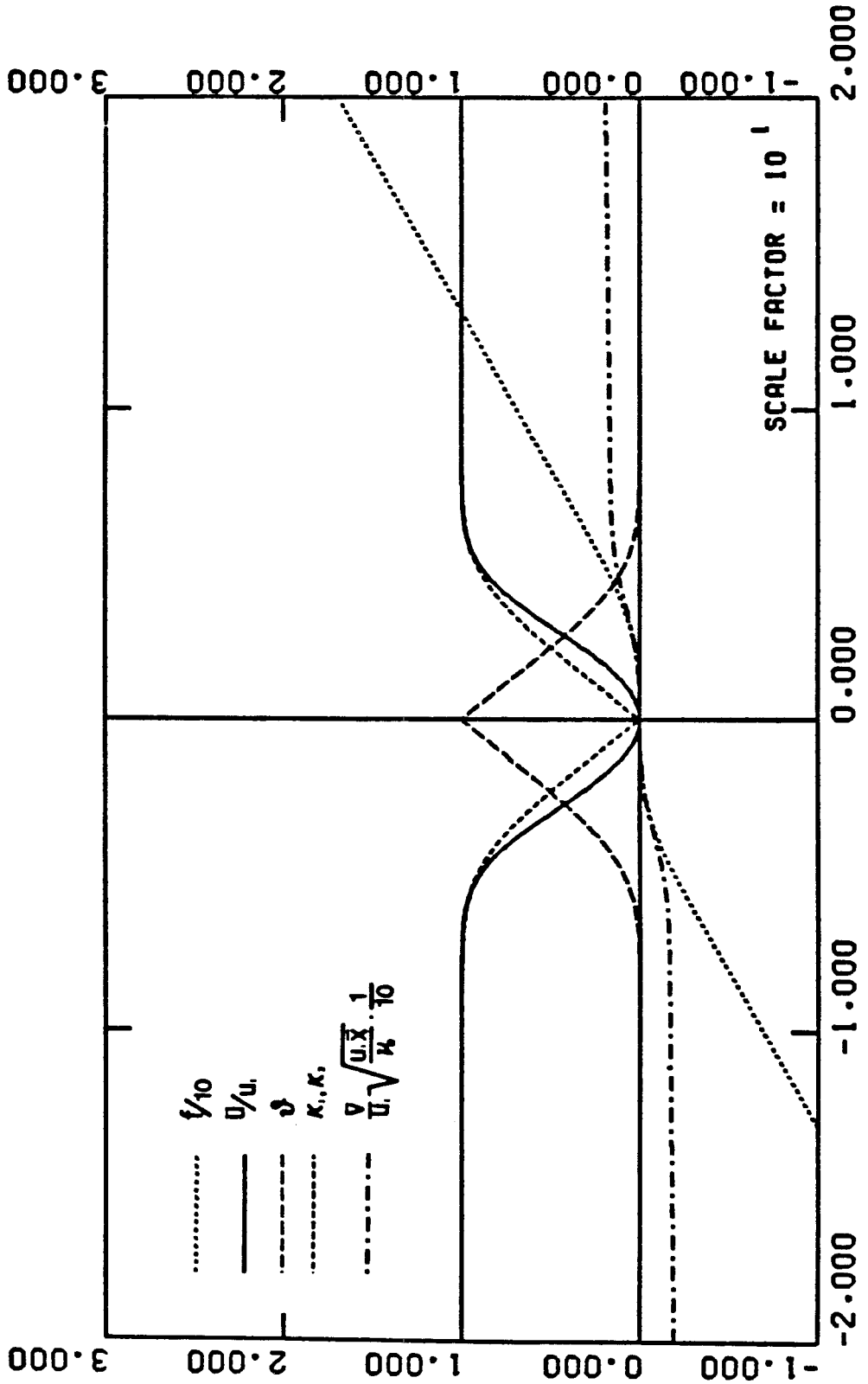

Figure (4.4) Distribution of Properties for a Diffusion Flame with $\varphi = 1.0$, $\beta = -0.0209$ $(K'(0^+) = 0.220)$.

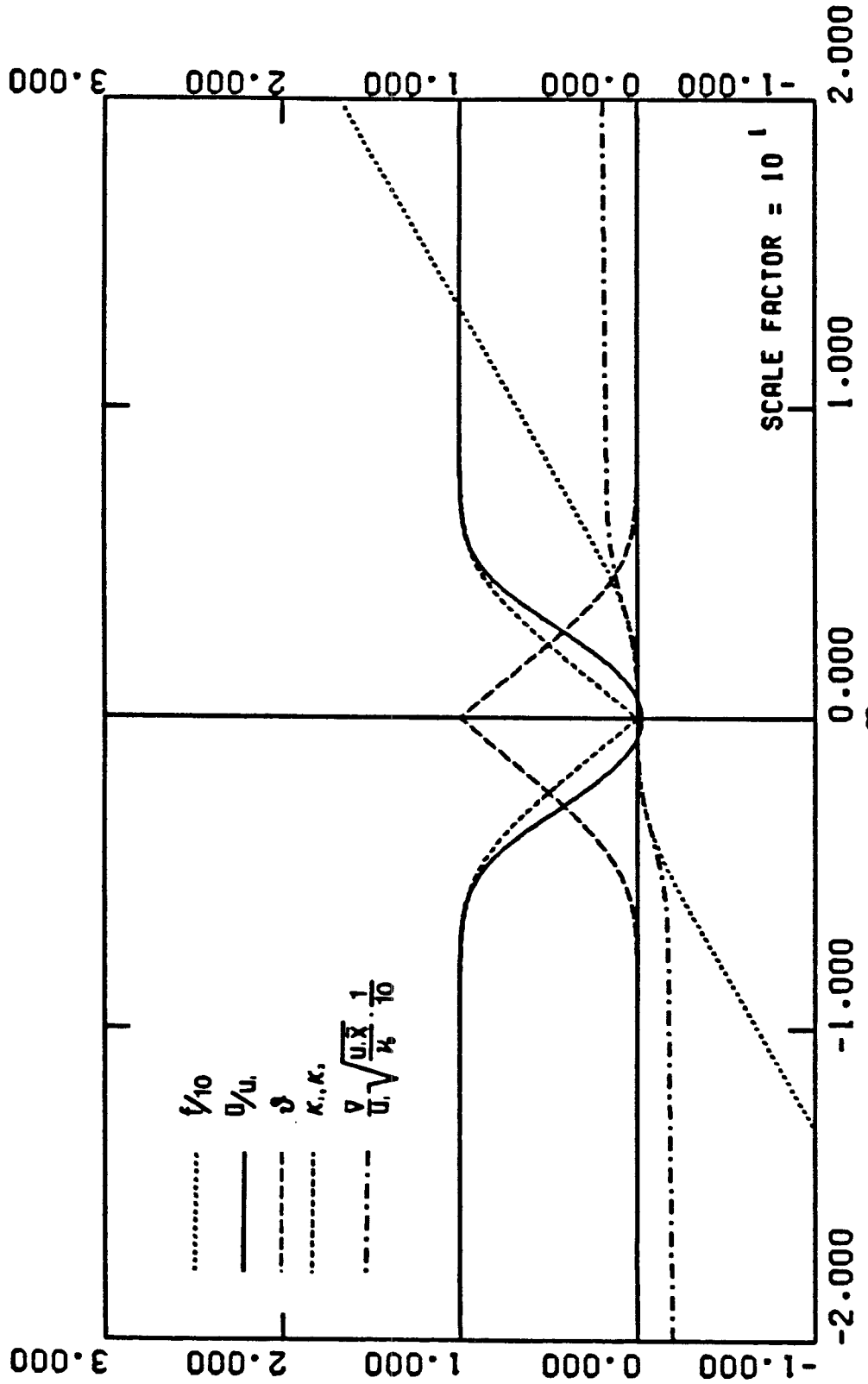

Figure (4.5) Distribution of Properties for a Diffusion Flame with $\varphi = 1.0$, $\beta = -0.0197$ $(K'(0^+) = 0.210)$.

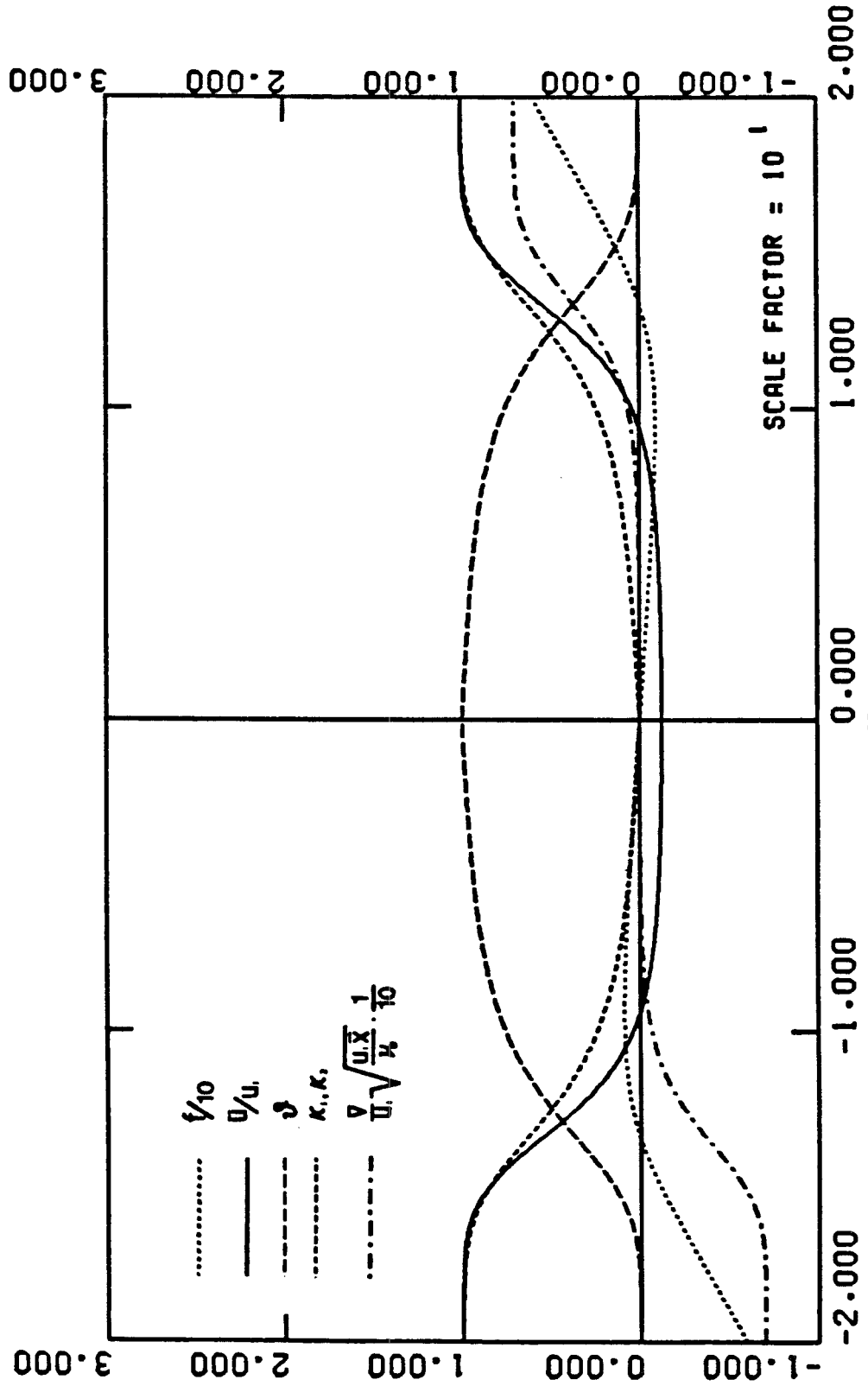

Figure (4.6) Distribution of Properties for a Diffusion Flame with $\varphi = 1.0$, $\beta = -0.00014$ $(K'(0^+) = 0.040)$.

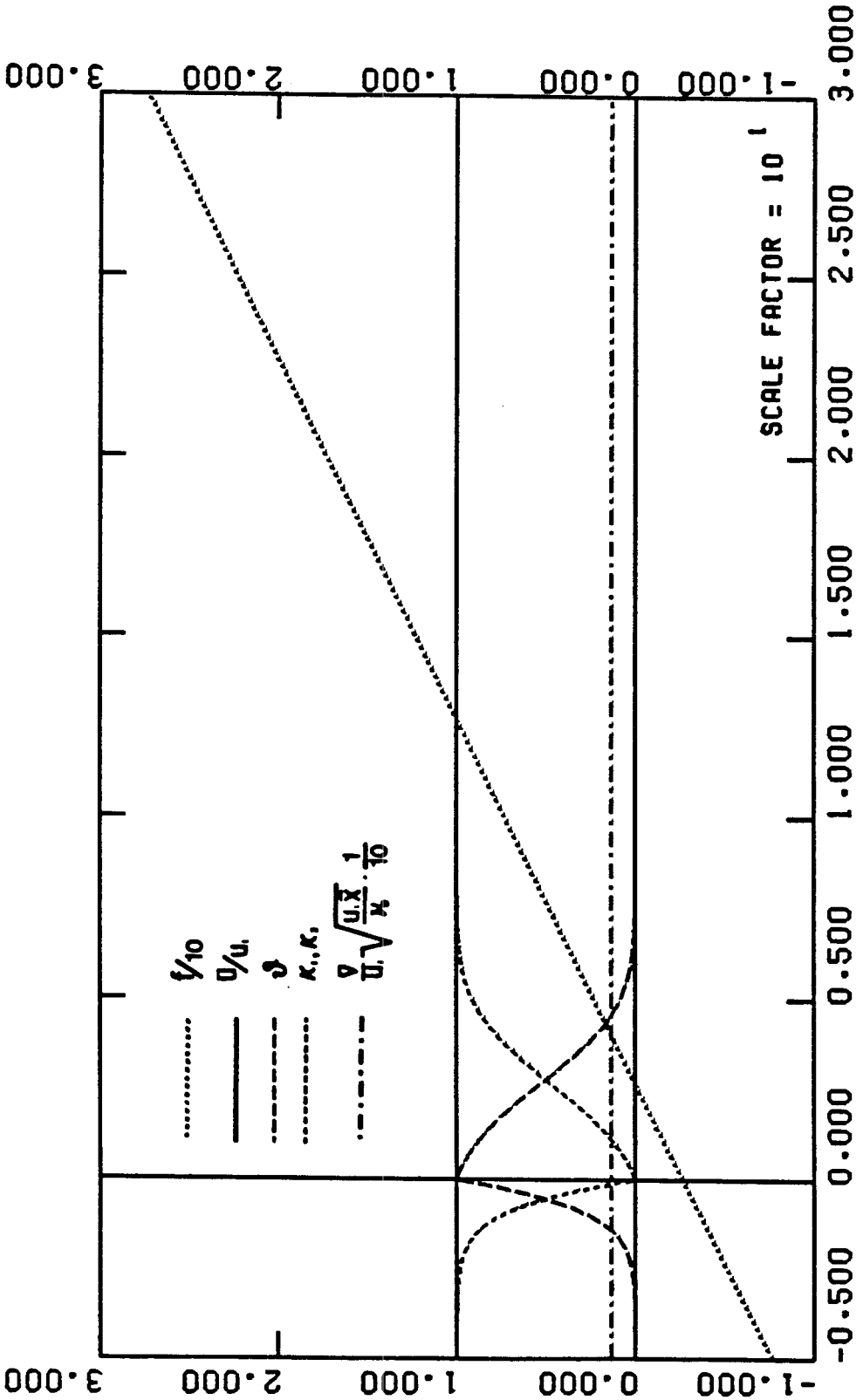

Figure (4.7) Distribution of Properties for a Diffusion Flame with $\varphi = 0.058$, $\beta = 0.0$ $(K'(0^+) = 0.0705)$.

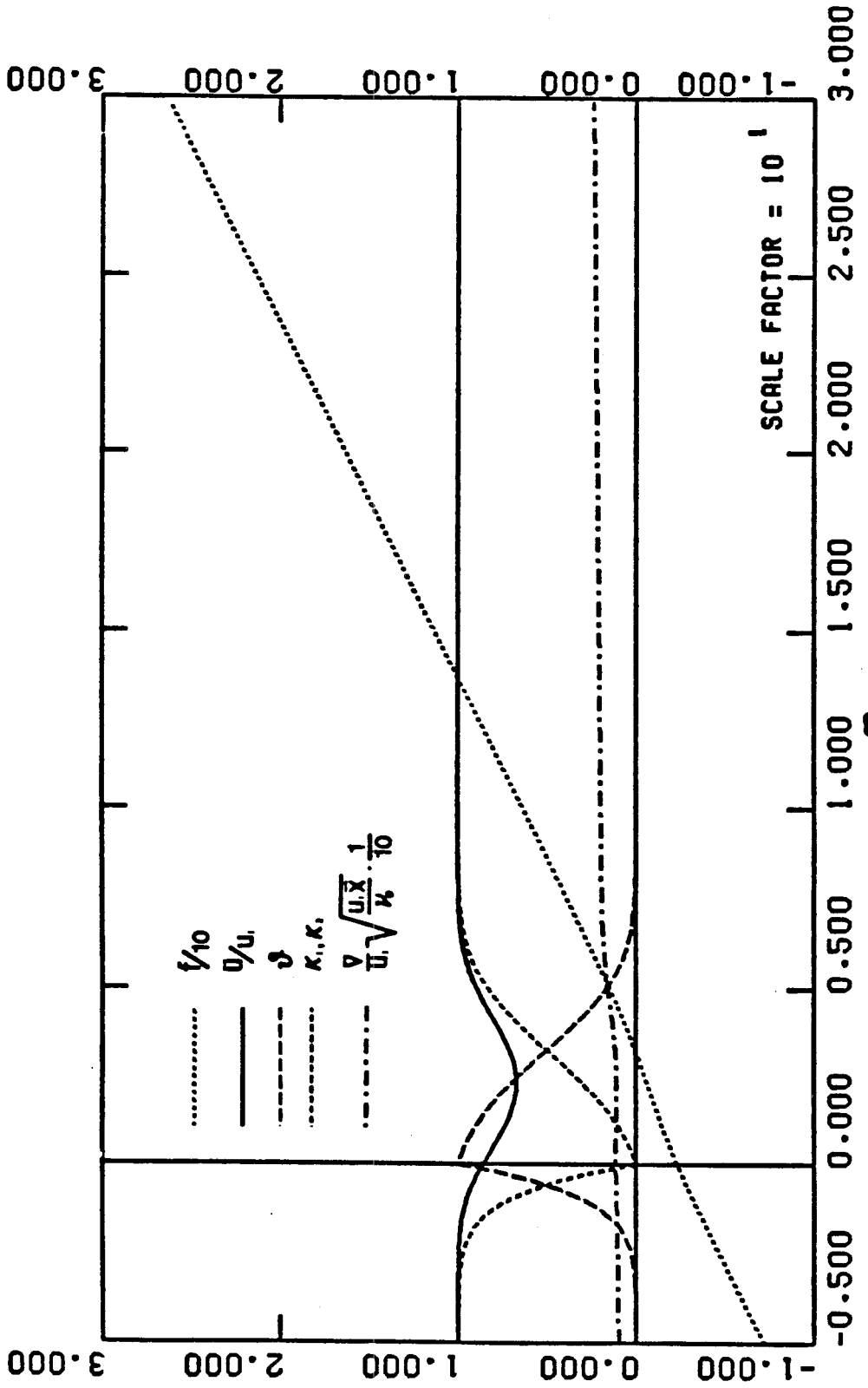

Figure (4.8) Distribution of Properties for a Diffusion Flame with $\varphi = 0.058$, $\beta = -0.020 \quad (K'(0^+) = 0.0621)$.

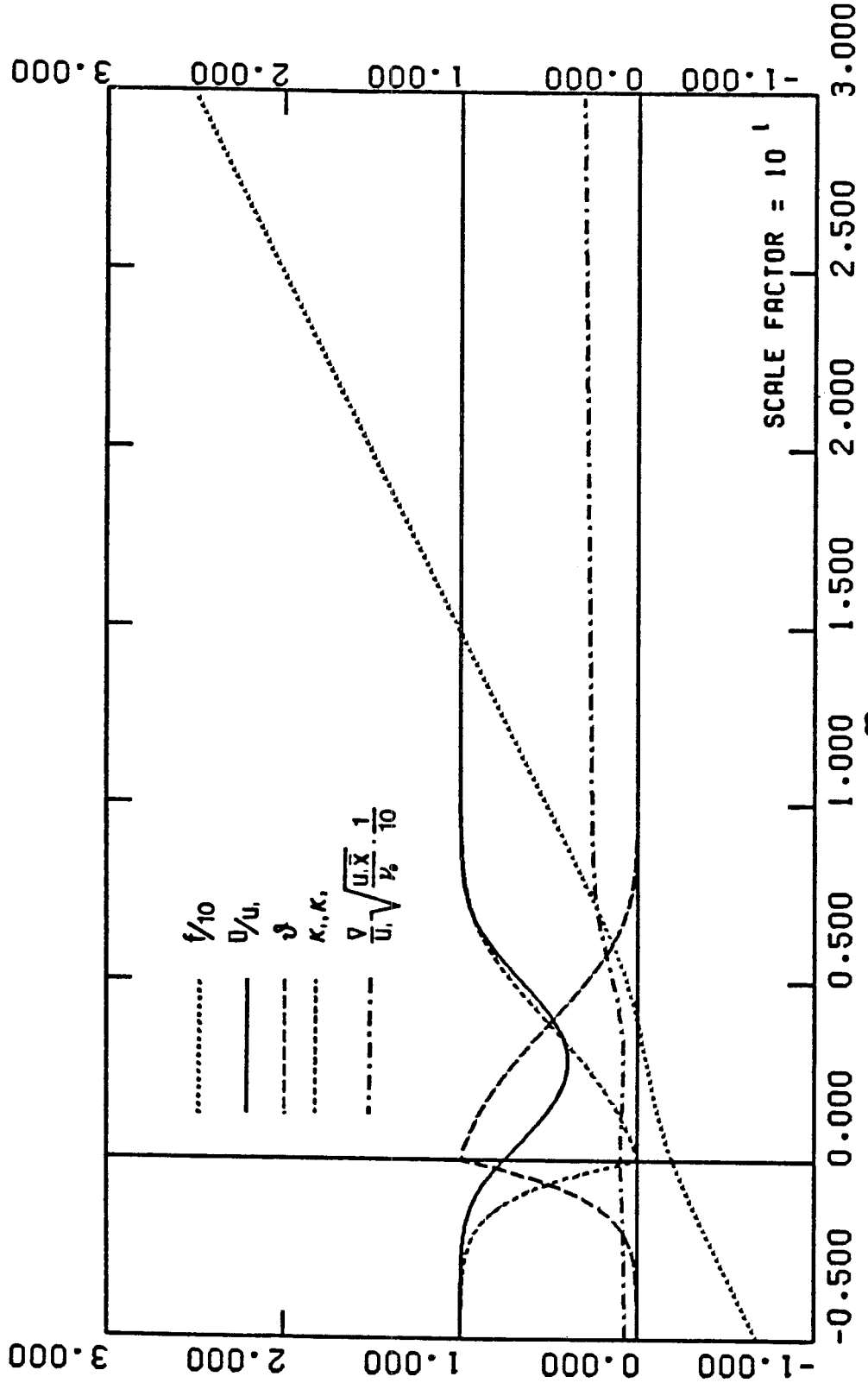

Figure (4.9) Distribution of Properties for a Diffusion Flame with $\varphi = 0.058$, $\beta = -0.025 \quad (K'(0^+) = 0.0555)$.

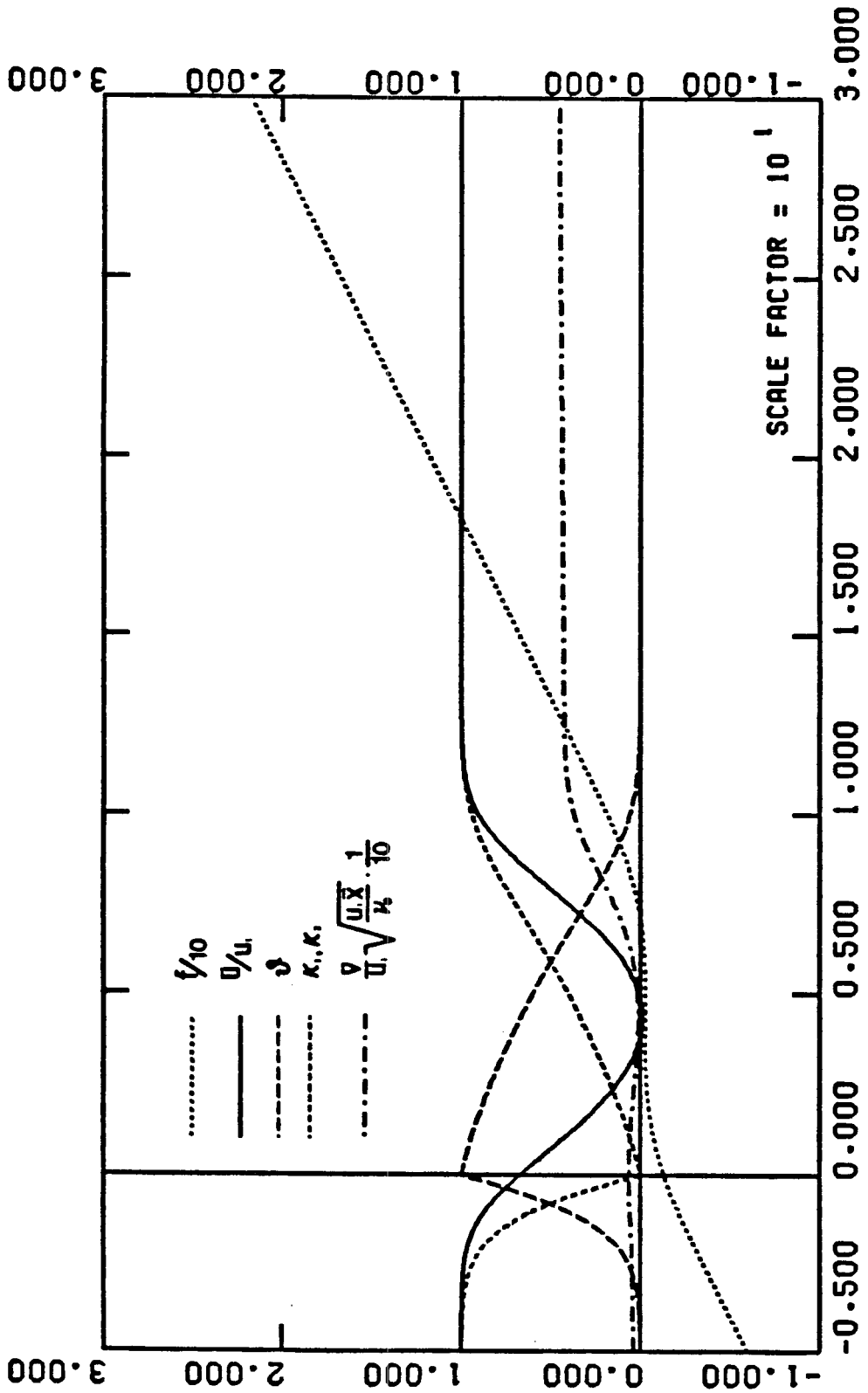

Figure (4.10) Distribution of Properties for a Diffusion Flame with $\varphi = 0.058$, $\beta = -0.017$ $(K'(0^+) = 0.0440)$.

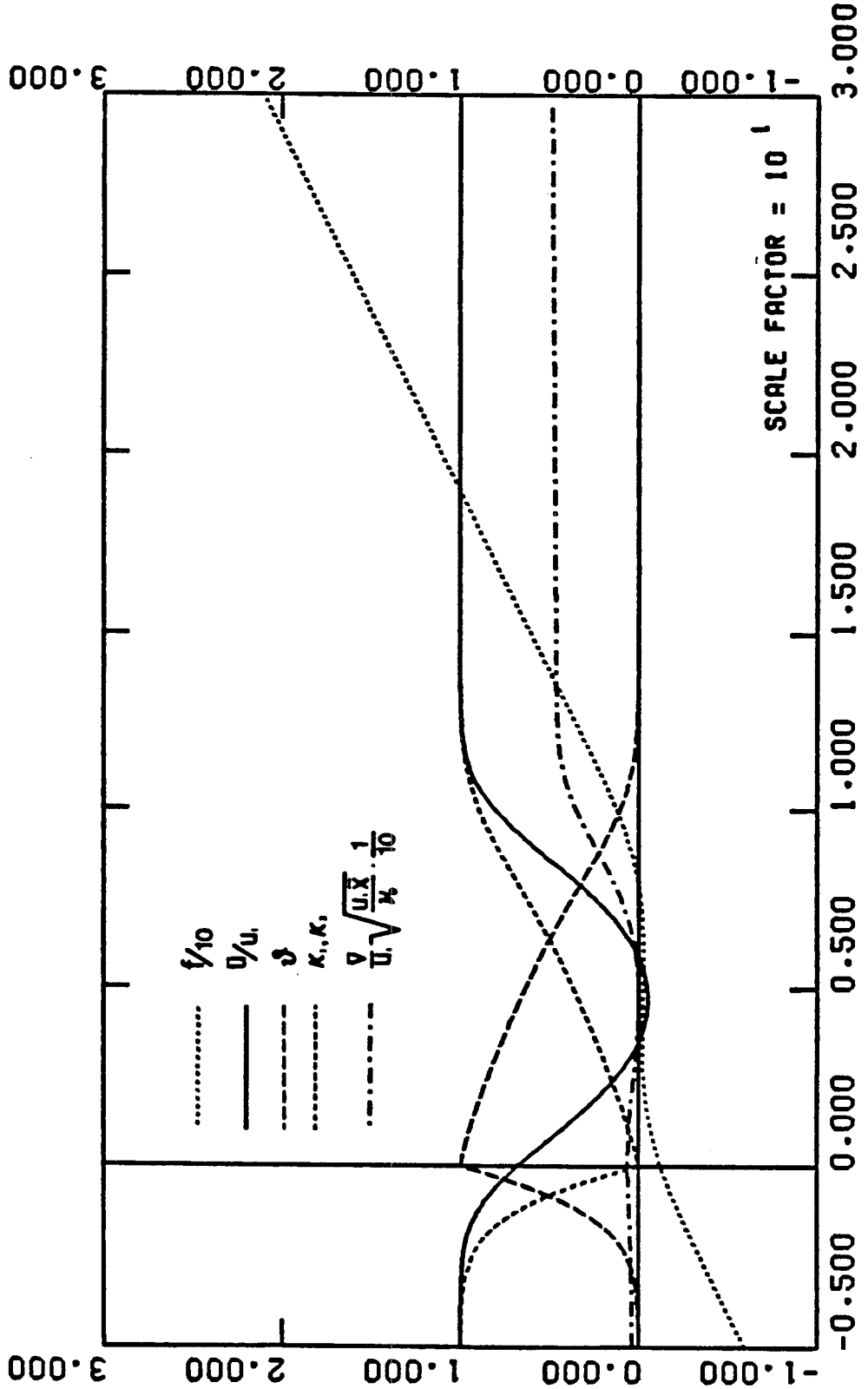

Figure (4.11) Distribution of Properties for a Diffusion Flame with $\varphi = 0.058$, $\beta = -0.015$ $(K'(0^+) = 0.0430)$.

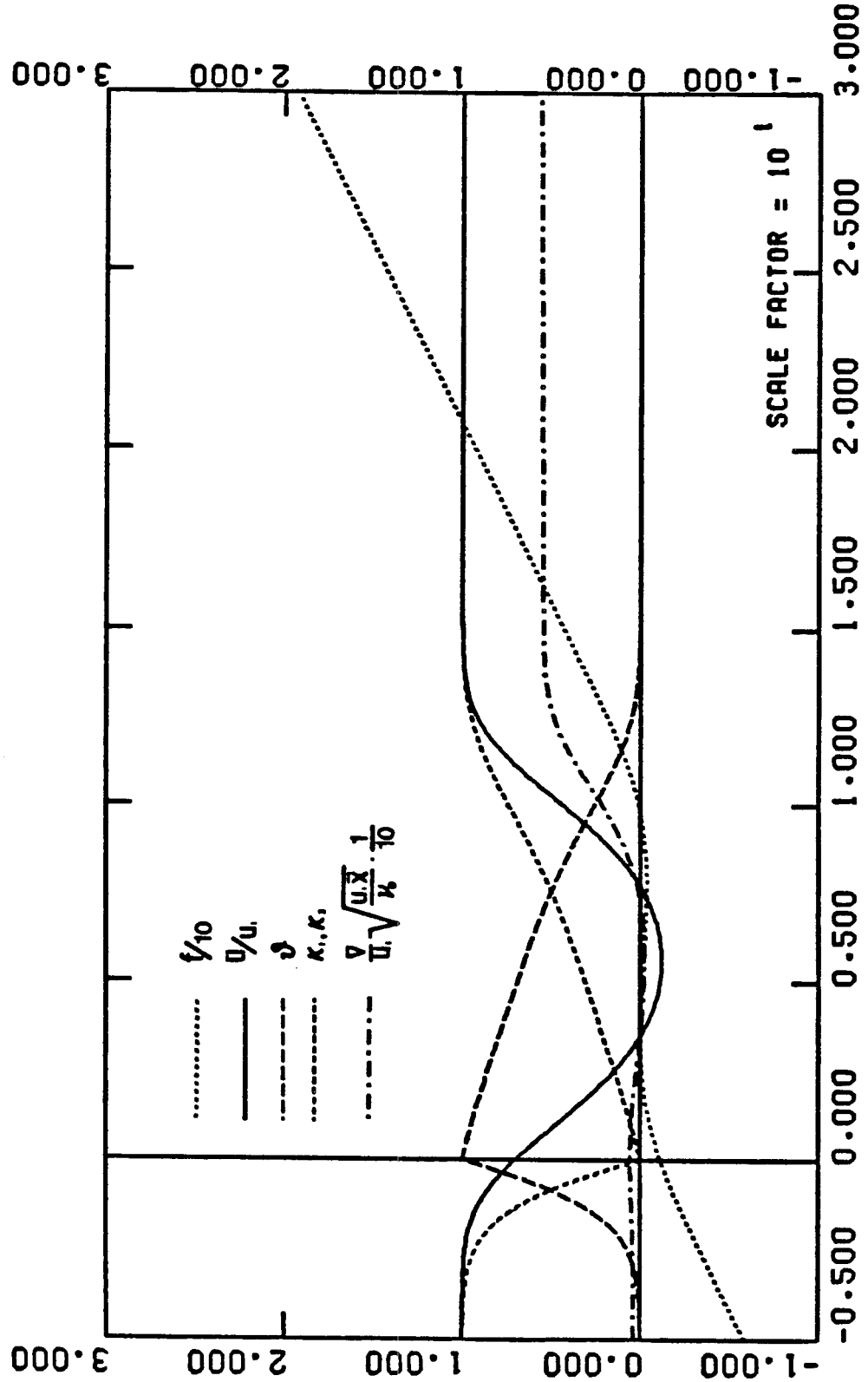

Figure (4.12) Distribution of Properties for a Diffusion Flame with $\varphi = 0.058$, $\beta = -0.0108$ $(K'(0^+) = 0.0418)$.

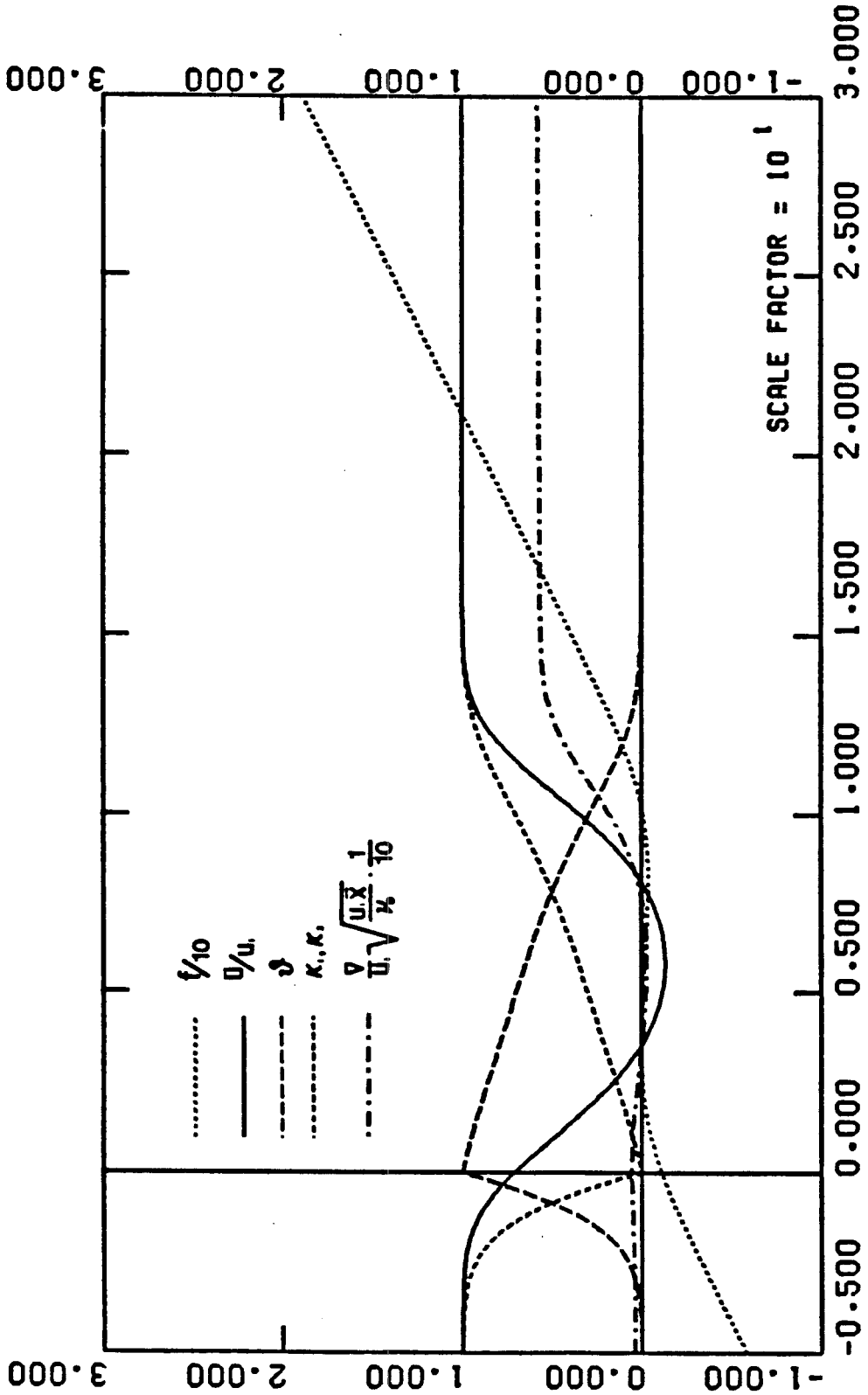

Figure (4.13) Distribution of Properties for a Diffusion Flame with $\varphi = 0.058$, $\beta = -0.010$ $(K'(0^+) = 0.0417)$.

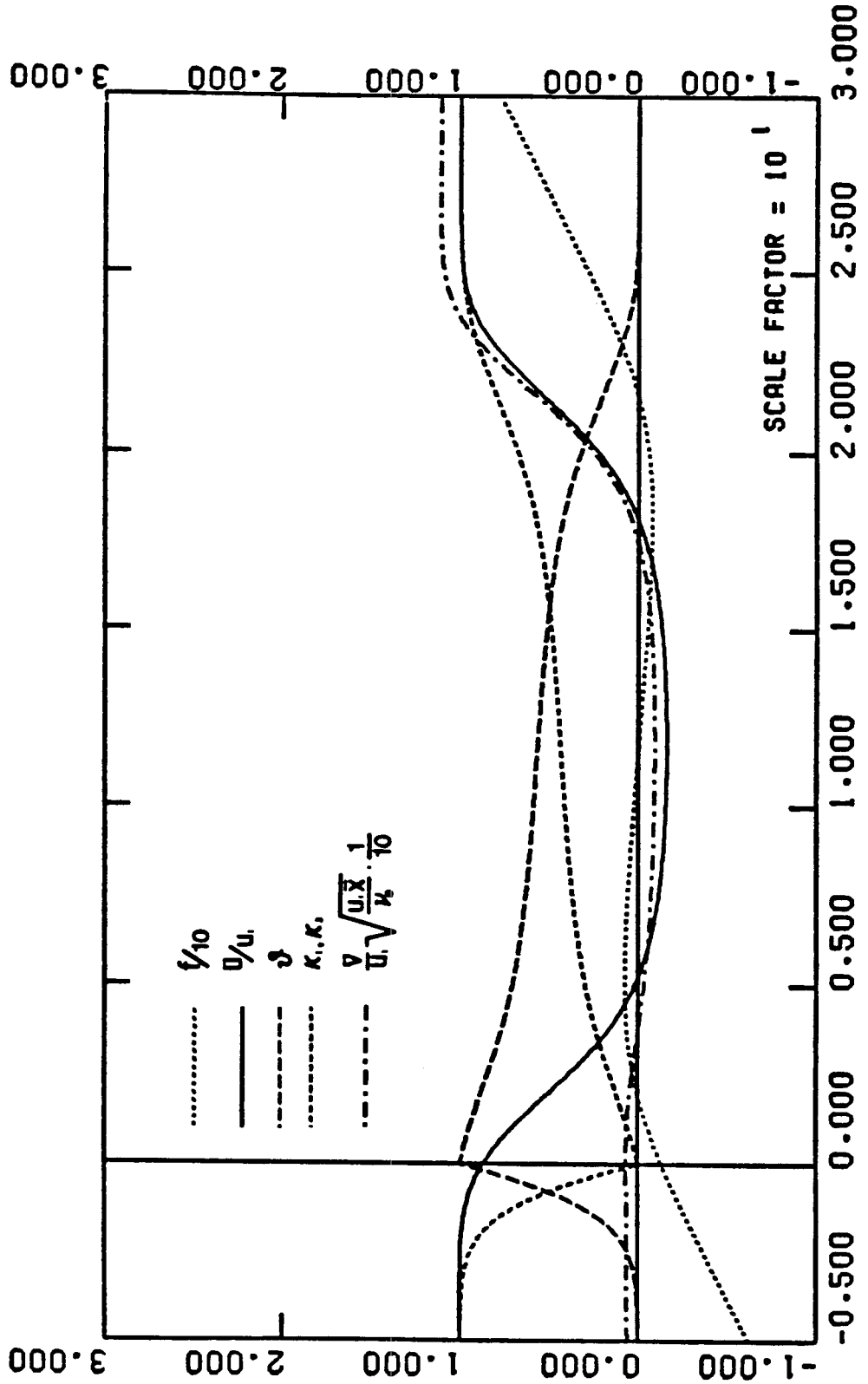

Figure (4.14) Distribution of Properties for a Diffusion Flame with $\varphi = 0.058$, $\beta = -0.001$ $(K'(0^+) = 0.0464)$.

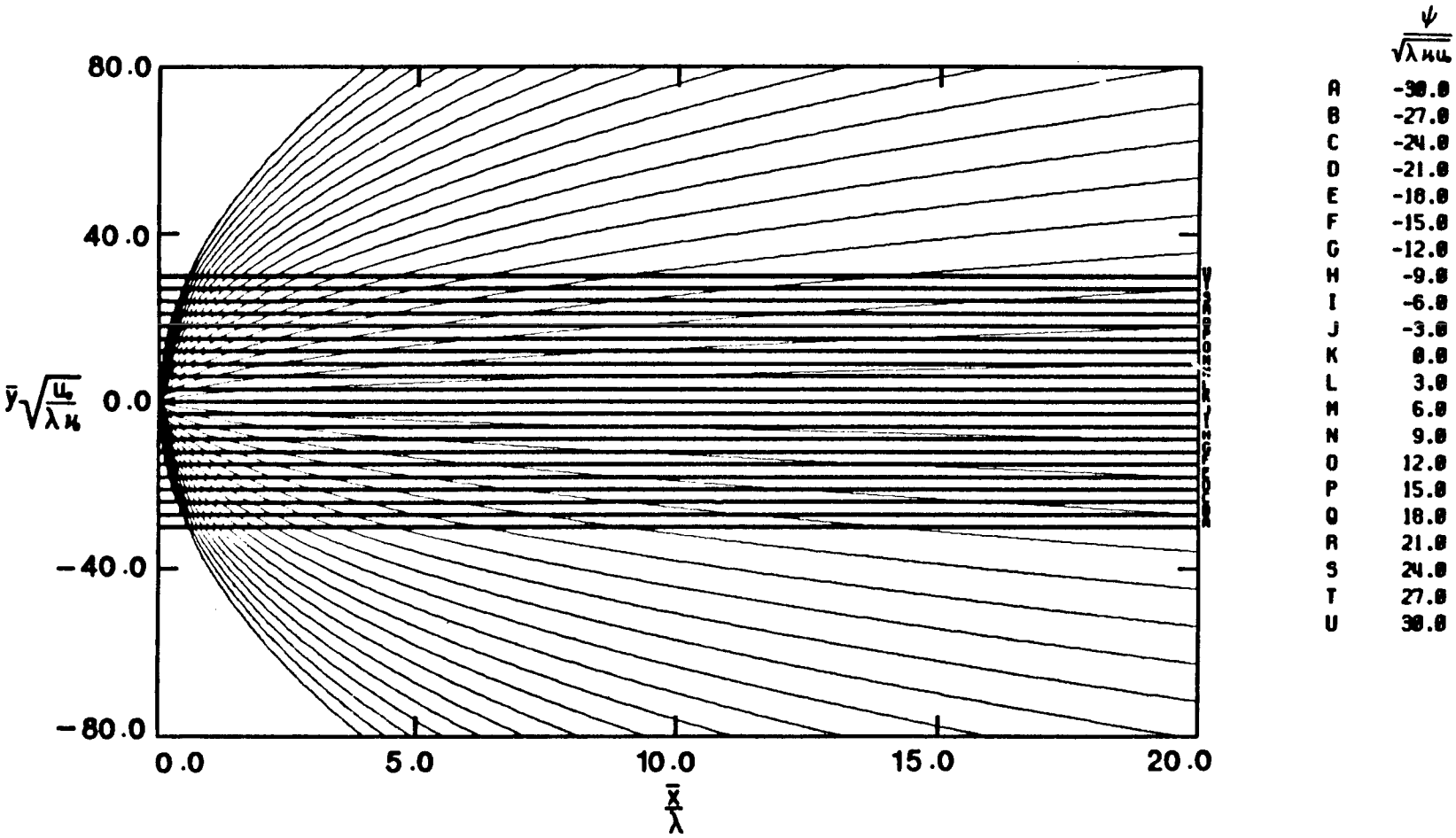

Figure (4.15) Streamline Patterns for a Diffusion Flame with $\varphi = 1.0$, $\beta = 0.0$ $(K'(0^+) = 0.478)$.

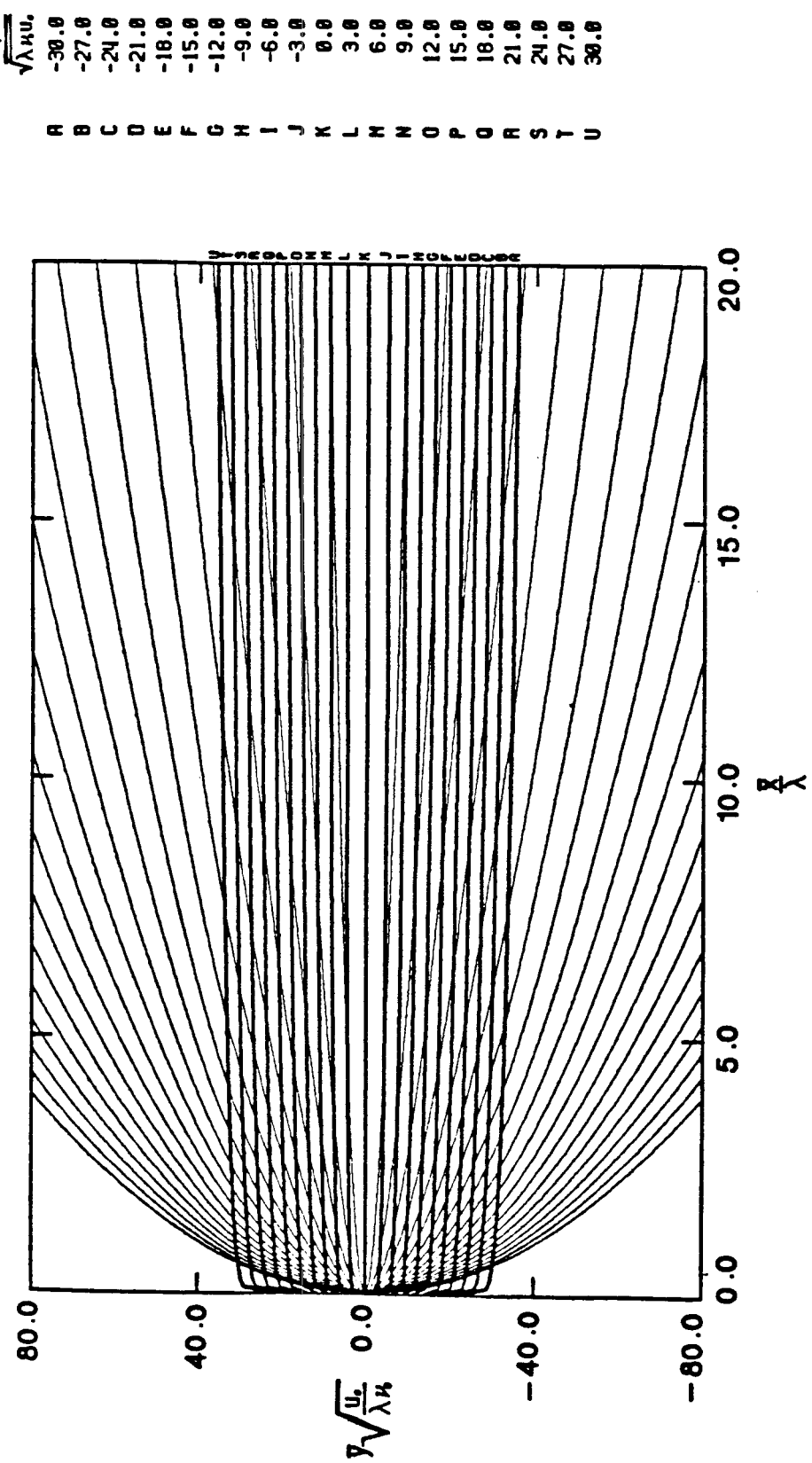

Figure (4.16) Streamline Patterns for a Diffusion Flame with $\varphi = 1.0$, $\beta = -0.0248 \quad (K'(0^+) = 0.400)$.

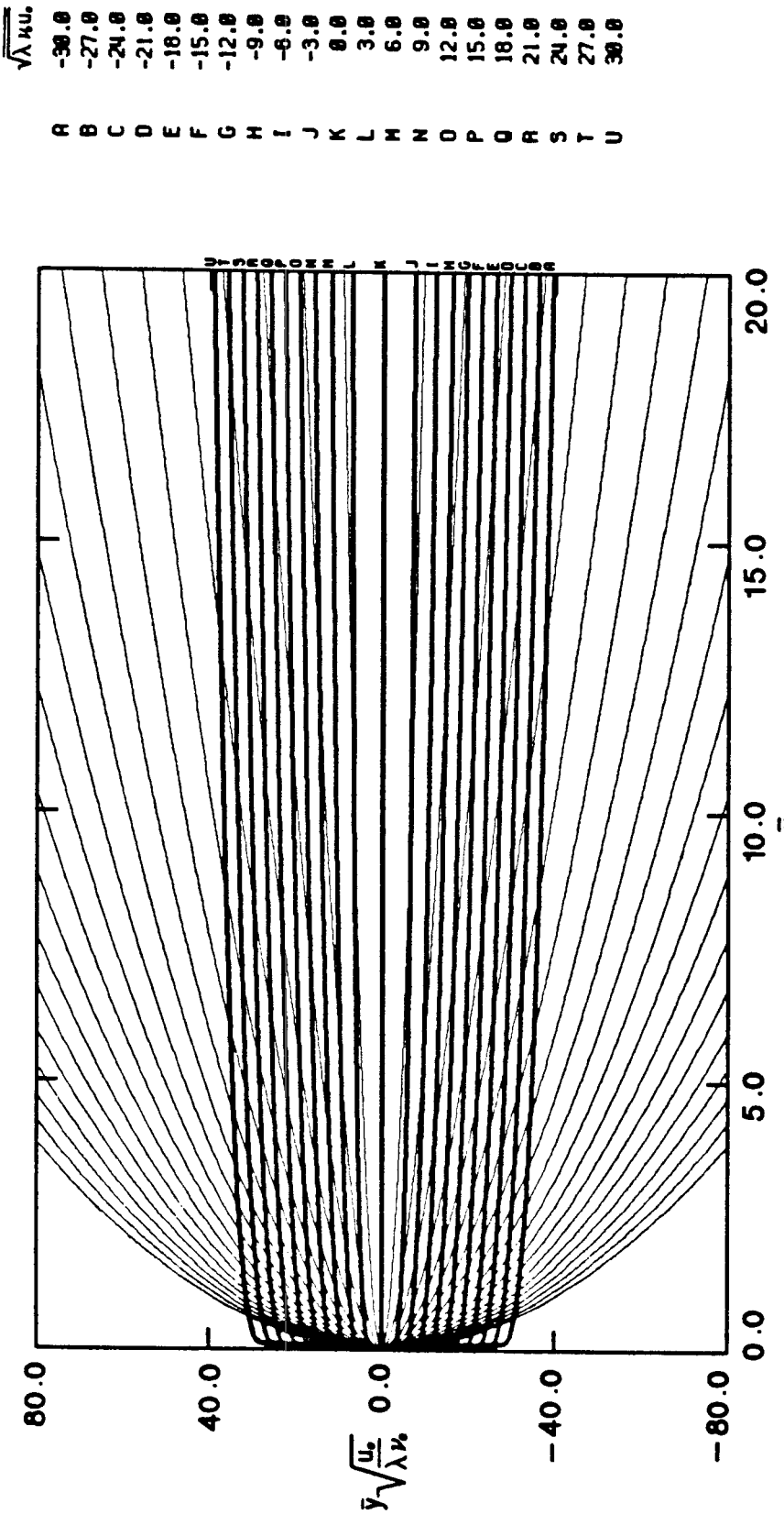

Figure (4.17) Streamline Patterns for a Diffusion Flame with $\varphi = 1.0$, $\beta = -0.0283$ $(K'(0^+) = 0.300)$.

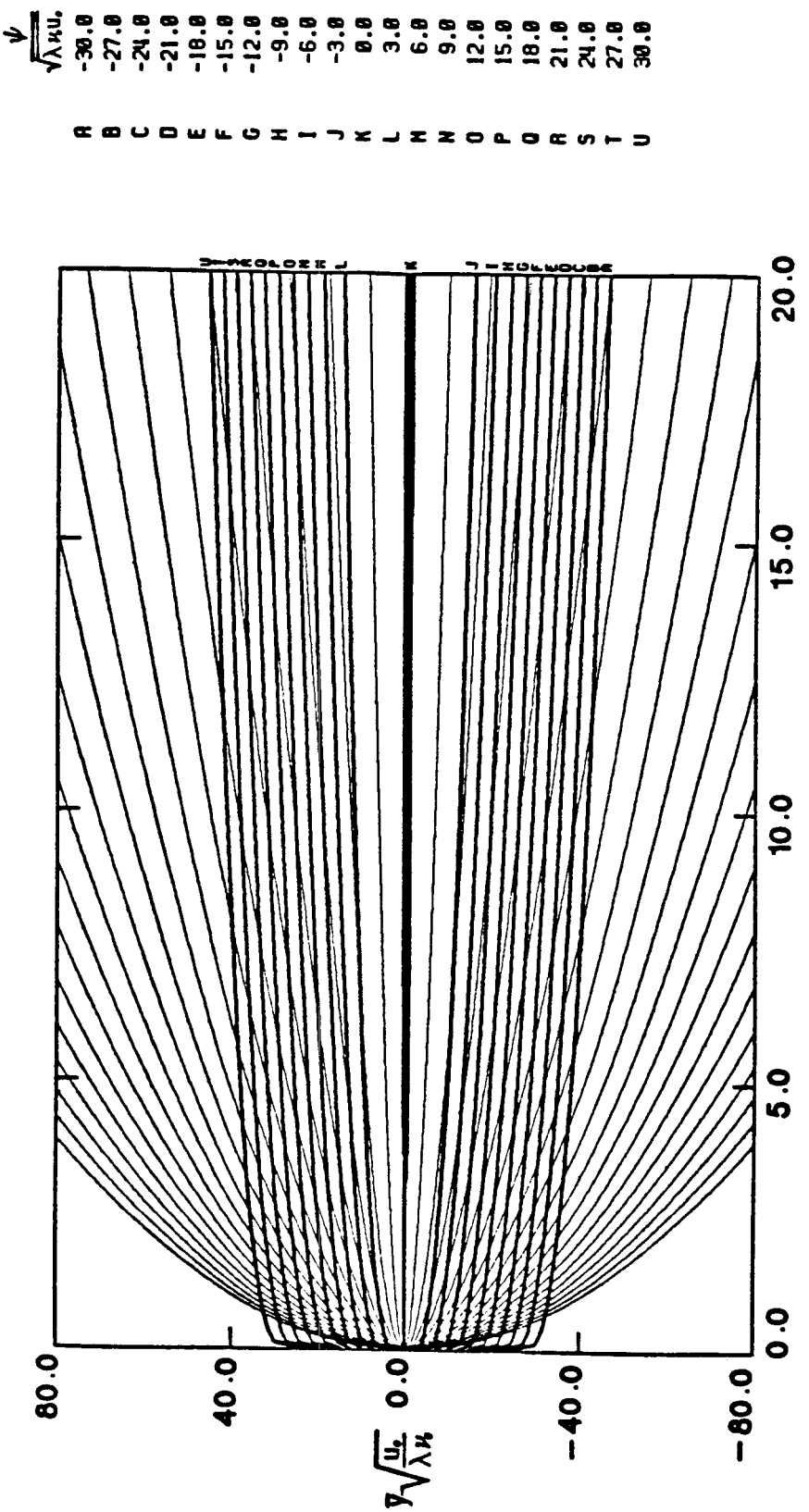

Figure (4.18) Streamline Patterns for a Diffusion Flame with $\varphi = 1.0$, $\beta = -0.0209 \quad (K'(0^+) = 0.220)$.

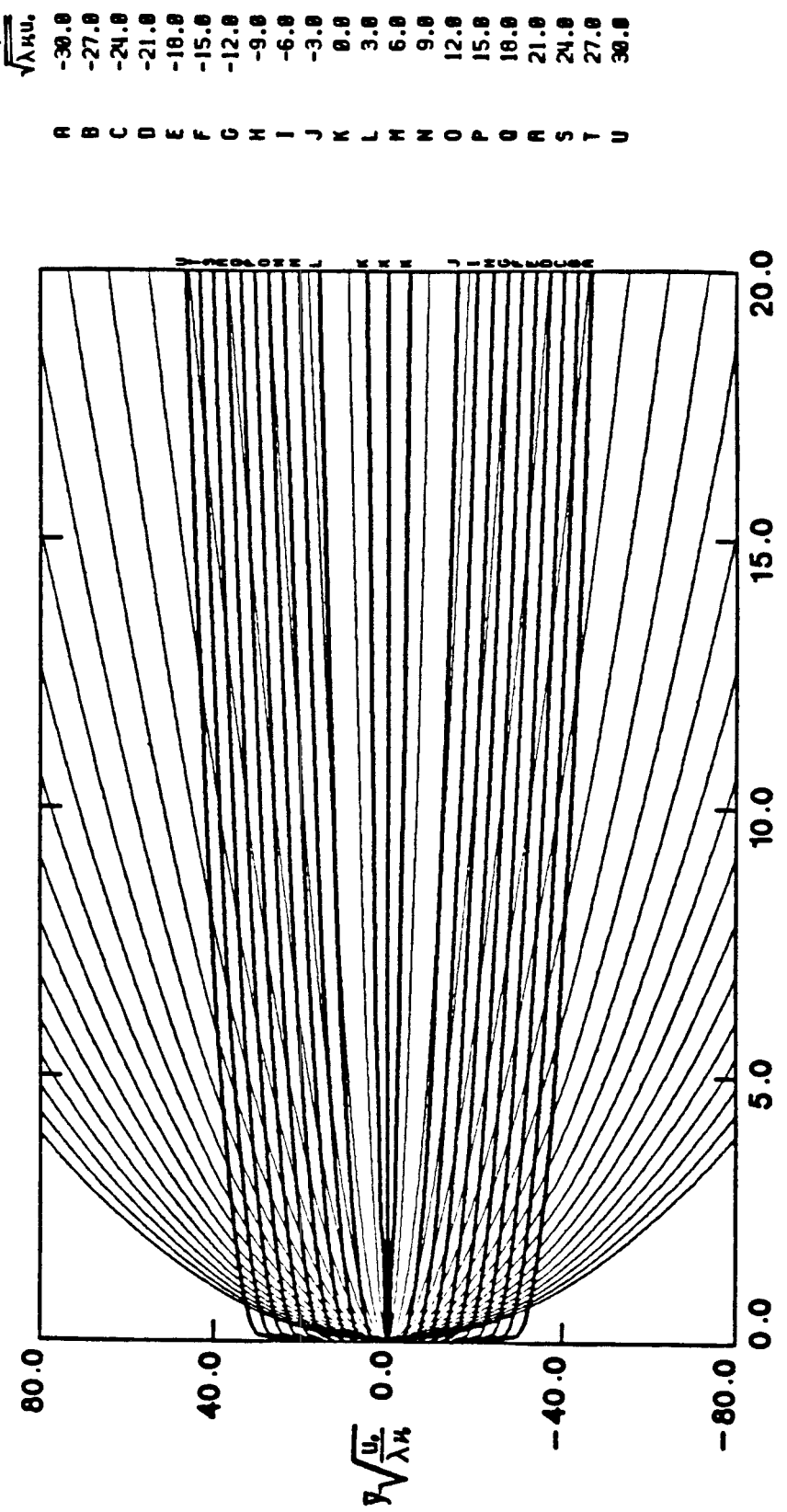

Figure (4.19) Streamline Patterns for a Diffusion Flame with $\varphi = 1.0$, $\beta = -0.0197$ $(K'(0^+) = 0.210)$.

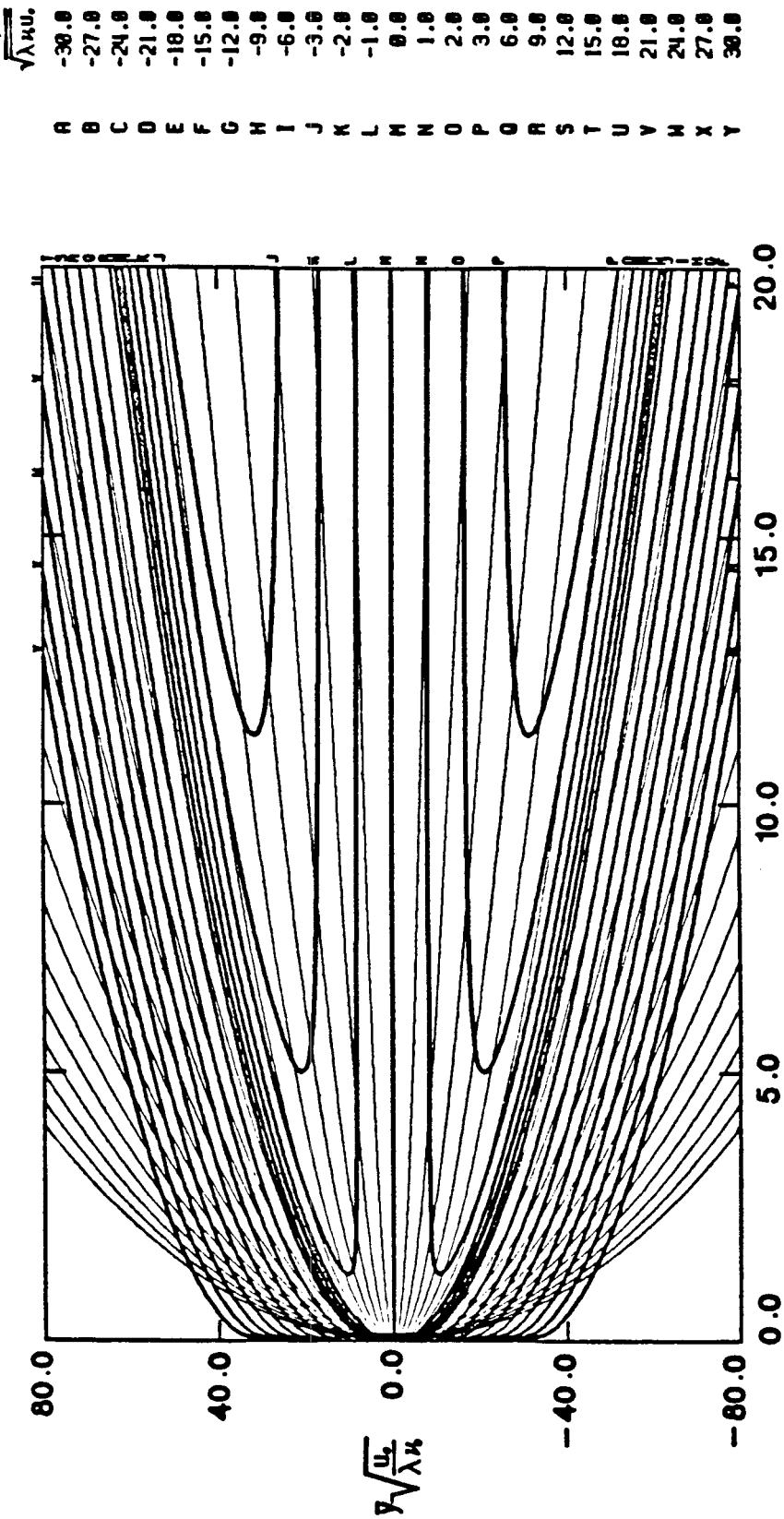

Figure (4.20) Streamline Patterns for a Diffusion Flame with $\varphi = 1.0$, $\beta = -0.00014$ $(K'(0^+) = 0.040)$.

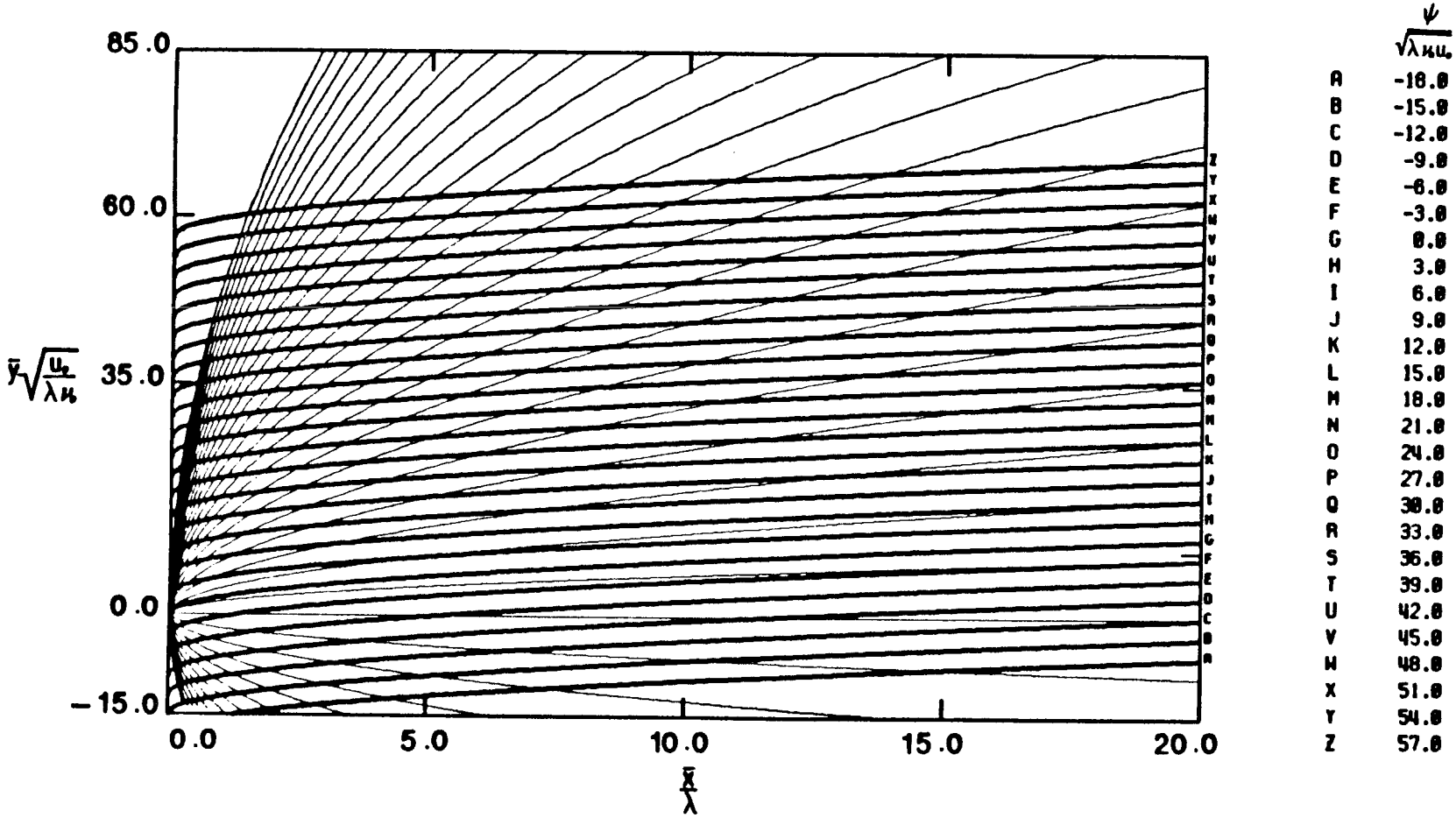

Figure (4.21) Streamline Patterns for a Diffusion Flame with $\varphi = 0.058$, $\beta = 0.0 \quad (K'(0^+) = 0.0705)$.

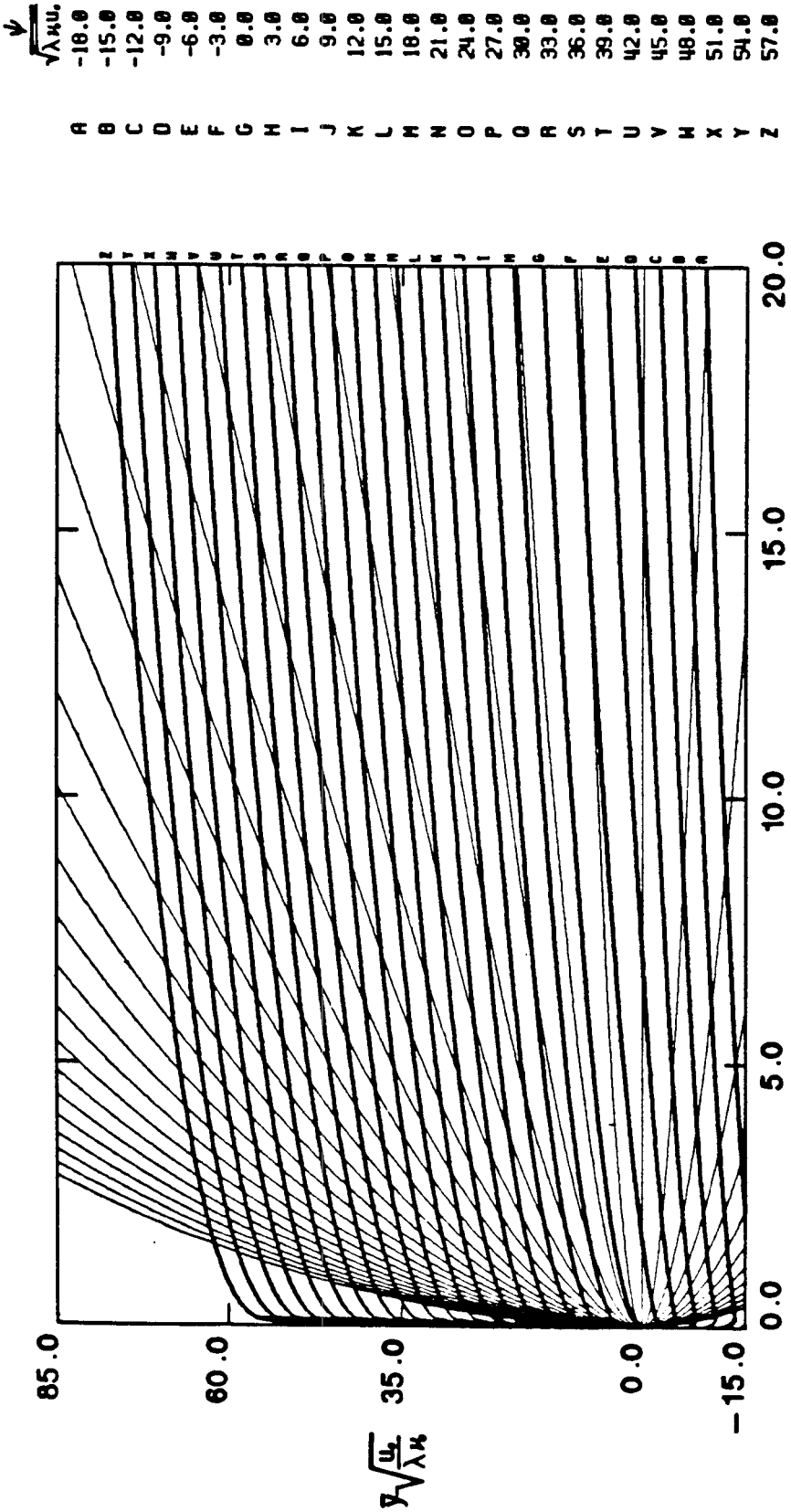

Figure (4.22) Streamline Patterns for a Diffusion Flame with $\varphi = 0.058$, $\beta = -0.020$ $(K'(0^+) = 0.0621)$.

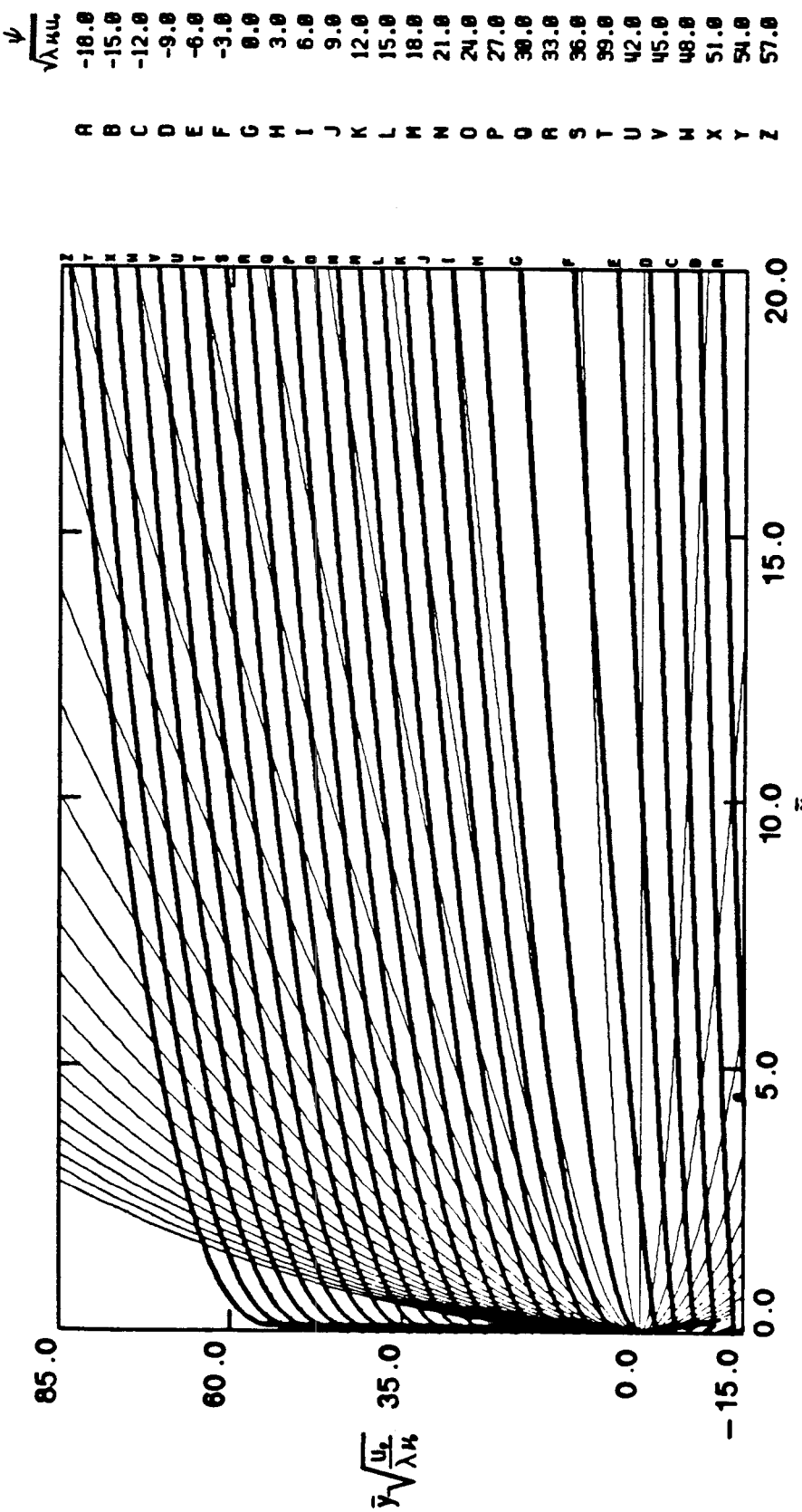

Figure (4.23) Streamline Patterns for a Diffusion Flame with $\varphi = 0.058$, $\beta = -0.025$ $(K'(0^+) = 0.0555)$.

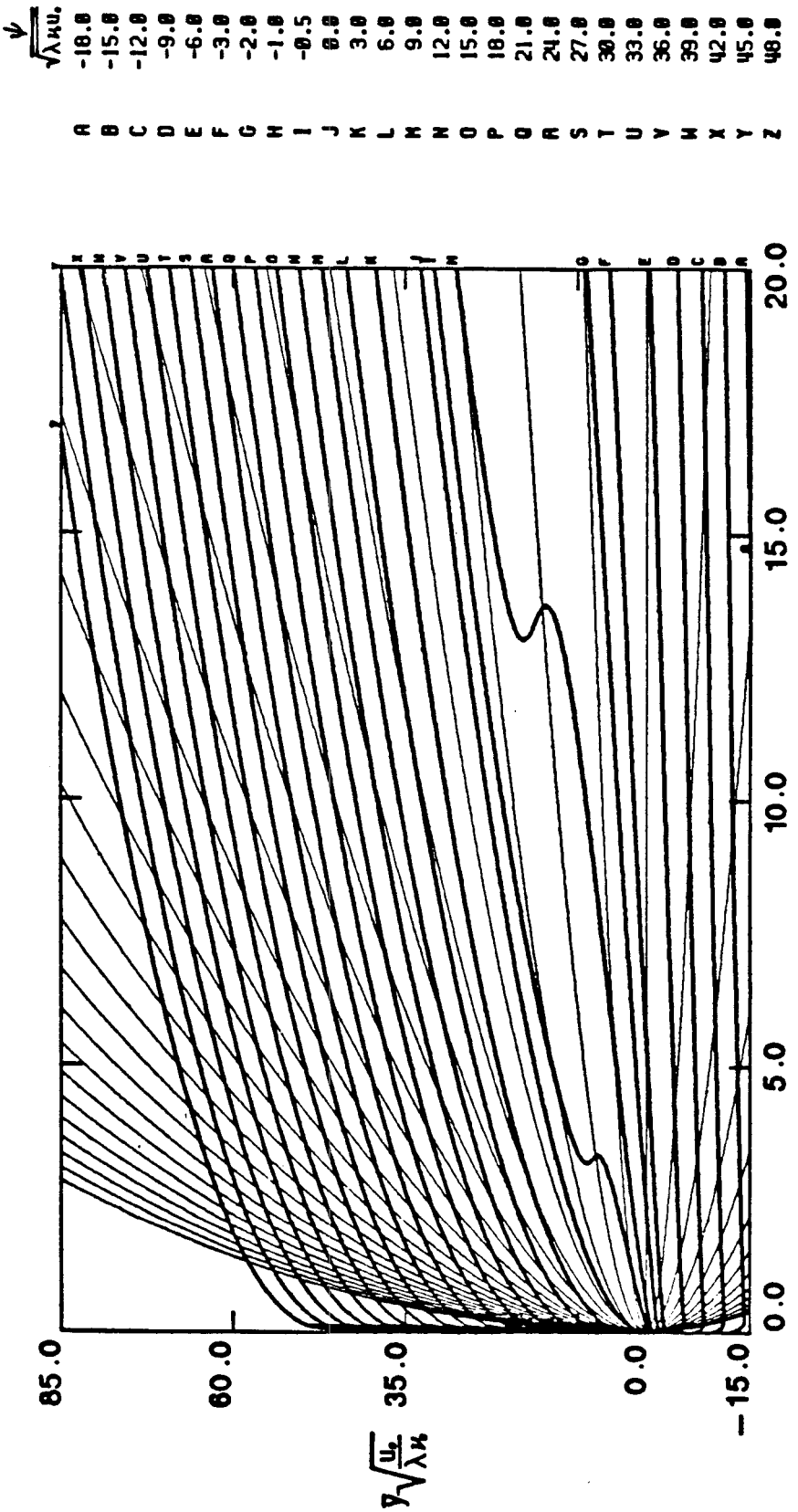

Figure (4.24) Streamline Patterns for a Diffusion Flame with $\varphi = 0.058$, $\beta = -0.017$ $(K'(0^+) = 0.0440)$.

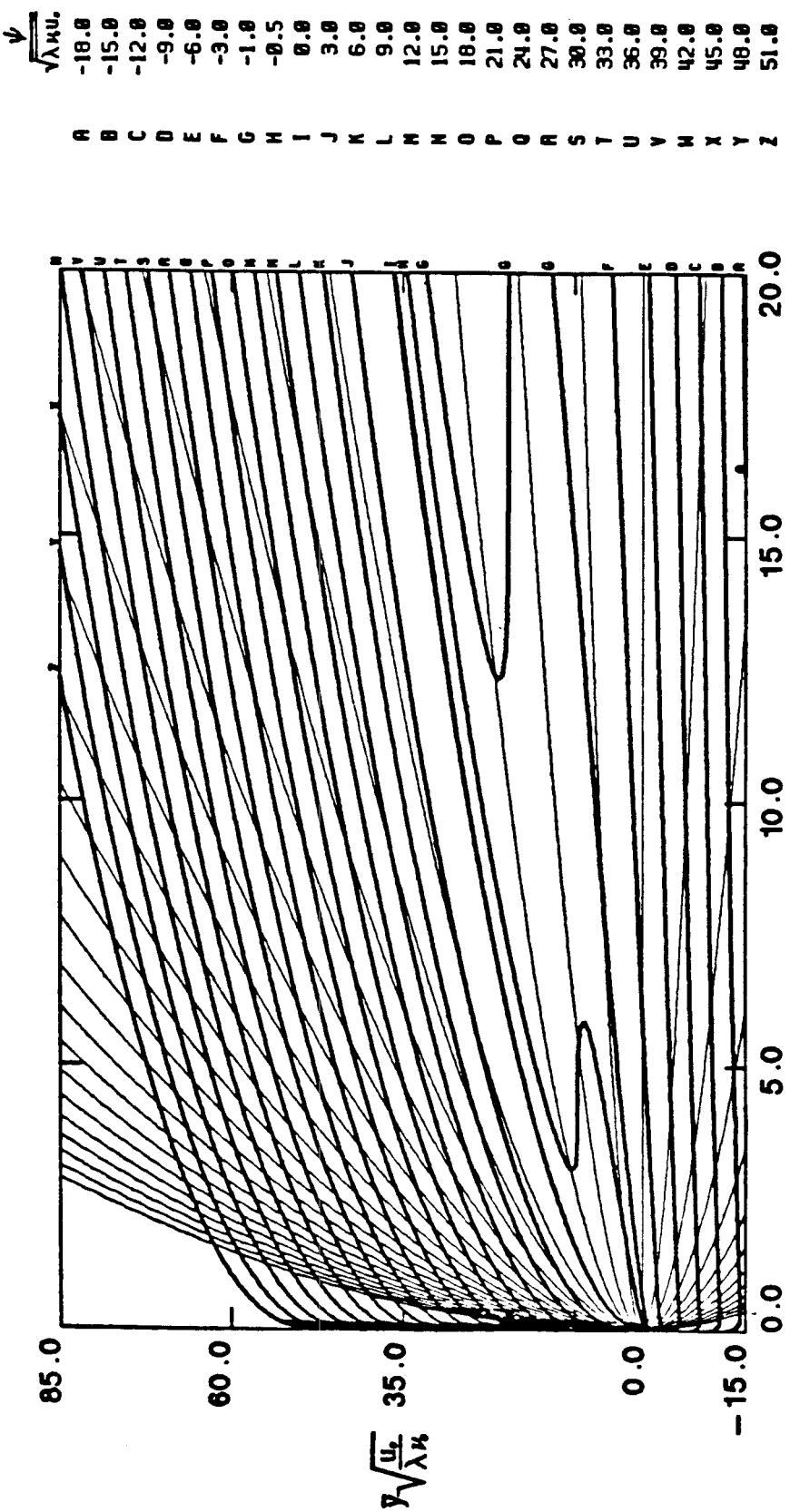

Figure (4.25) Streamline Patterns for a Diffusion Flame with $\varphi = 0.058$, $\beta = -0.015$ $(K'(0^+) = 0.0430)$.

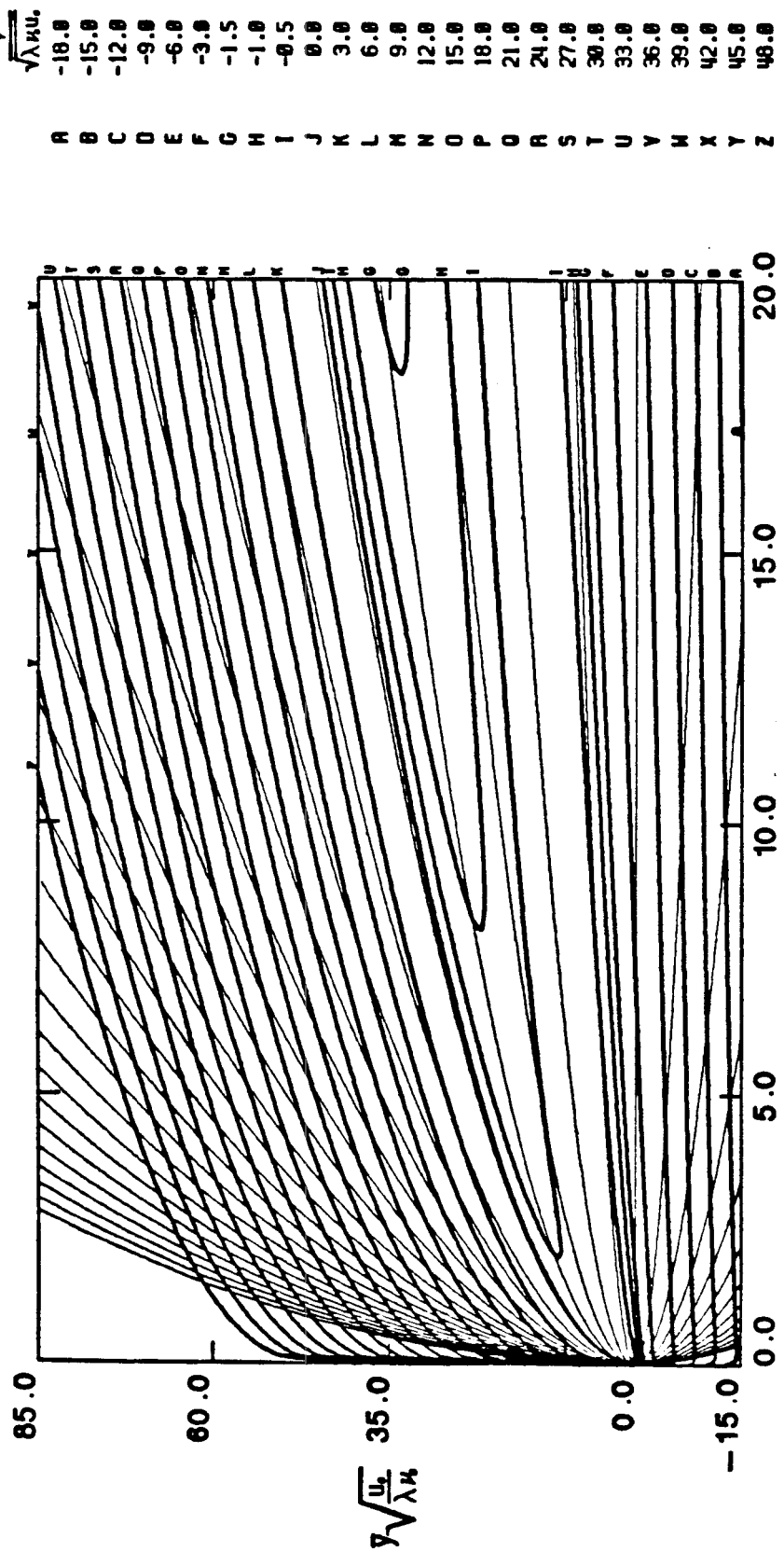

Figure (4.26) Streamline Patterns for a Diffusion Flame with $\varphi = 0.058$, $\beta = -0.0108$ $(K'(0^+) = 0.0418)$.

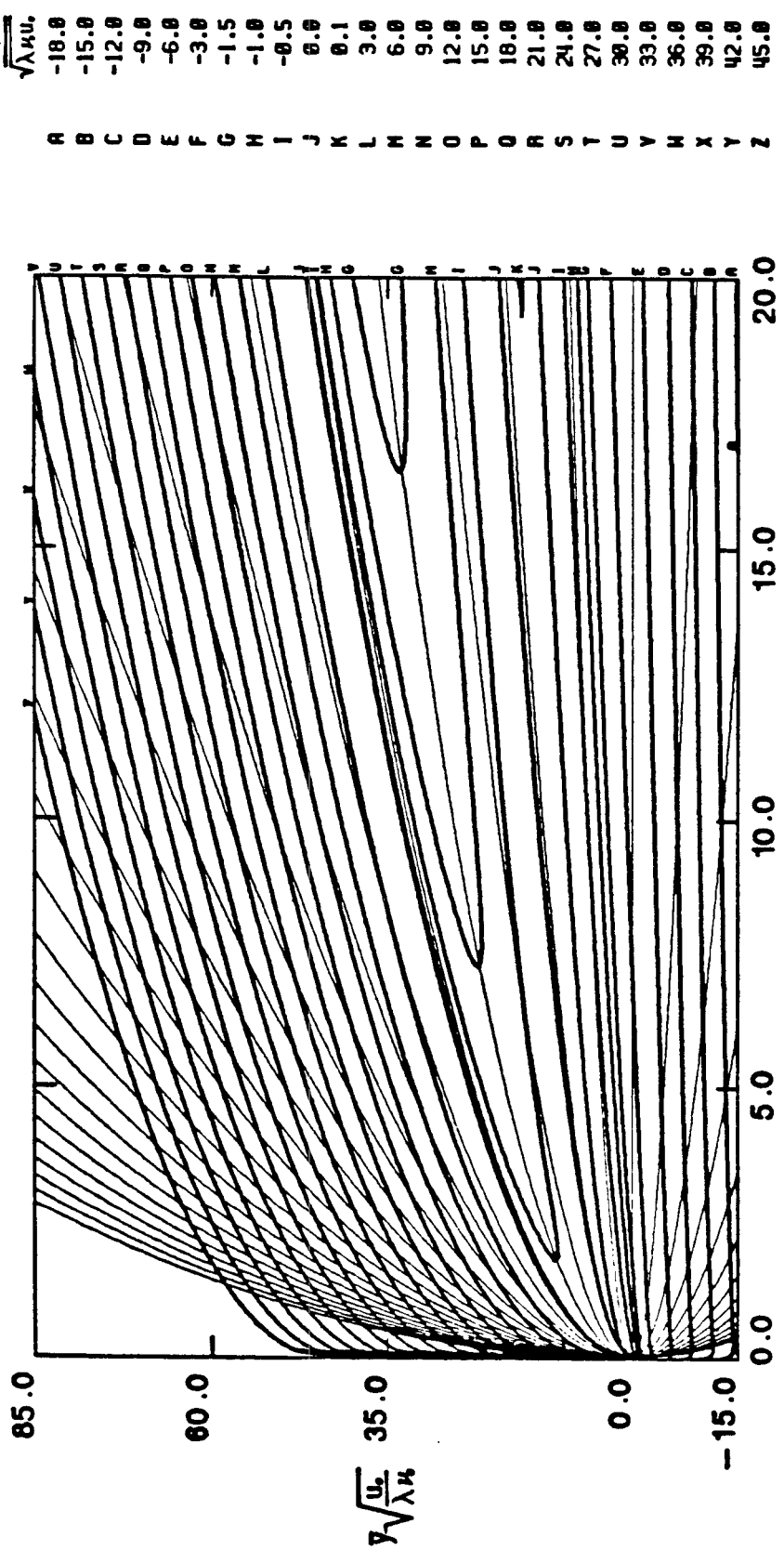

Figure (4.27) Streamline Patterns for a Diffusion Flame with $\varphi = 0.058$, $\beta = -0.0100 \quad (K'(0^+) = 0.0417)$.

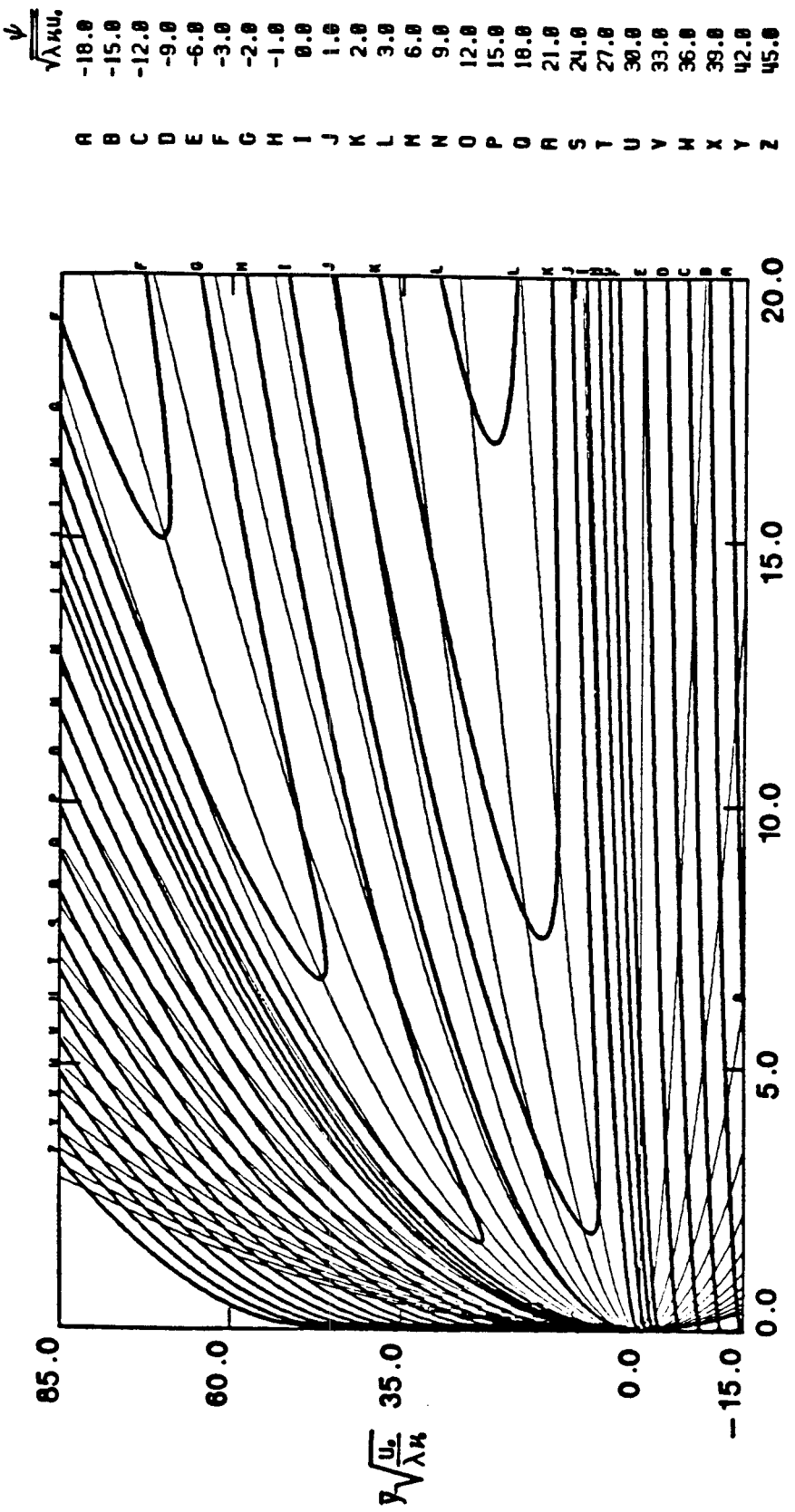

Figure (4.28) Streamline Patterns for a Diffusion Flame with $\varphi = 0.058$, $\beta = -0.001$ $(K'(0^+) = 0.0464)$.

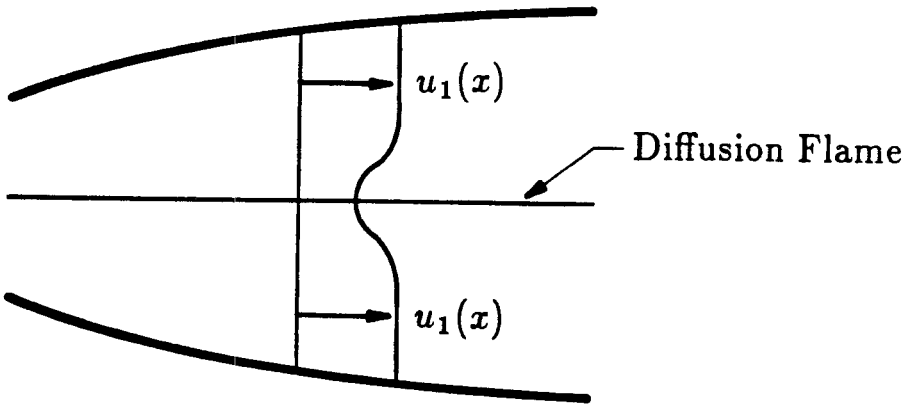

Figure (4.29) (a) Schematic Diagram of a Diffusion Flame in a Diverging Channel.

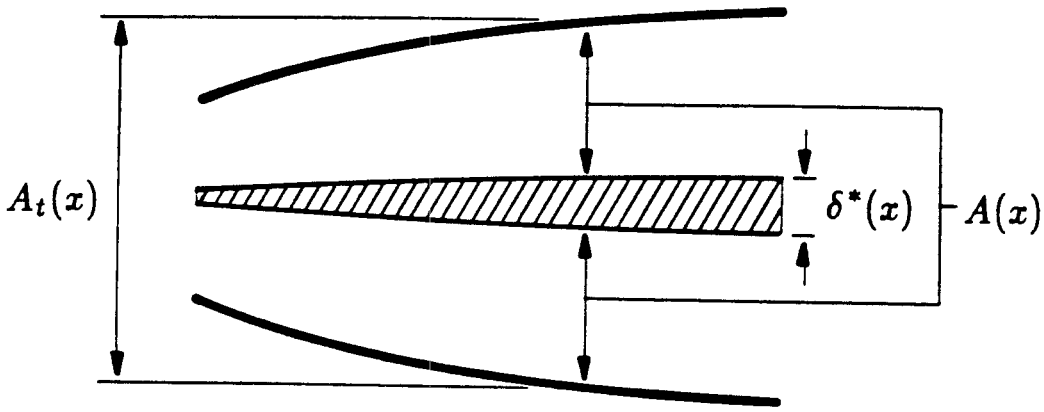

Figure (4.29) (b) Equivalent Channel Area for the Outer Flow Field.

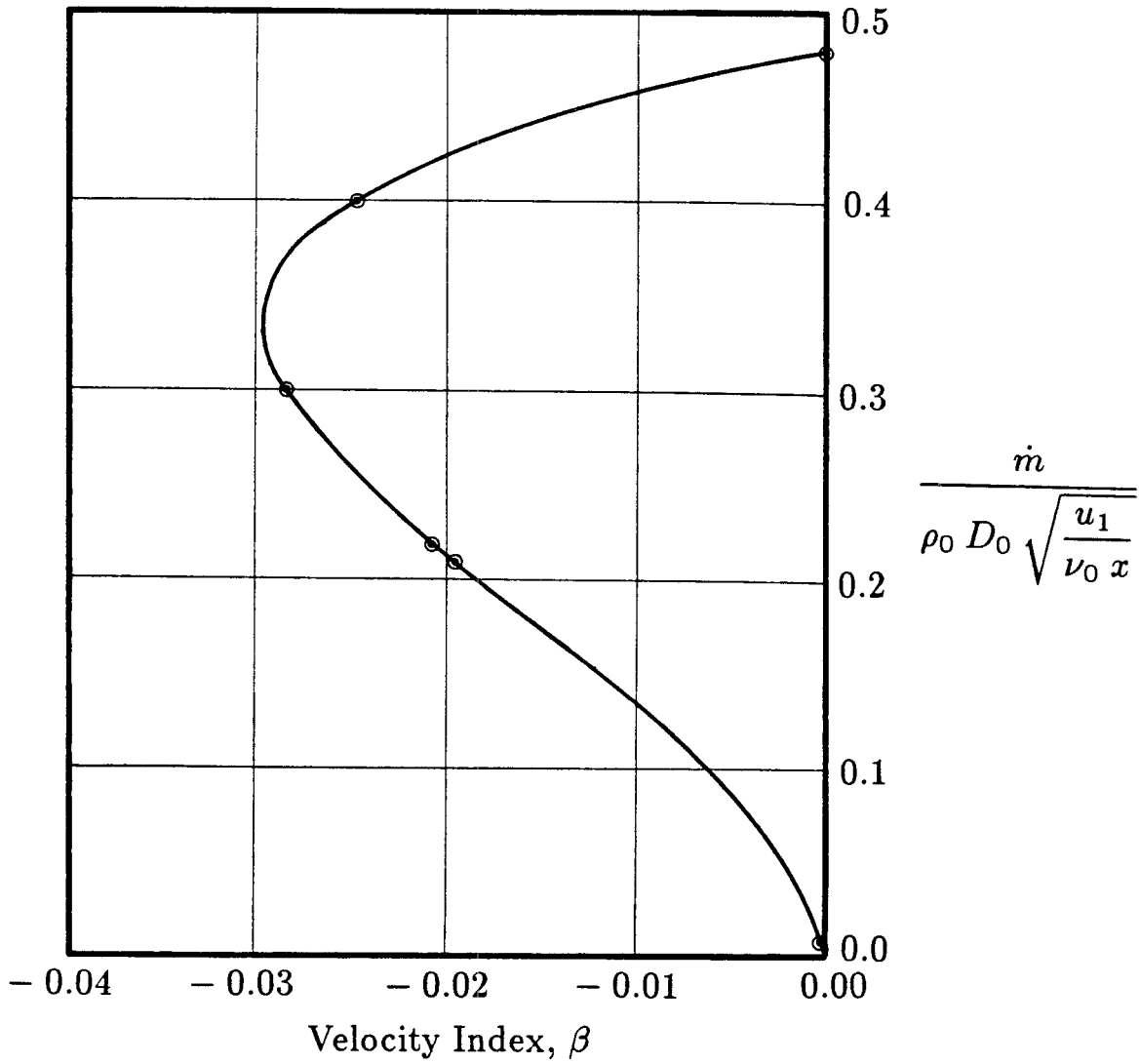

Figure (4.30) Dimensionless Fuel Mass Consumption Rate as a Function of the Velocity Index, β $(\varphi = 1.0)$.

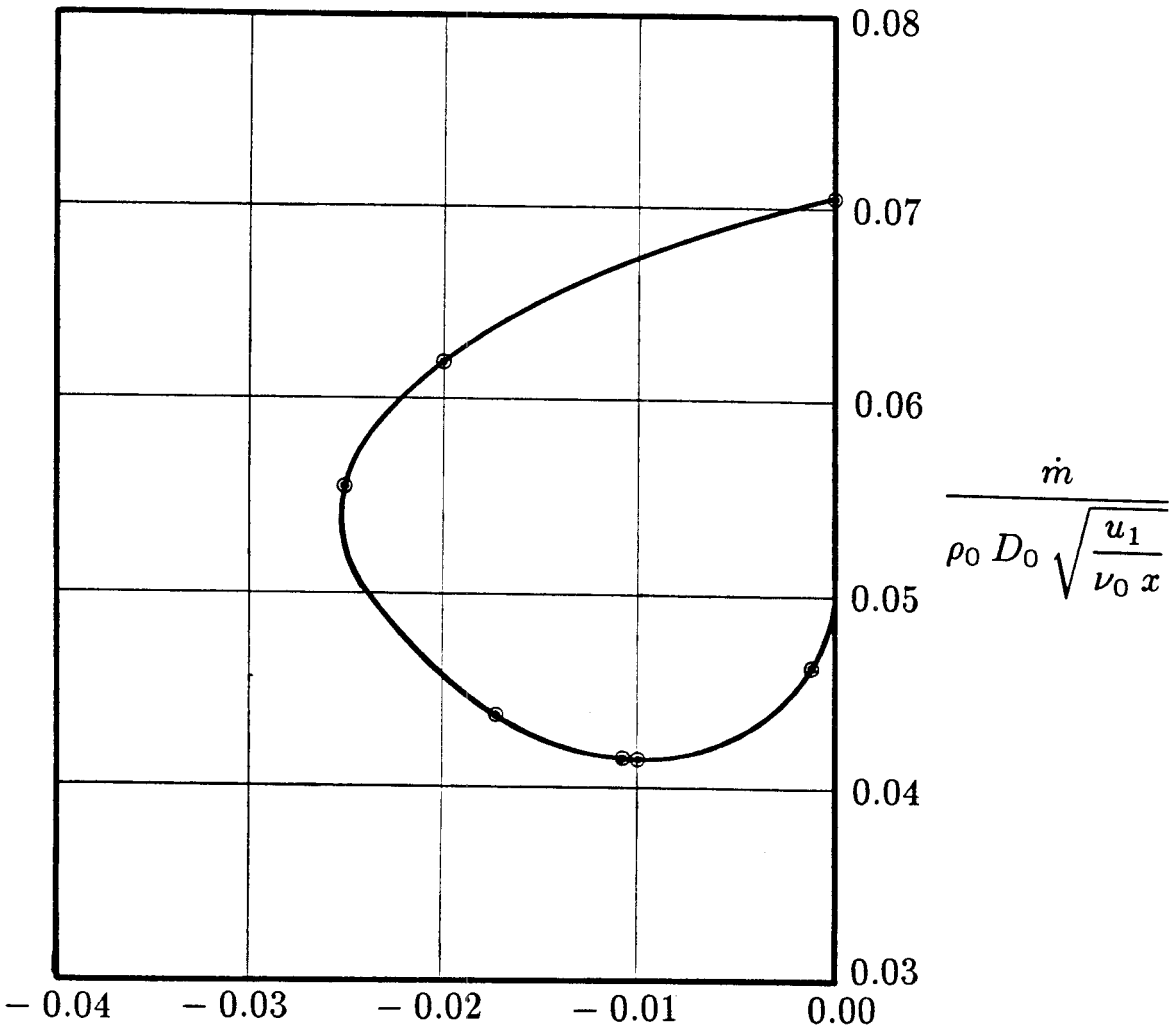

Figure (4.31) Dimensionless Fuel Mass Consumption Rate as a Function of the Velocity Index, β $(\varphi = 0.058)$.

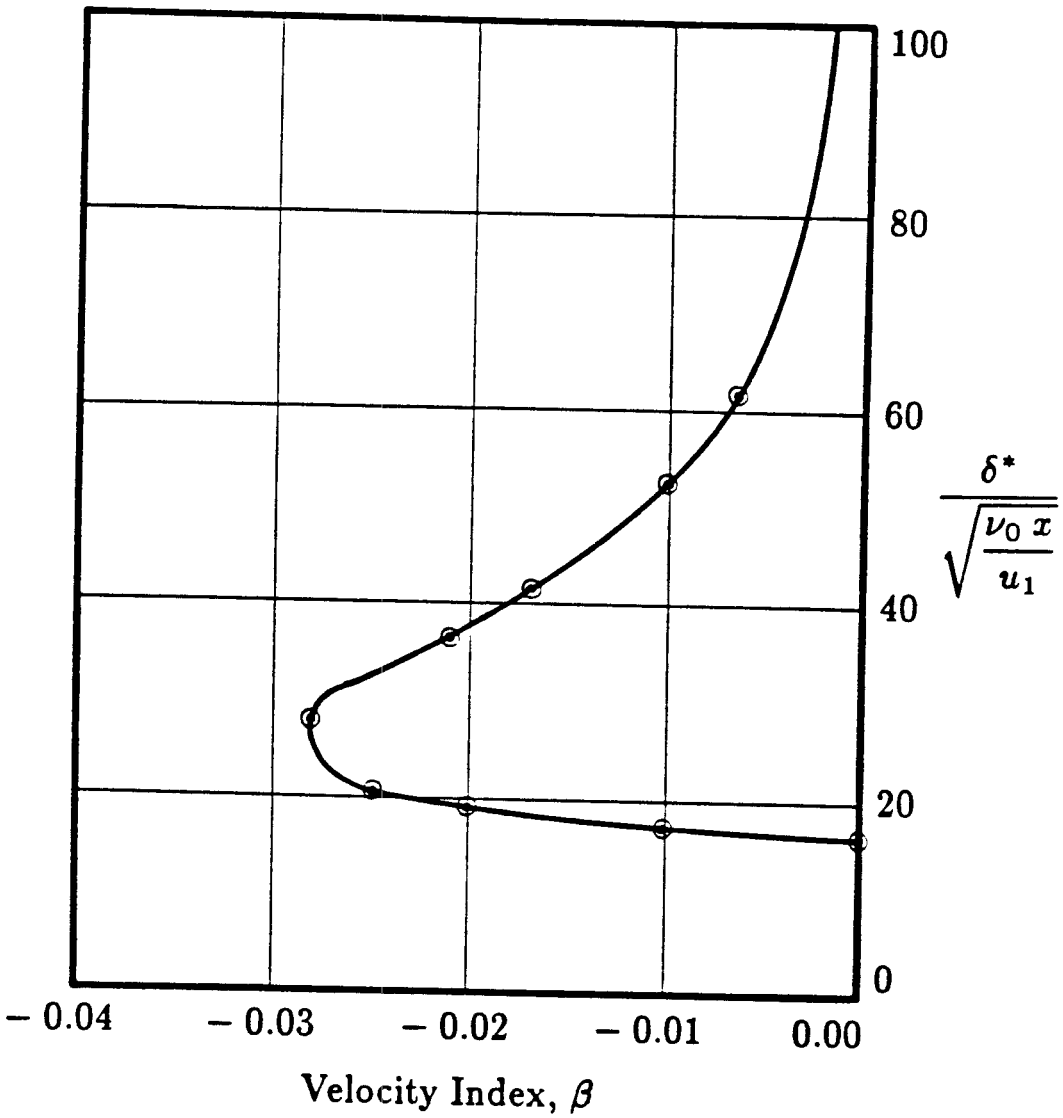

Figure (4.32) Displacement Thickness as a Function of the Velocity Index,β ($\varphi = 1.0$).

Chapter 5

Concluding Remarks

The interaction of the diffusion flame zone with the imposed pressure gradient generates a flow field rich in structure which shows significant changes as the pressure gradient and stoichiometric fuel–air ratios are varied. For favorable pressure gradients the flow field resembles that of the buoyant diffusion flame, the analysis of which produces results reasonably close to those obtained from experiments. Because the present analysis utilizes assumptions similar to those used in the analysis of buoyant diffusion flames, it is expected that the results that have been presented show a corresponding agreement with the physical situations which they model.

The favorable pressure gradient produces a flow field in which fluid accelerates as it moves downstream. The flame is strained along its length and an augmentation in the mass consumption rate of fuel results, the mechanism of which is similar to that of the strained diffusion flame in an unbounded counterflow. Because the fluid mechanics associated with the unbounded counterflow is relatively simple, the structure of the reaction zone and its role in extinction phenomena has been widely studied and is well understood. Because of the close agreement which exists between the results of the present analysis and those of the strained diffusion flame in an unbounded counterflow for infinite reaction rates, the relevance of extinction phenomena to the present problem can be deduced without getting involved in the complex mathematical details that would result from the interaction of the flow field with the chemical reaction. It is deduced that the diffusion flame would show a tendency towards extinction for values of the pressure gradient parameter β greater than one, while the flame associated with values of β less than one would show no such tendency.

The diffusion flame in an adverse pressure gradient has a complex structure which exhibits significant differences for the two fuel–air ratios considered. For both cases the

mass consumption rate is a double valued function of the pressure gradient parameter, but the symmetric flame shows a tendency toward extinction on the lower branch of the solution curve whereas the case corresponding to $\varphi = 0.058$ does not. Two different flow fields are possible for the same value of the pressure gradient parameter β. The suggestion arises that a question of stability is involved in determining which branch of solutions the flow field would tend to for a given pressure gradient. In the case where the pressure gradient is imposed on the flow field by a channel of increasing area, this question does not arise. Two different area programs can produce the same pressure gradient, the nature of the flow field in the vicinity of the flame being different in the two cases. The channel area therefore determines to which branch of solutions the flow field tends. On the other hand, if the flame is embedded in a flow field in which the pressure gradient is imposed on the flame zone by some other fluid mechanic phenomenon (e.g. a diffusion flame embedded in a vortex structure) the branch of solutions to which the flow field would tend is uncertain. It is probably determined by the way in which the flow field evolves in time or, more likely, on the nature of the external flow field producing the pressure gradient.

6. References

Ahmad, T. and Faeth, G.M. (1978), An Investigation of the Laminar Overfire Region along Upright Surfaces, *Journal of Heat Transfer*, **100**, 112

Burke, S. and Schumann, T. (1928), Diffusion Flames, *Industrial and Engineering Chemistry*, **20**, 998

Bush, W.B., Feldman, P.S. and Fendell, F.E. (1976), On Diffusion Flames in Turbulent Shear Flows: Modeling Reactant Consumption in a Mixing Layer, *Combustion Science and Technology*, **13**, 27

Carrier, G.F., Fendell, F.E. and Marble, F.E. (1975), The Effect of Strain Rate on Diffusion Flames, *SIAM Journal of Applied Mathematics*, **28**, 463

Cebeci, T. and Keller, H.B. (1971), Shooting and Parallel Shooting Methods for the Solving the Falkner–Skan Boundary–Layer Equation, *Journal of Computational Physics*, **7**, 289

Cohen, C.B. and Reshotko, E. (1955), Similar Solutions for the Compressible Laminar Boundary Layer with Heat Transfer and Pressure Gradient, *NACA Technical Note 3325*

Falkner, V.M. and Skan, S.W. (1931), Solutions of the Boundary Layer Equations, *Philosophical Magazine*, **12**, 865

Fleming, G.C. (1982), Structure and Stability of Buoyant Diffusion Flames, *Ph.D Thesis, California Institute of Technology*

Groff, E.G. and Faeth, G.M. (1978), Laminar Combustion of Vertical Free–Standing Fuel Surfaces, *Combustion and Flame*, **32**, 139

Hartree, D.R. (1937), On an Equation Occurring in Falkner and Skan's Approximate Treatment of the Equations of the Boundary Layer, *Proceedings of the Cambridge Philosophical Society*, **33**, 223

Howarth, L. (1948), Concerning the Effect of Compressibility on Laminar Boundary Layers and Their Separation, *Proceedings of the Royal Society of London, Series A*, **194**, 16

Karagozian, A.R. (1982), An Analytical Study of Diffusion Flames in Vortex Structures, *Ph.D Thesis, California Institute of Technology*

Kim, J.S., De Ris, J. and Kroesser, F.W. (1971), Laminar Free Convective Burning of Fuel Surfaces, *Thirteenth Symposium (International) on Combustion*, 949

Kinoshita, C.M. and Pagni, P.J. (1980), Laminar Wake Flame Heights, *Journal of Heat Transfer*, **102**, 104

Kosdon, F.J., Williams, F.A. and Buman, C. (1969), Combustion of Vertical Cellulosic Cylinders in Air, *Twelfth Symposium (International) on Combustion*, 253

Liñán, A. (1974), The Asymptotic Structure of Counterflow Diffusion Flames for Large Activation Energies, *Acta Astronautica*, **1**, 1007

Marble, F.E. and Broadwell, J.E. (1977), The Coherent Flame Model for Turbulent Chemical Reactions, *Project SQUID Technical Report TRW-9-PU*

Pagni, P.J. and Shih, T.M. (1977), Excess Pyrolyzate, *Sixteenth Symposium (International) on Combustion*, 1329

Stewartson, K. (1954), Further Solutions of the Falkner Skan Equation, *Proceedings of the Cambridge Philosophical Society*, **50**, 454

Appendix A: The Strained Flame Approximation

A.1 Case 1 $\beta \neq 1$

It was shown in Chapter 3 that the position of a flame element x_e as a function of time is given by the expression

$$\left(\frac{x_e}{\lambda}\right) = \left(\left(\frac{x_0}{\lambda}\right)^{1-\beta} - \frac{(\beta-1)f'(0)u_0 t}{\lambda}\right)^{\frac{1}{1-\beta}} \qquad \beta \neq 1 \tag{a.1}$$

where x_0 is the initial position of the flame element at time $t = 0$. From (a.1) and the strain as a function of position

$$\varepsilon(x) = \frac{du_f}{dx} = \frac{\beta\, f'(0)\, u_0}{\lambda}\left(\frac{x}{\lambda}\right)^{\beta-1} \quad , \tag{a.2}$$

the strain rate as a function of time of a flame element starting off at a position x_0 can be calculated:

$$\varepsilon(t) = \frac{1}{\frac{\lambda}{\beta\, f'(0)\, u_0}\left(\frac{x_0}{\lambda}\right)^{1-\beta} - \frac{\beta-1}{\beta}\, t} \quad . \tag{a.3}$$

A flame element undergoing an arbitrary strain rate $\varepsilon(t)$ has a mass consumption rate

$$\dot{m}_{str}(t) = \rho_0\, D_0 \left(\frac{Sc}{\nu_0\, \pi\, \tau}\right)^{\frac{1}{2}} e^{\int_0^t \varepsilon(t_1)dt_1} \left(\frac{1+\varphi}{2}\right) e^{-\eta_f{}^2} \tag{a.4}$$

where

$$\tau = \int_0^t \left(e^{2\int_0^{t_2} \varepsilon(t_1)dt_1}\right) dt_2 \tag{a.5}$$

and

$$\operatorname{erf} \eta_f = -\left(\frac{1-\varphi}{1+\varphi}\right) \tag{a.6}$$

(see Carrier, Fendell and Marble (1975) or Karagozian (1982)).

The analysis that yields these results has initial conditions

$$K_1(0, y > 0) = 1, \quad K_1(0, y < 0) = 0 \tag{a.7}$$

$$K_2(0, y > 0) = 0, \quad K_2(0, y < 0) = 1 \quad . \tag{a.8}$$

Now in order to draw an analogy between the strained flame and the strained flame element approximation for the flame in a pressure gradient, the two situations have to satisfy the same initial conditions. The flame in the pressure gradient satisfies these conditions at $\frac{x}{\lambda} = 0$ but, since this is a stagnation point in the flow field, we cannot let $\frac{x_0}{\lambda} = 0$ at $t = 0$. In the following calculation it will therefore be assumed that the initial conditions apply at $\frac{x}{\lambda} = \frac{x_0}{\lambda}$, the mass consumption for this case will be calculated and then the limit as $\frac{x_0}{\lambda} \to 0$ will be found as a final step in the calculation.

(a.3) And (a.4) yield

$$\dot{m}_{str}(t) = \rho_0 D_0 \left(\frac{Sc}{\nu_0 \pi}\right)^{\frac{1}{2}} \left(\frac{1+\varphi}{2}\right) e^{-\eta_f{}^2} \left(\frac{\frac{1+\beta}{\lambda} f'(0) \nu_0 \left(\frac{x_0}{\lambda}\right)^{\beta-1}}{h(t) - h(t)^{\frac{-2\beta}{1-\beta}}}\right)^{\frac{1}{2}} \tag{a.9}$$

where

$$h(t) = \left(1 - \frac{\beta - 1}{\lambda} f'(0) u_0 \left(\frac{x_0}{\lambda}\right)^{\beta-1} t\right) \tag{a.10}$$

or, converting back to the spatial variable

$$\dot{m}_{str}(x) = \rho_0 D_0 \left(\frac{Sc}{\nu_0 \pi}\right)^{\frac{1}{2}} \left(\frac{1+\varphi}{2}\right) e^{-\eta_f{}^2} \left(\frac{(1+\beta)\ f'(0)\, u_1}{x}\right)^{\frac{1}{2}} \frac{1}{\left(1 - \left(\frac{x_0}{x}\right)^{\beta+1}\right)^{\frac{1}{2}}} \tag{a.11}$$

and

$$\lim_{x \to 0} \dot{m}_{str}(x) = \rho D_0 \left(\frac{u_1}{\nu_0 x}\right)^{\frac{1}{2}} \left(\frac{(1+\beta)\ f'(0)\, Sc}{\pi}\right)^{\frac{1}{2}} \left(\frac{1+\varphi}{2}\right) e^{-\eta_f{}^2} \tag{a.12}$$

A.2 Case 2: $\beta = 1$

For $\beta = 1$ the strain rate is constant and given by the expression

$$\varepsilon_0 = \frac{f'(0)\, u_0}{\lambda} = \frac{f'(0)\, u_1}{x} \tag{a.13}$$

and the steady state mass consumption rate for a flame subject to a constant strain rate is

$$\begin{aligned} \dot{m}_{str} &= \rho_0 D_0 \left(\frac{2\,\varepsilon_0\, Sc}{\pi\, \nu_0}\right)^{\frac{1}{2}} \left(\frac{1+\varphi}{2}\right) e^{-\eta_f{}^2} \\ &= \rho_0 D_0 \left(\frac{u_1}{\nu_0 x}\right)^{\frac{1}{2}} \left(\frac{2\, f'(0)\, Sc}{\pi}\right)^{\frac{1}{2}} \left(\frac{1+\varphi}{2}\right) e^{-\eta_f{}^2} \end{aligned} \tag{a.14}$$

which is the same as (a.11) for $\beta = 1$. The expression

$$\dot{m}_{str}(x) = \rho_0 D_0 \left(\frac{u_1}{\nu_0\, x}\right)^{\frac{1}{2}} \left(\frac{(1+\beta)\, f'(0)\, Sc}{\pi}\right)^{\frac{1}{2}} \left(\frac{1+\varphi}{2}\right) \mathrm{e}^{-\eta_f{}^2} \qquad \text{(a.15)}$$

is therefore uniformly valid for all $\beta > 0$.

Part 2

A Computational Model for Combustion Instabilities Behind a Rearward Facing Step Flameholder.

Chapter 1

Introduction

Combustion instabilities generated in the combustion chambers of air breathing engines can be divided into two classes according to their origin. The first class comprises of the instabilities generated by the interaction of the combustion zone behind the flame holding device with pressure and velocity fluctuations corresponding to transverse modes of the combustion chamber. This mode of combustion instability is generally of high frequency (because of the compact transverse dimensions of combustion chambers) and is referred to as screeching combustion. Rogers and Marble (1956) conducted an experimental investigation into the mechanism of screeching combustion. They found that the transverse oscillations in the combustion chamber caused vortices to be shed alternately from the flameholder edges. The unsteady combustion in these vortices, in turn, reinforced the pressure oscillations, making the instability mechanism self sustaining. Because of the relative ease with which transverse pressure oscillations can be damped out, screeching combustion does not constitute a problem in combustion chambers of modern air breathing engines.

The second class of combustion instability comprises of those excited by the pressure oscillations corresponding to longitudinal modes of the combustion system. In ramjet engines these longitudinal pressure oscillations can interact with the shock structure at the inlet to such an extent that the shock moves out of the inlet, in effect causing a failure of the propulsion system. The excitation of the longitudinal modes of oscillation involves a complex interaction between the pressure waves, the flame holding device, and the combustion zone behind this device which, at present, is not well understood. Numerous experimental studies have been conducted in an effort to gain some insight into the interaction mechanism. Gangi and Sawyer (1980) conducted an experimental investigation on the effect of fuel–air equivalence ratio on pollutant formation for lean

mixtures. For low equivalence ratios the combustion zone downstream of their rearward facing step flameholder resembled the mixing zone of non–reacting fluids which is characterized by the presence of coherent vortical structures. As the equivalence ratio of the fuel–air mixture was increased toward stoichiometric, the nature of the combustion zone downstream of the step changed dramatically. Instead of a mixing layer forming downstream of the step, large scale vortical structures (much larger than those present in the mixing layer) were periodically shed from the edge of the flame holder. Keller (1982) and Vaneveld (1984) studied the unstable mode of combustion in more detail but little insight into the fundamental mechanism of formation of the large vortical structures was gained from these studies.

Smith and Zukoski (1985) followed up on these studies with an experimental investigation of the unstable combustion mode in a combustion facility similar to the one used by the previous workers in the field. They made the important discovery that the frequencies at which at which the large vortical structures were shed from the flameholder corresponded to longitudinal acoustic modes of the system. It was found that the velocity fluctuations associated with the longitudinal pressure oscillations were of the same order of magnitude as the mean flow of the reactants, causing a surging flow over the step which, they proposed, could account for the shedding of the large vortical structures.

The experimental apparatus used by Smith and Zukoski is shown schematically in fig(1.1). A flow control system delivers a premixed methane–air mixture in any equivalence ratio over a wide variety of flow rates. The flow control system delivers the combustible mixture to a cylindrical plenum chamber where the flow is straightened by a porous core section and a series of mesh screens. The mixture then flows through a contraction section which changes the axisymmetric flow field in the plenum chamber to a two dimensional field compatible with the combustion chamber. The combustible

mixture flows from the contraction section into an inlet section which feeds the reactants into the combustion chamber over a rearward facing step flameholder.

A linearized, one dimensional acoustic analysis was done to determine the resonant frequencies of oscillation corresponding to longitudinal modes of the combustion system. The system displayed several resonant modes, each corresponding to the resonant mode of oscillation of a different component, or a combination of components, of the system. Even though the pressure fluctuations encountered in the experiment were large (between 1% and 10% of ambient), which would imply that nonlinear effects would be important, the linearized model produced results that compared well with the resonant frequencies deduced from the experimental study. This, however, is expected since nonlinear effects cause small changes in the resonant frequencies of a system away from those produced by a linear analysis.

A feature of the apparatus was that the resonant frequencies of the system could be varied by changing the length of the plenum chamber. Experiments were conducted for various fuel–air equivalence ratios and three different configurations. In all cases it was found that when the unstable mode of combustion was excited, the large vortical structures were shed at frequencies associated with the resonant modes of the system.

Fig(1.2) shows the structure of the flow field when the large vortical structures are shed at 188 Hz, this frequency corresponding to the resonant mode of oscillation of the plenum chamber. The value of the pressure perturbation at the edge of the flameholder is shown alongside the sequence of shadowgraphs. In the first frame of the shadowgraph sequence the fluid above the step is nearly stagnant, indicating that the magnitude of the velocity fluctuation is close to the mean fluid velocity. As the pressure at the edge of the step falls, the fluid above the step is exposed to a pressure gradient which causes it to surge forward, forcing a jet of the cold unreacted mixture into the combustion chamber which is filled with hot combustion products. As the jet of reactants moves into the

chamber, the vortex sheet formed at the boundary between the hot and cold fluid rolls up into a large vortex, causing the bulk of the cold mixture above it to move downward toward the lower wall. This continues until the downward moving tongue of reactants formed by the vortex impinges against the lower wall, causing the reactants to spread, mix with the hot combustion products, and react vigorously. The intense combustion which results is thought to have a major effect on the driving of the pressure oscillations and therefore the sustenace of the unstable combustion phenomenon. By changing the equivalence ratio of the fuel–air mixture and its mass flow rate into the combustion chamber, large vortex shedding at other resonant modes of the system was excited.

The experimental study also indicated that once a stable mode of vortex shedding was excited, changes in the velocity of the mean flow did not cause significant changes in the structure of the flow field. This was true up to a certain critical mean flow velocity at which another frequency of vortex shedding was excited intermittently. Increasing the fluid velocity above this critical value would change the frequency of vortex shedding.

In the present study a first attempt is made to investigate, computationally, the behavior of a surging flow of a high density fluid (corresponding to the cold combustible mixture in the experiment) over a rearward facing step into a chamber containing low density fluid (the combustion products). The proportions of the computational domain are chosen equivalent to the combustor used by Smith and Zukoski. The surging flow is generated by passing a weak shock wave over the step, the constant velocity induced behind the shock wave representing the surging fluid. By passing the weak shock wave over the step, the slug of fluid above the step is accelerated impulsively. This is different from the sinusoidal acceleration that the fluid in the experiment experiences, but the behavior of the fluid is qualitatively the same. The flow to be modelled is shown schematically in fig(1.3). Three effects are investigated in the study. The first is the effect of the presence of the low density fluid in the chamber on the motion of the high density fluid entering

the chamber. Parametric studies are also done to determine the effects of changing the mean flow velocity (u_0) and the surge velocity (u_1) on the motion of the fluid entering the chamber.

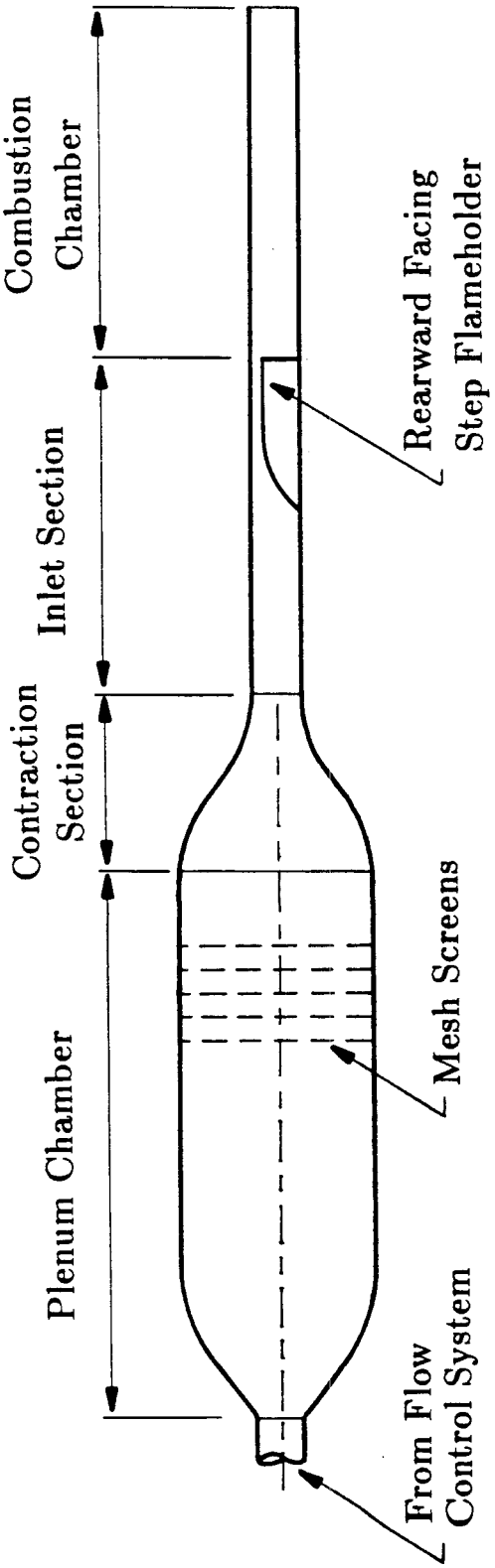

Figure (1.1) Schematic Diagram of the Apparatus used for the Combustion Instability Experiment.

VORTEX EVOLUTION

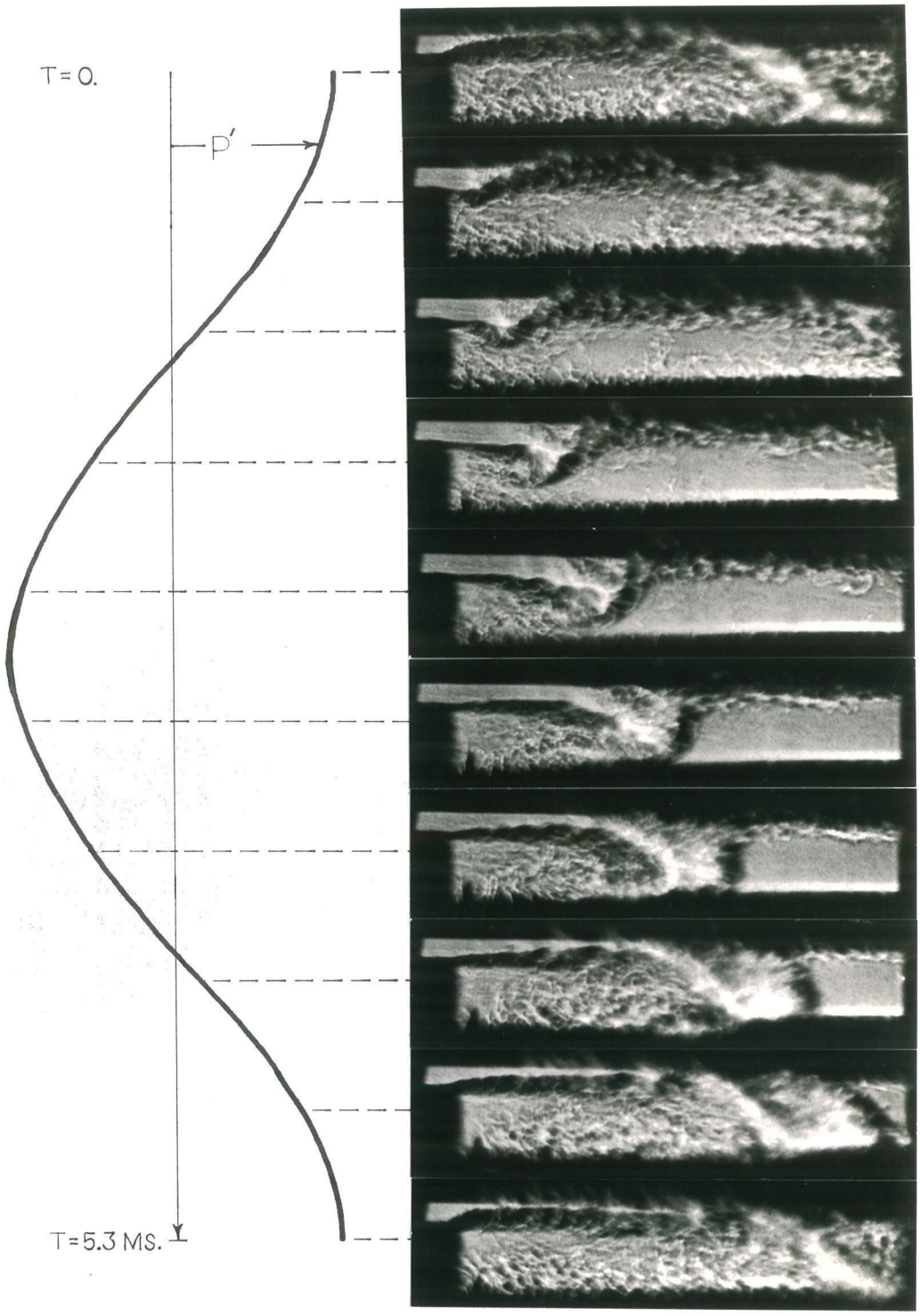

Figure (1.2) Vortex Evolution in the Combustion Chamber with Rearward Facing Step Flameholder.

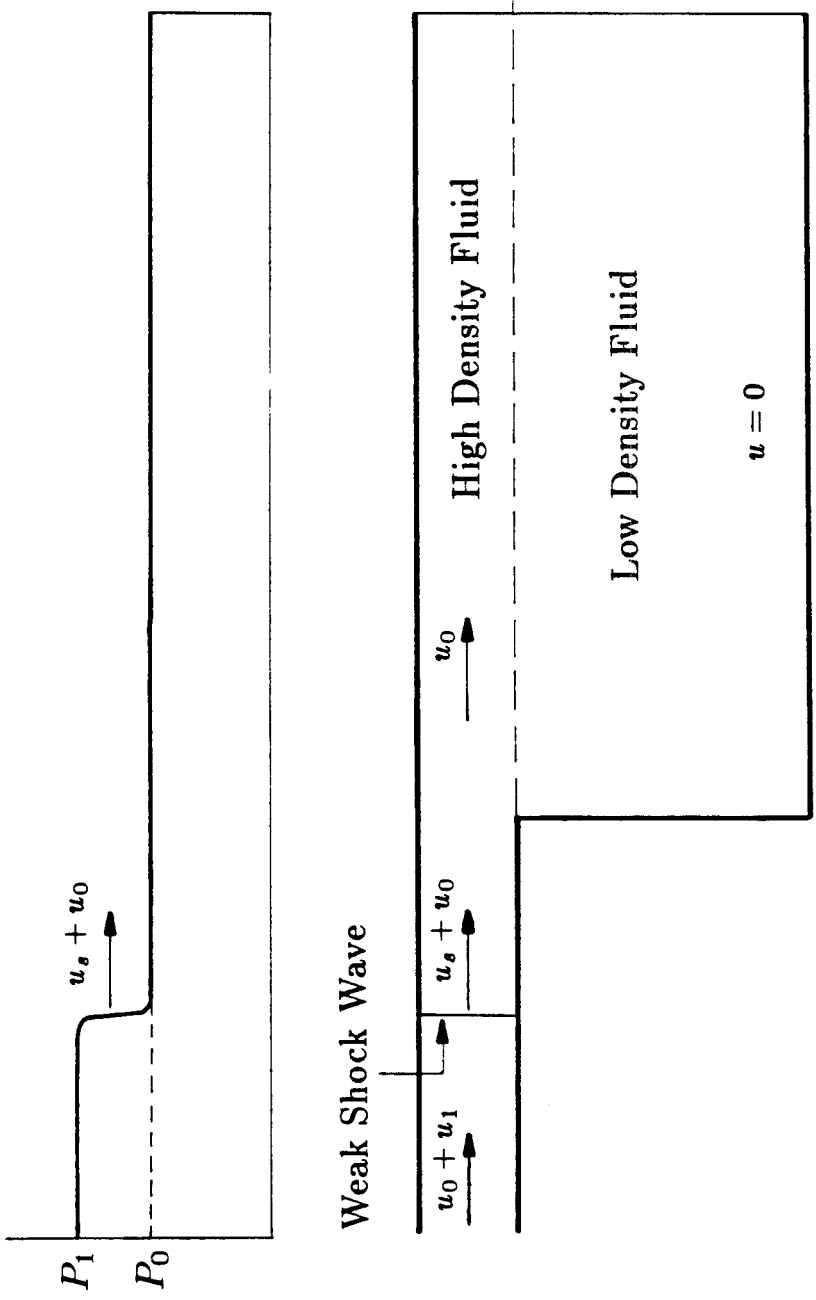

Figure (1.3) Initial Conditions for the Flow Field to be Modelled.

Chapter 2

Numerical Formulation

The computational code used in the study is a modification of one that was developed by Dr E. Baum at the TRW Space and Technology Group for the study of the interaction of shock waves with density stratified fluids. The code solves the Euler equations;

continuity:

$$\frac{\partial \rho}{\partial t} + \frac{\partial \rho u}{\partial x} + \frac{\partial \rho v}{\partial y} = 0 \tag{2.1}$$

x–momentum:

$$\frac{\partial \rho u}{\partial t} + \frac{\partial \rho u^2}{\partial x} + \frac{\partial \rho uv}{\partial y} + \frac{\partial P}{\partial x} = 0 \tag{2.2}$$

y–momentum:

$$\frac{\partial \rho v}{\partial t} + \frac{\partial \rho uv}{\partial x} + \frac{\partial \rho v^2}{\partial y} + \frac{\partial P}{\partial y} = 0 \tag{2.3}$$

energy conservation:

$$\frac{\partial e}{\partial t} + \frac{\partial \left(e + P\right) u}{\partial x} + \frac{\partial \left(e + P\right) v}{\partial y} = 0 \tag{2.4}$$

where

$$e = \frac{P}{\gamma - 1} + \tfrac{1}{2}\rho(u^2 + v^2) \tag{2.5}$$

for a polytropic gas, with boundary condition

$$u_n = 0 \tag{2.6}$$

(u_n =velocity normal to a solid boundary).

The equations are non–dimensionalized by the initial conditions in the cold gas ρ_0, P_0, c_0, and l, a reference length in the chamber. The non–dimensional variables are

$$\overline{P} = \frac{P}{P_0}, \qquad \overline{\rho} = \frac{\rho}{\rho_0}, \qquad \overline{u} = \frac{u}{c_0} \tag{2.7}$$

$$\overline{x} = \frac{x}{l}, \qquad \overline{y} = \frac{y}{l}, \qquad \overline{t} = \frac{t\, c_0}{l} \tag{2.8}$$

and

$$\overline{e} = \frac{\overline{P}}{\gamma(\gamma-1)} + \tfrac{1}{2}\overline{\rho}\left(\overline{u}^2 + \overline{v}^2\right) \tag{2.9}$$

The non–dimensionalized equations are

$$\frac{\partial \overline{\rho}}{\partial \overline{t}} + \frac{\partial \overline{\rho}\,\overline{u}}{\partial \overline{x}} + \frac{\partial \overline{\rho}\,\overline{v}}{\partial y} = 0 \tag{2.10}$$

$$\frac{\partial \overline{\rho}\,\overline{u}}{\partial \overline{t}} + \frac{\partial \overline{\rho}\,\overline{u}^2}{\partial \overline{x}} + \frac{\partial \overline{\rho}\,\overline{u}\,\overline{v}}{\partial \overline{y}} + \frac{\partial}{\partial \overline{x}}\left(\frac{\overline{P}}{\gamma}\right) = 0 \tag{2.11}$$

$$\frac{\partial \overline{\rho}\,\overline{v}}{\partial \overline{t}} + \frac{\partial \overline{\rho}\,\overline{u}\,\overline{v}}{\partial \overline{x}} + \frac{\partial \overline{\rho}\,\overline{v}^2}{\partial \overline{y}} + \frac{\partial}{\partial \overline{y}}\left(\frac{\overline{P}}{\gamma}\right) = 0 \tag{2.12}$$

$$\frac{\partial \overline{e}}{\partial \overline{t}} + \frac{\partial\left(\overline{e} + \frac{\overline{P}}{\gamma}\right)\overline{u}}{\partial \overline{x}} + \frac{\partial\left(\overline{e} + \frac{\overline{P}}{\gamma}\right)\overline{v}}{\partial \overline{y}} = 0 \tag{2.13}$$

with

$$\overline{u}_n = 0 \quad . \tag{2.14}$$

2.1 The Numerical Method

The non–dimensionalized equations are solved using the Flux–Corrected Transport (FCT) algorithm developed by Boris, Book and Hain (1973), (1975). A problem with standard numerical schemes is that they produce oscillations in the vicinity of large gradients in the flow variables (eg. in the vicinity of shock waves). The FCT algorithm overcomes this problem by employing a diffusive differencing scheme which prevents the formation of oscillations. This, however, has a smearing effect in the vicinity of large gradients in the solution variables. This problem is solved by employing a second "antidiffision" stage which corrects for the diffusive effects of the differencing scheme. In this way shock structures and contact surfaces between fluids of different density remain highly resolved and the problem of oscillation formation is not encountered. Details of the method can be found in the references given.

The code developed by Baum employs alternate direction splitting. For each time step all the terms in the differential equations involving x–derivatives are integrated first

along rows of constant y, followed by an integration of the y–derivative terms along columns of constant x. The problem at each time step therefore involves the solution of a succession of ordinary differential equations which leads to a significant simplification in the programming effort.

The computational grid is shown schematically in fig(2.1). The ratio of step height to channel height was kept constant and equal to $\frac{3}{4}$ for all the runs, this value corresponding to the step used by Smith and Zukoski in their experimental study. The computational grid consists of two sections. A one dimensional section extends from the inflow boundary to a certain location upstream of the step edge up to where the flow is assumed to be essentially one dimensional, since the effects of the step and the low density gas are not felt. A two dimensional section extends from the end of the one dimensional section to the outflow boundary as shown in fig(2.1). Because the flow structures of interest are fairly large, a rather course grid is used, 40 by 16 in the two dimensional section.

2.2 Boundary Conditions

The flow field generated in the geometry under consideration (represented in fig(2.2a)) would be exactly the same as that produced in fig(2.2b). The walls A and B of the channel are therefore reflecting boundaries. Simple reflecting boundary conditions are therefore used at these walls. Walls D and E, however, are not reflecting so a special treatment of the FCT algorithm using the zero normal velocity boundary condition was derived and employed in the code.

As an outflow boundary condition along boundary C, the slopes of the flow variables are assumed to be zero (Roache (1972)). This boundary condition, although not mathematically correct, worked well for small disturbances and caused the pressure wave to move out of the computational domain without any significant reflections. The same boundary condition was used at inflow, but the inflow boundary was chosen to be located sufficiently for upstream that, even if non–physical reflections were generated, they

would not reach the the field of interest in the computational run time.

2.3 Initial Conditions

For each computation the following parameters are specified; the density ratio of the high to low density fluid, the mean velocity of the high density fluid, and the static pressure ratio across the shock wave. The density ratio across the shock wave and the velocity induced behind the shock wave are calculated using the shock relations

$$\overline{\rho_1} = \frac{\rho_1}{\rho_0} = \frac{1 + \frac{\gamma+1}{\gamma-1}\overline{P}_1}{\frac{\gamma+1}{\gamma-1} + \overline{P}_1} \quad , \tag{2.15}$$

$$\overline{u}_1 = \frac{u_1}{c_0} = (\overline{P}_1 - 1)\left(\frac{2}{\gamma(\gamma+1)\overline{P}_1 + \gamma(\gamma-1)}\right)^{\frac{1}{2}} \tag{2.16}$$

where

$$\overline{P}_1 = \frac{P_1}{P_0} \tag{2.17}$$

(see Liepmann and Roshko (1957)). The zero subscripts refer to the initial conditions in the high density fluid ahead of the shock wave, the subscript 1 to the conditions behind the shock wave, and the subscript 2 to the conditions in the low density fluid. At the start of the computation the shock wave is located at the start of the two dimensional grid. The following initial conditions are therefore used;

for the fluid behind the shock wave

$$\overline{u} = \overline{u}_0 + \overline{u}_1 \tag{2.18}$$

$$\overline{P} = \overline{P}_1 \tag{2.19}$$

$$\overline{\rho} = \overline{\rho}_1 \tag{2.20}$$

$$\overline{e} = \frac{\overline{P}_1}{\gamma(\gamma-1)} + \tfrac{1}{2}\overline{\rho}_1(\overline{u}_0 + \overline{u}_1)^2 \tag{2.21}$$

for the high density fluid ahead of the shock wave

$$\overline{u} = \overline{u}_0 \tag{2.22}$$

$$\overline{P} = 1 \tag{2.23}$$

$$\overline{v} = 1 \tag{2.24}$$

$$\overline{e} = \frac{1}{\gamma(\gamma - 1)} + \tfrac{1}{2}\overline{u}_0{}^2 \tag{2.25}$$

and for the fluid in the low density region

$$\overline{u} = 0 \tag{2.26}$$

$$\overline{P} = 1 \tag{2.27}$$

$$\overline{\rho} = \overline{\rho}_2 = \frac{\rho_2}{\rho_0} \tag{2.28}$$

$$\overline{e} = \frac{1}{\gamma(\gamma - 1)} \tag{2.29}$$

The shock wave is released at dimensionless time $\bar{t} = 0$, and the position of the interface between the high and low density fluid is updated after each time step by utilizing the fluid velocities induced by the flow field at the interface. Graphical output of the position of the interface and the values of the flow variables is obtained after specified numbers of time steps.

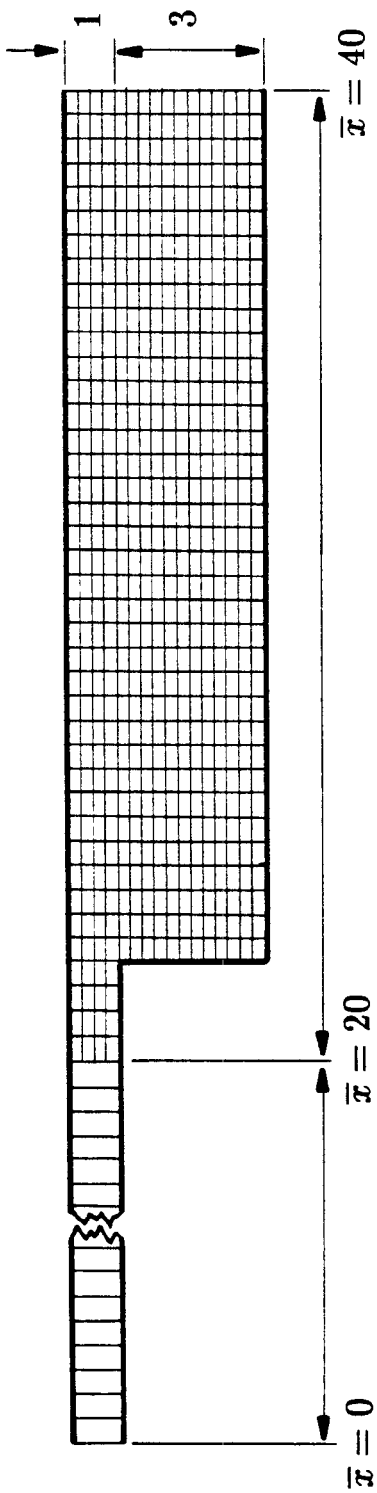

Figure (2.1) Mesh used for the Computational Study.

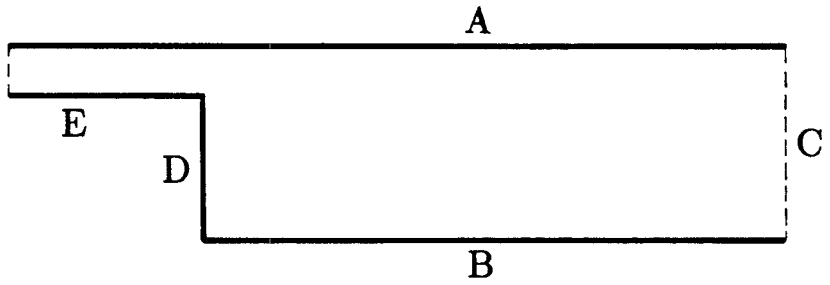

Figure (2.2) (a) Boundaries of the Computational Domain.
(b) Boundaries of the Equivalent Domain.

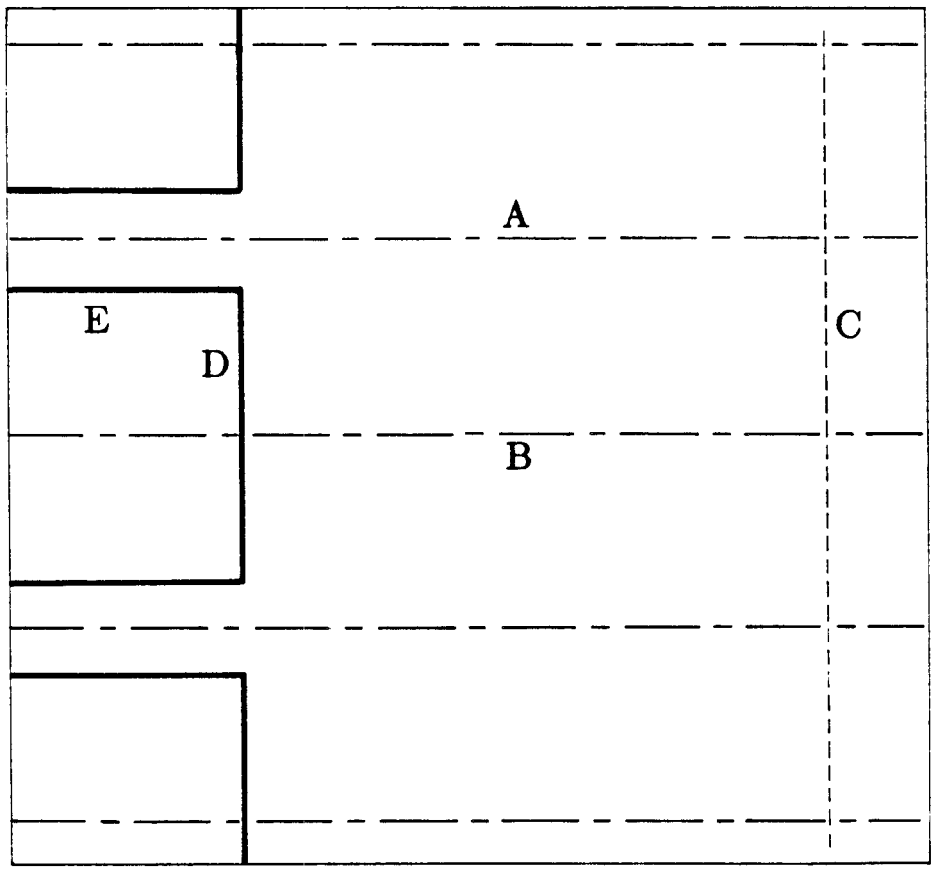

Chapter 3

Results and Discussion

In an effort to accomplish the objectives of the study outlined at the end of Chapter 1, the following program is followed. First, in order to determine the effect of the presence of the low density fluid in the chamber on the motion of the high density fluid entering the chamber, a comparative study is done in which the initial conditions (the surge velocity and the mean velocity of the high density fluid) are kept constant, but the density of the fluid in the chamber is changed. The flow field generated when the fluid in the chamber has the same density as the fluid entering the chamber is compared with the case in which the density ratio is 7 (approximately the ratio of the density of the combustion products to the fuel-air mixture in the experiment).

Second, in order to determine the effect of the mean velocity of the high density fluid entering the chamber on the flow field, the results of three computational runs in which the surge velocity is kept constant but the mean velocity varied, are presented. For this parametric study the ratio of the densities of the high to low density fluid is kept constant at 7. Third, in order to determine the effect of a change in the surge velocity on the flow field, the strength of the shock wave is varied while the other parameters are kept constant.

Before the results of the parametric studies are given, the behavior of the flow field for a particular set of initial conditions (mean flow velocity $\bar{u}_0 = 0.125$, surge velocity $\bar{u}_1 = 0.0686$, density ratio $\bar{\rho}_2 = \frac{1}{7}$) will be considered in some detail. The sequence of figures 3.1–3.7 represents the behavior of the flow field and flow field variables at selected dimensionless times. The chamber was seeded with particles located, at the dimensionless time $\bar{t} = 0$, at the positions shown in fig(3.1a). Here, and in all subsequent figures, particles that are adjacent initially are connected by straight lines. Particles in the low density fluid are not connected to adjacent particles in the high density

fluid. Fig(3.1b) shows the important flow variables on the lower wall. Fig(3.1c) shows the channel geometry with a line representing the boundary between the high and low density fluid. Fig(3.1d) shows the values of the flow variables along the upper wall of the chamber. In the figures representing the flow variables, the curves are normalized by the maximum value of each particular variable in the domain of interest. The maximum value for each of the variables is given at the right hand side of each graph. It should also be noted that the horizontal scales of the figures representing the channel geometry have been compressed. The scale length l defined in Chapter 2 corresponds to the height of the inlet section to the chamber. The step is three units high and the total length of the section represented in the figures is twenty units. Figure (3.2) shows the flow field and flow field variables at $\bar{t} = 2.303$. This figure depicts the time at which the shock wave has reached the edge of the step. This is apparent from the graph representing the flow variables along the top wall. In fig(3.2a) the particle that was at the edge of the step at $\bar{t} = 0$ is marked with an asterisk. The displacement of this particle away from the edge of the step is due to the mean velocity that was given to the upper, high density fluid as an initial condition, since the shock wave has not reached this position yet.

Now as the shock wave moves into the chamber, the fluid behind it surges over the step, shedding a sheet of vorticity into the chamber. Studies (both analytical and experimental) on the start up flows over wedges (eg. the analytical study by Pullin (1978)) have shown that the vortex sheets of finite extent shed from such bodies tend to roll up at their leading edges. The effect of the discrete vortex formed by the rolling up of the vortex sheet shed from the step is noticeable in fig(3.3) from the deformation of the interface between the high and low density fluid. In this figure the shock wave, considerably weakened by its expansion into the large channel area, is located at $\bar{x} \approx 37$ on the lower wall and $\bar{x} \approx 32$ on the upper wall. The difference in the propagation speeds of the pressure waves is due to the fact that the sound speed is much higher in the low

density fluid in the vicinity of the lower wall than in the high density fluid in the vicinity of the upper wall.

Subsequent figures show the deformation of the interface between the high and low density fluid for increasing dimensionless times. Fig(3.4) for $\bar{t} = 12.564$ shows the flow field and flow field variables for a time after which the pressure wave has left the computational domain. The flow variables at the outflow boundary go to the conditions behind the pressure wave without any significant reflections, which is an indication that the simple outflow boundary conditions used work fairly well. In fig(3.5) ($\bar{t} = 21.534$) the clockwise rotational velocity induced by the vortex shed from the edge of the step is starting to be felt at the lower wall. This is apparent from the negative horizontal velocity at the wall in the vicinity of the foot of the step, which is in opposition to the positive horizontal velocity induced behind the pressure wave. This is even more apparent in fig(3.6) ($\bar{t} = 28.259$). The motion of the tongue of high density fluid induced by the vortex is shown more clearly in this figure. This tongue of high density fluid moves into the low density fluid and approaches the lower wall at large times (fig(3.7), $\bar{t} = 51.813$).

The effect of the presence of the low density fluid on the flow field will now be examined. Fig(3.8) shows the flow field generated by a surging flow with initial conditions $\overline{u}_0 = 0.125$ and $\overline{u}_1 = 0.240$. In this case the fluid in the chamber has the same density as the fluid entering it. Fig(3.9) shows the flow field generated with the same initial conditions, but with low density fluid present in the chamber. By examining the figures it is clear that a significant difference exists in the motion of the fluid entering the chamber. The fluid in fig(3.8) tends to roll up in an elliptical structure (which appears to be circular because of the compressed horizontal scale). When the low density fluid is present, however, a tongue of high density fluid from the upper stream moves downward toward the lower wall with a small degree of rolling around the vortex. A possible explanation

for the observed difference in the structure of the flow field is the following. The fluid that the vortex is tending to rotate is subject to a centrifugal acceleration. When the high density fluid moves into the low density medium, it experiences a buoyancy force directed away from the center of the vortex. This fluid, instead of moving in an elliptical path, moves around the vortex in a path of increasing distance away from the center of the vortex. It therefore appears to move toward the lower wall instead of around the center of the vortex. In the constant density case, however, the buoyancy force is absent so the fluid moves in the the elliptical path (which is elliptical rather than circular due to the presence of the walls) prescribed by the vortex. The motion of the high density fluid in the numerical computation is similar to that observed in the combustion experiment of Smith and Zukoski.

To determine the effect of variations in the mean velocity, the surge velocity is kept constant at 0.247 and the results of three different computations for values of the mean velocity equal to 0.250, 0.125 and 0.0625 are presented in figs(3.10), (3.9) and (3.11) respectively. From these figures it is clear that the generated flow fields are fundamentally the same, the high density fluid reaching the lower wall at approximately the same dimensionless time. However, because of the different magnitudes of the mean velocity, the position downstream of the step at which the high density fluid reaches the lower wall is different in the three cases. The time taken for the fluid to reach the lower wall, however, is the most important result since, in the combustion experiment, it represents the delay time after which significant mixing and therefore significant combustion occurs.

To study the effect of varying the surge velocity, computations were done in which the mean flow velocity was kept constant at 0.125 and different surge velocities were used ($\overline{u}_1 = 0.247$–the surge velocity for the previous case, $\overline{u}_1 = 0.132$, and $\overline{u}_1 = 0.0686$). The results are show in figs(3.9),(3.12) and (3.13). As expected, because the strength of the vortex sheet and therefore the strength of the vortex formed at its apex is increased

with increasing surge velocity, the downward velocity induced by the vortex on the high density fluid is much larger. The high density fluid therefore reaches the lower wall in much shorter times for higher surge velocities. The position of the lower extremity of the tongue of high density fluid is plotted against dimensionless time for the different surge velocities in fig(3.14). From this plot it is apparent that the lower extremity of the high density fluid moves toward the wall at constant velocity. These constant vertical velocities are plotted against the surge velocity in fig(3.15).

The results of the computational study are now compared to the experiment for two different vortex shedding frequencies, 188Hz and 446Hz. The surge velocities for the 188Hz and 446Hz cases are 42m/s and 24m/s respectively. For a sound speed of 340m/s in the fuel–air mixture entering the chamber (the reference state in the calculation) these correspond to $\overline{u}_1 = 0.124$ for the 188Hz case and $\overline{u}_1 = 0.071$ for the 466Hz case. From fig(3.15) the non–dimensional vertical velocities corresponding to these surge velocities are $\overline{v} = 0.08$ (188Hz) and $\overline{v} = 0.05$ (446Hz). For the step height of 19mm the times taken for the high density fluid to reach the lower wall in the two cases are $\overline{t} = 0.7$ms (188Hz) and $\overline{t} = 1.1$ms (446Hz).

Now from figs(3.16) and (3.17) the actual times taken for the high density fluid to reach the lower wall are approximately 2.6ms (188Hz) and 1.5ms (446Hz). The calculation therefore yields a time fairly close to the experimental result in the 446Hz case but agreement is poor in the 188Hz case. By examining figs(3.16) and (3.17) carefully the reason for this is clear. Because the fluid above the step is accelerated sinusoidally in the experiment, the leading edge of the vortex sheet shed from the step is not as strong as that in the calculation where the fluid is accelerated impulsively. The edge of the vortex sheet will therefore have less of a tendency to roll up in the experiment than in the calculation, and the discrete vortex formed will also be weaker. This vortex will induce lower vertical velocities in the high density fluid and the time taken for the fluid

in the experiment to reach the lower wall will therefore be larger. Now in the 188Hz case the surge velocity at the edge of the step reaches its maximum value (corresponding to the minimum of the pressure fluctuation curve) at the time that the high density fluid impinges on the bottom wall. In the 446Hz case, however, the velocity of the fluid above the step reaches its maximum value (frame three of the shadowgraph sequence) before a significant amount of the high density fluid has moved away from the edge of the step. This case therefore corresponds more closely to the calculation. This is evident from the close agreement between the results of the experiment and the calculation for this case.

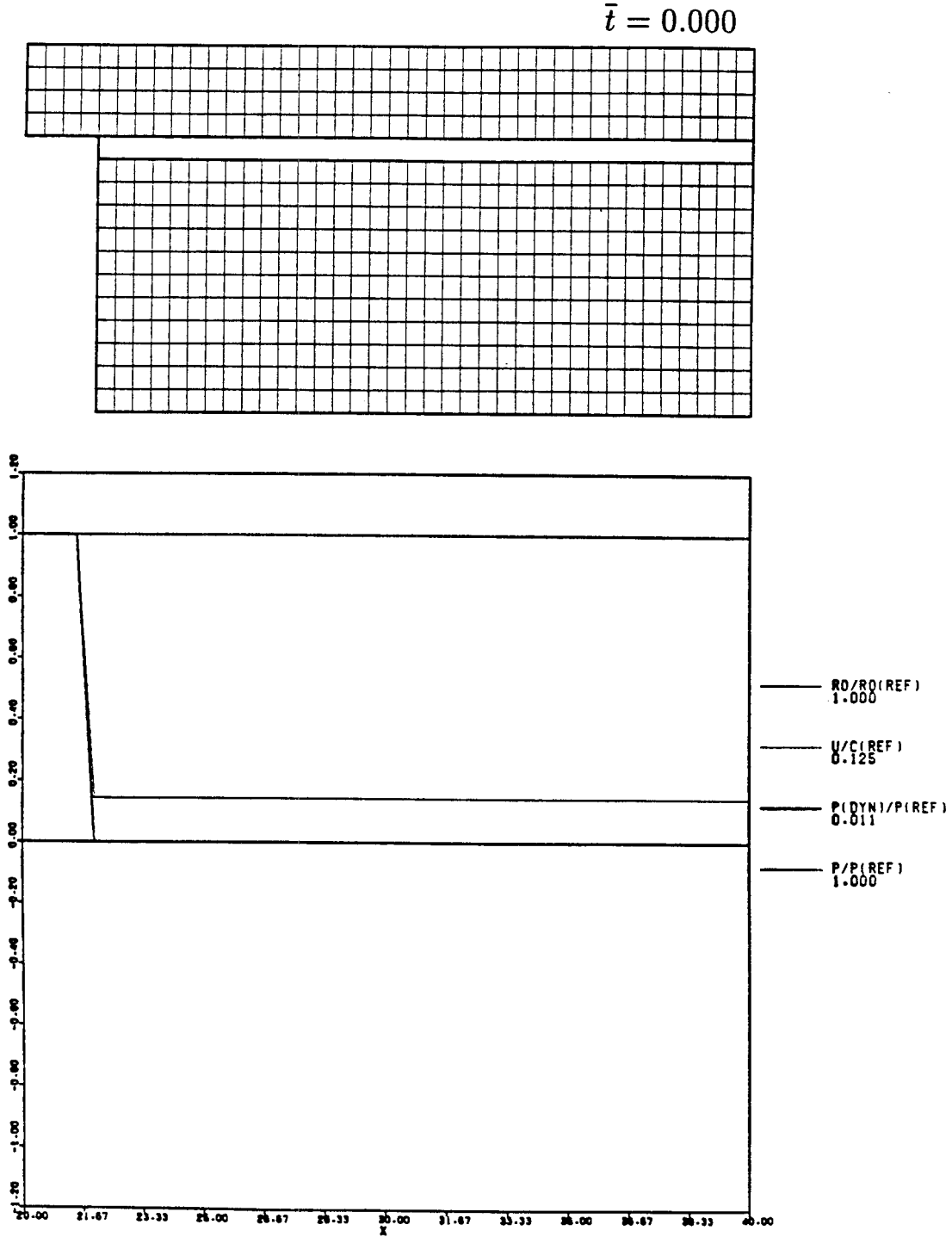

Figure (3.1) (a) Positions of Particles at $\bar{t} = 0.000$ for a Flow Field with Initial Conditions $\overline{u}_0 = 0.125$, $\overline{u}_1 = 0.0686$ and $\overline{\rho}_2 = \frac{1}{7}$.

(b) Flow Field Variables along the Lower Wall.

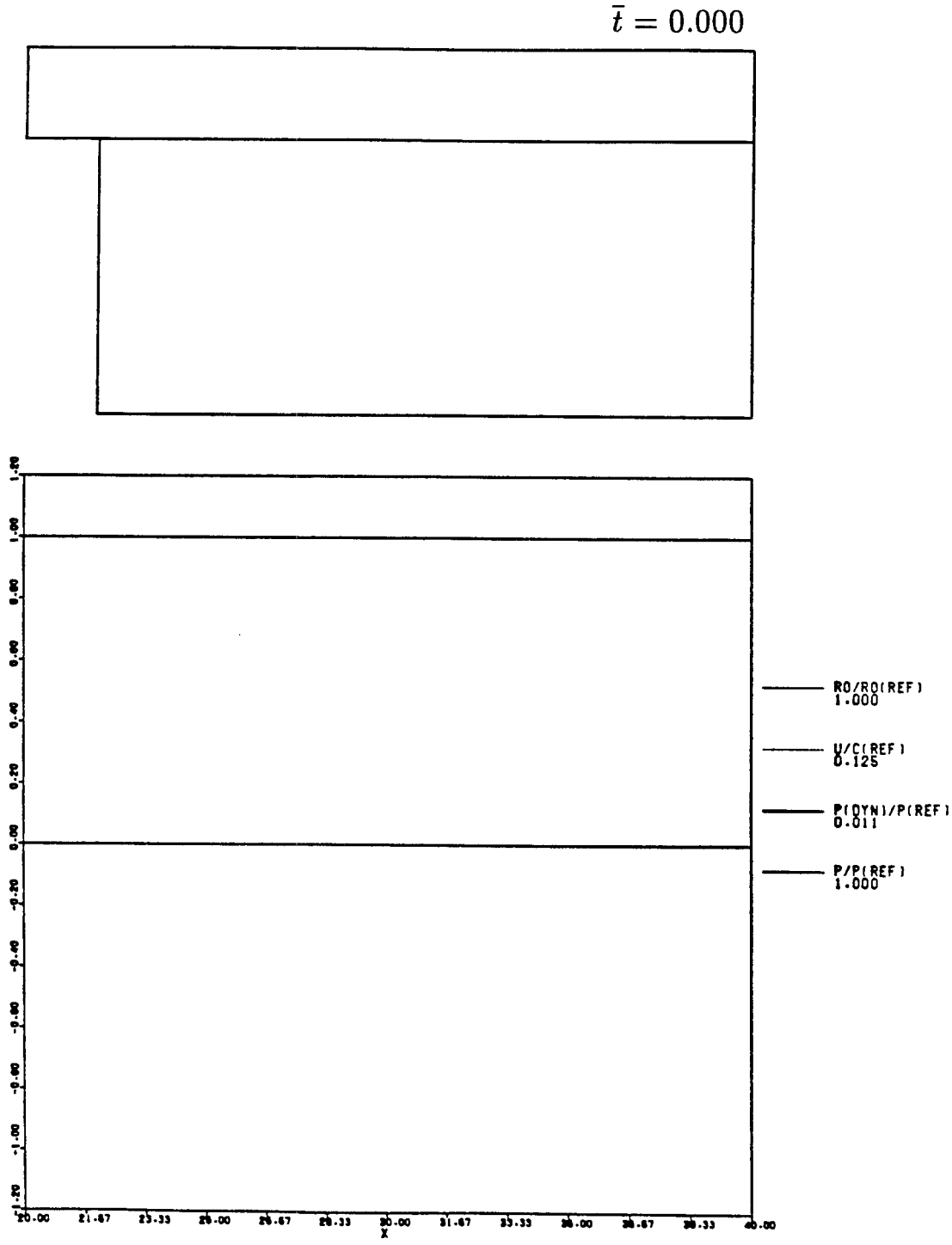

Figure (3.1) (c) Position of Interface Between High and Low Density Fluid.

(d) Flow Field Variables along the Upper Wall.

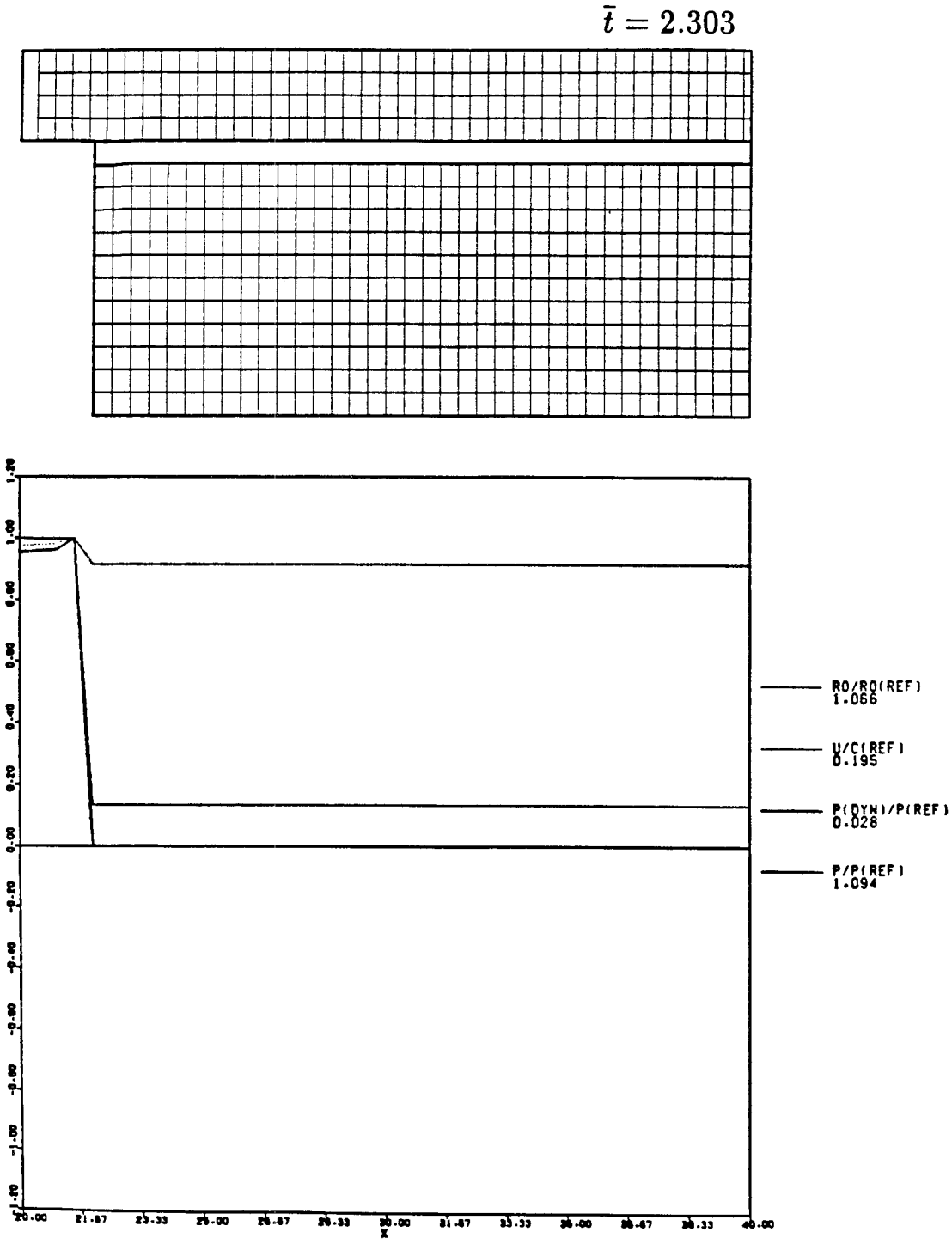

Figure (3.2) (a) Positions of Particles at $\bar{t} = 2.303$ for a Flow Field with Initial Conditions $\overline{u}_0 = 0.125$, $\overline{u}_1 = 0.0686$ and $\overline{\rho}_2 = \frac{1}{7}$.

(b) Flow Field Variables along the Lower Wall.

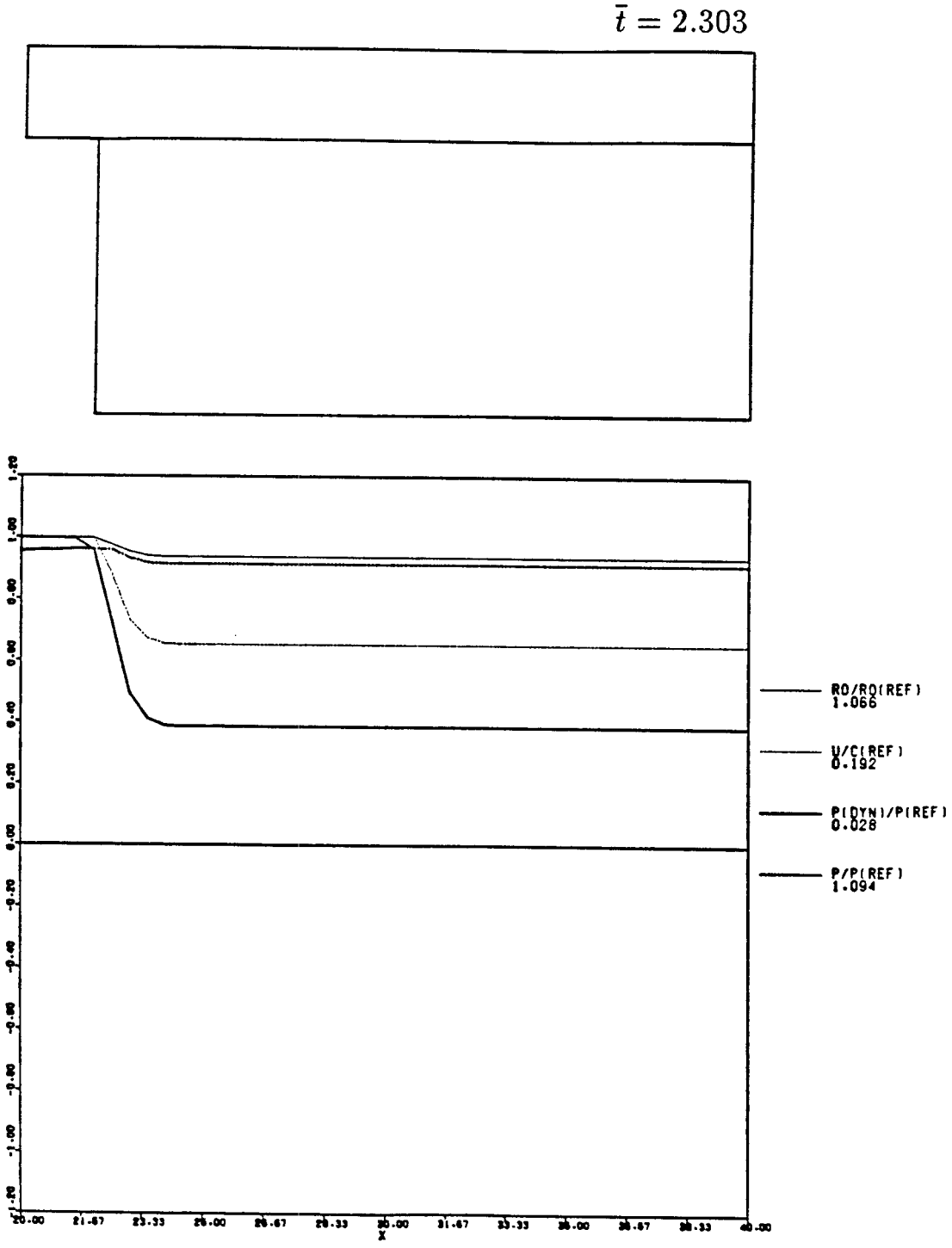

Figure (3.2) (c) Position of Interface Between High and Low Density Fluid.

(d) Flow Field Variables along the Upper Wall.

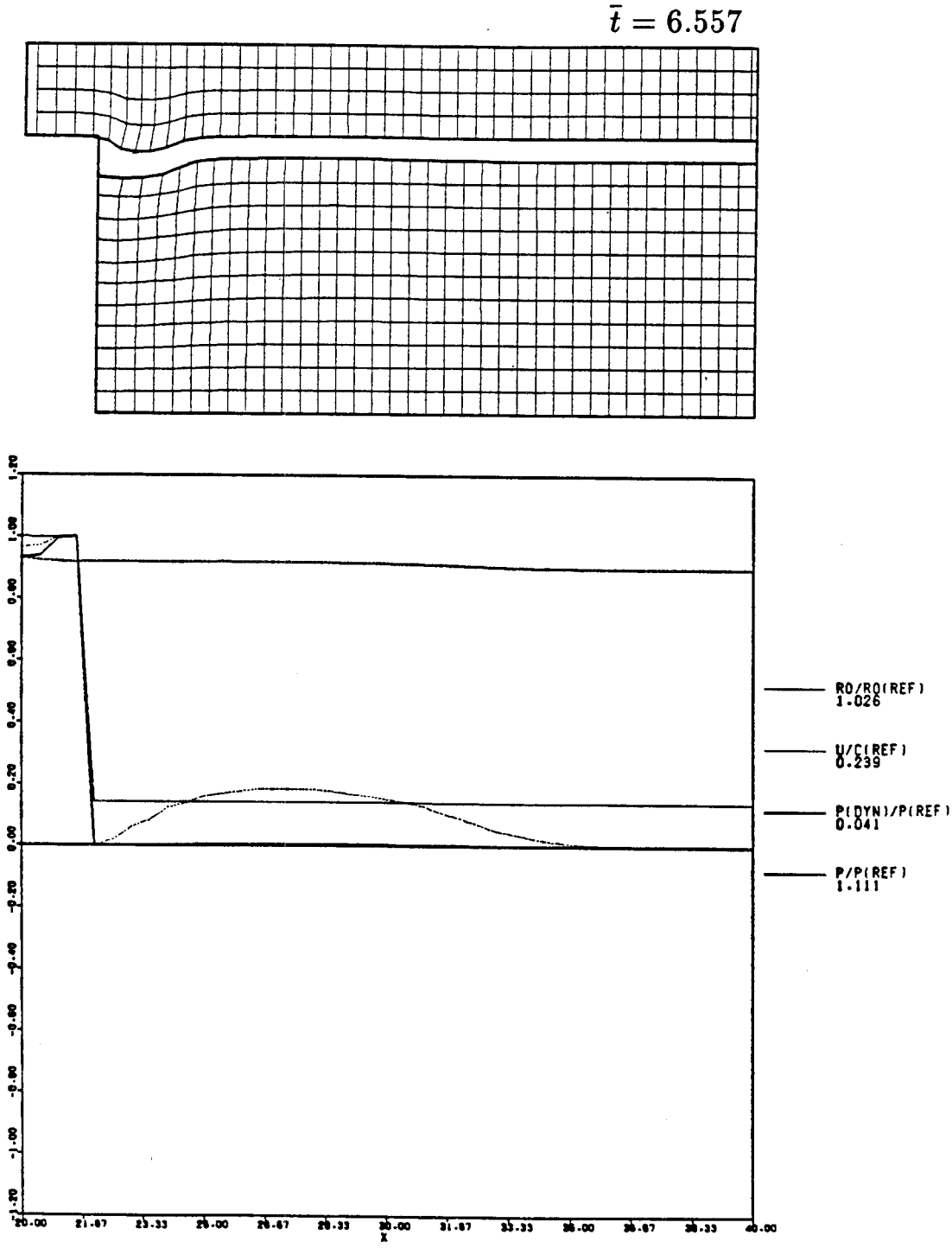

Figure (3.3) (a) Positions of Particles at $\bar{t} = 6.557$ for a Flow Field with Initial Conditions $\overline{u}_0 = 0.125$, $\overline{u}_1 = 0.0686$ and $\overline{\rho}_2 = \frac{1}{7}$.

(b) Flow Field Variables along the Lower Wall.

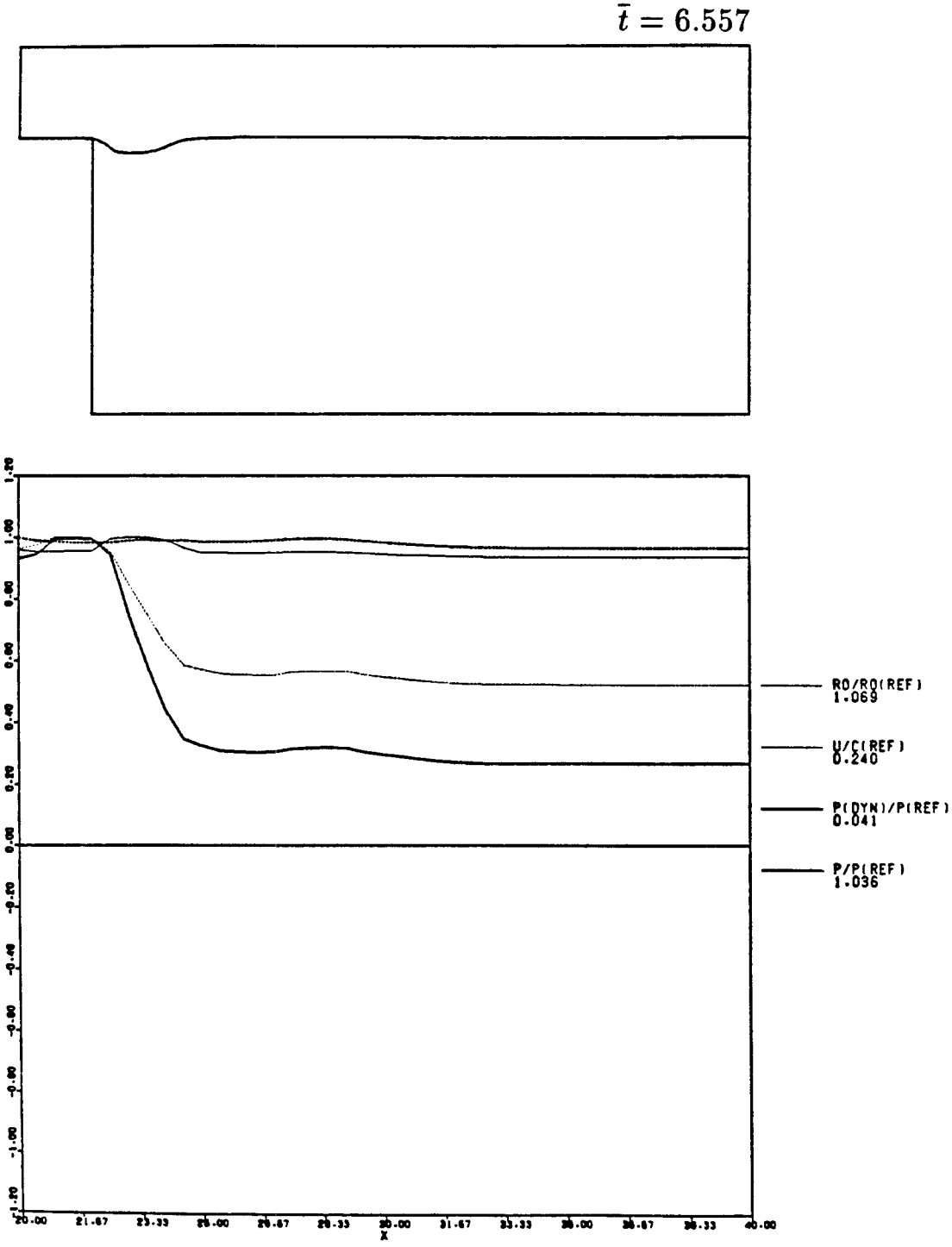

Figure (3.3) (c) Position of Interface Between High and Low Density Fluid.

(d) Flow Field Variables along the Upper Wall.

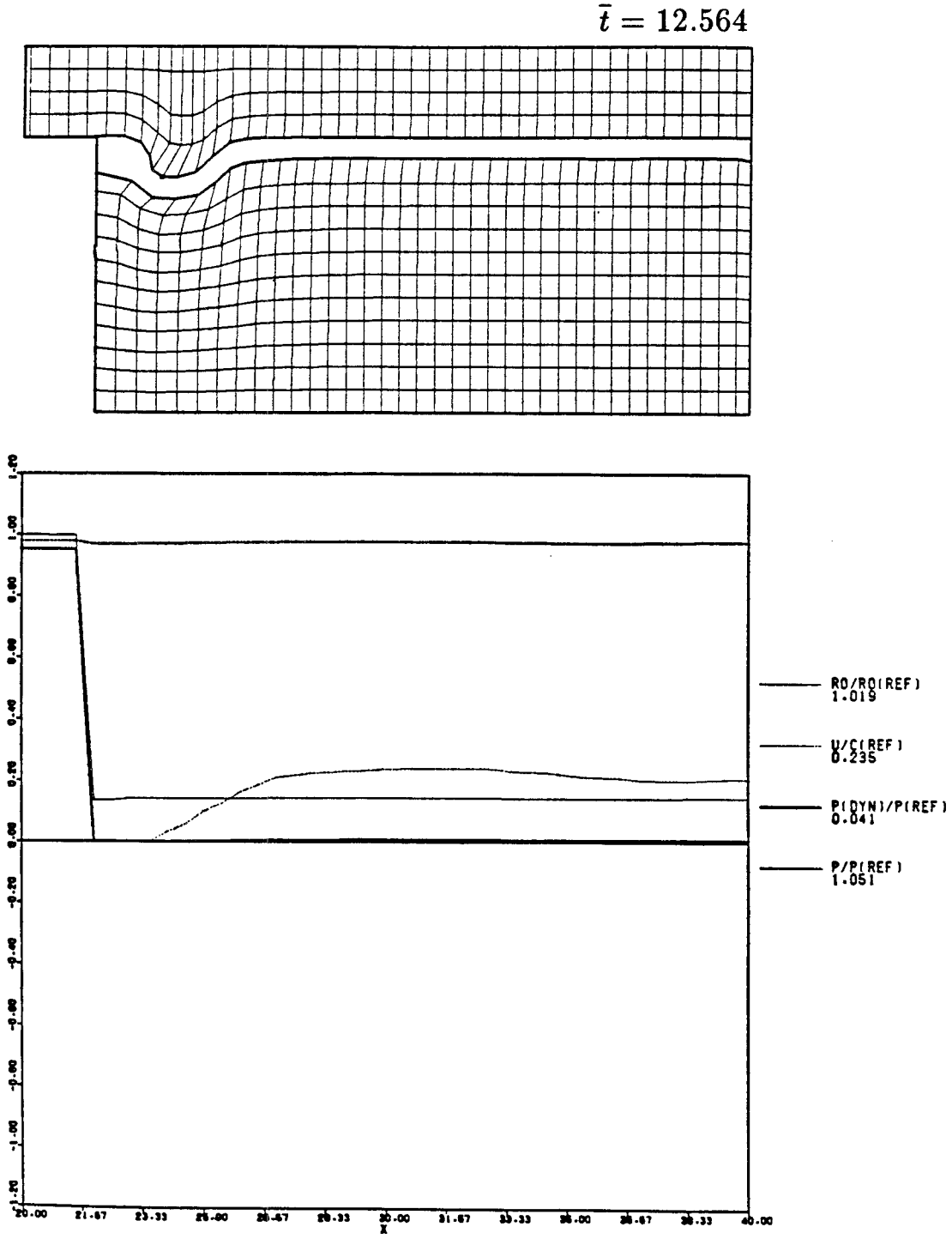

Figure (3.4) (a) Positions of Particles at $\bar{t} = 12.564$ for a Flow Field with Initial Conditions $\overline{u}_0 = 0.125$, $\overline{u}_1 = 0.0686$ and $\overline{\rho}_2 = \frac{1}{7}$.

(b) Flow Field Variables along the Lower Wall.

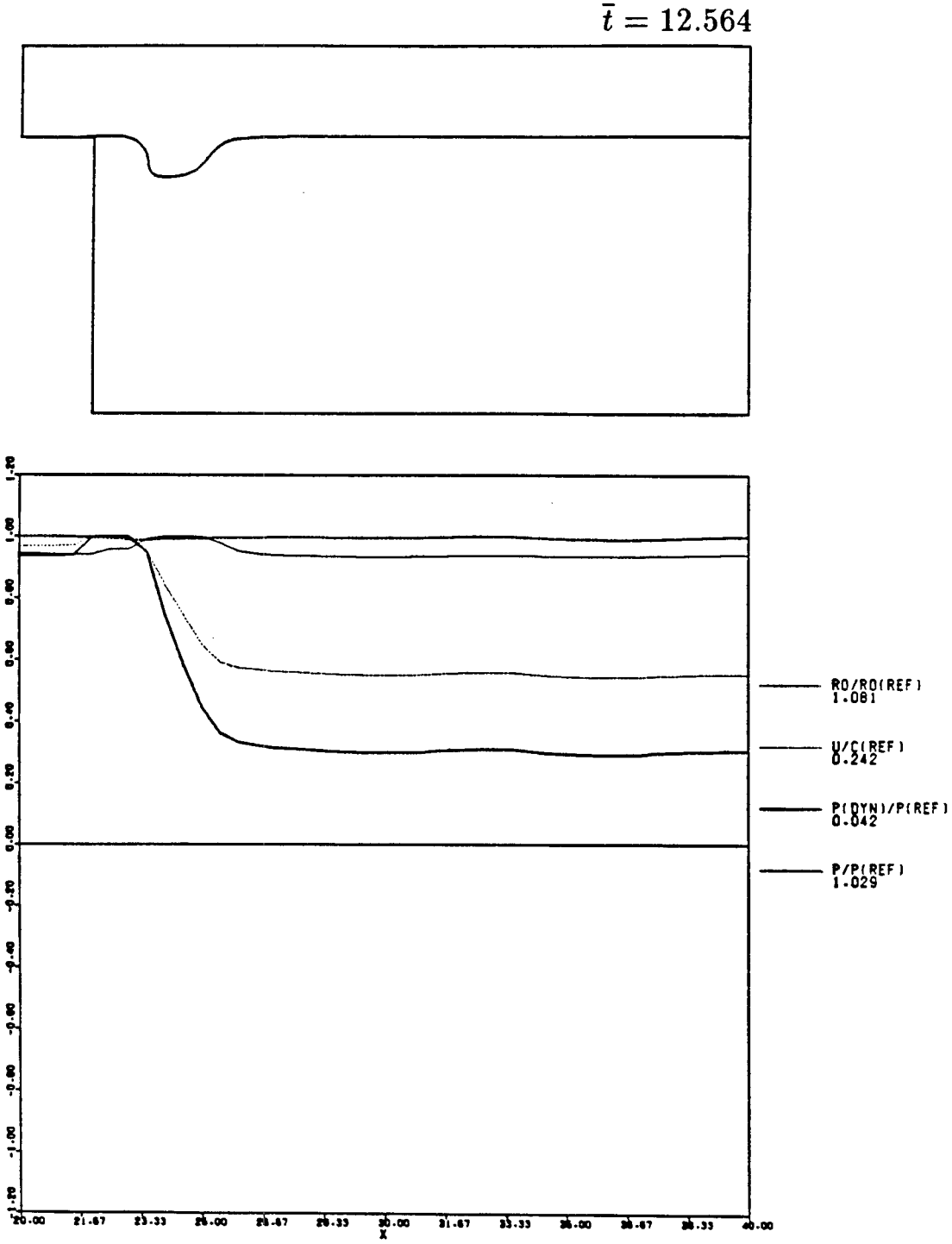

Figure (3.4) (c) Position of Interface Between High and Low Density Fluid.

(d) Flow Field Variables along the Upper Wall.

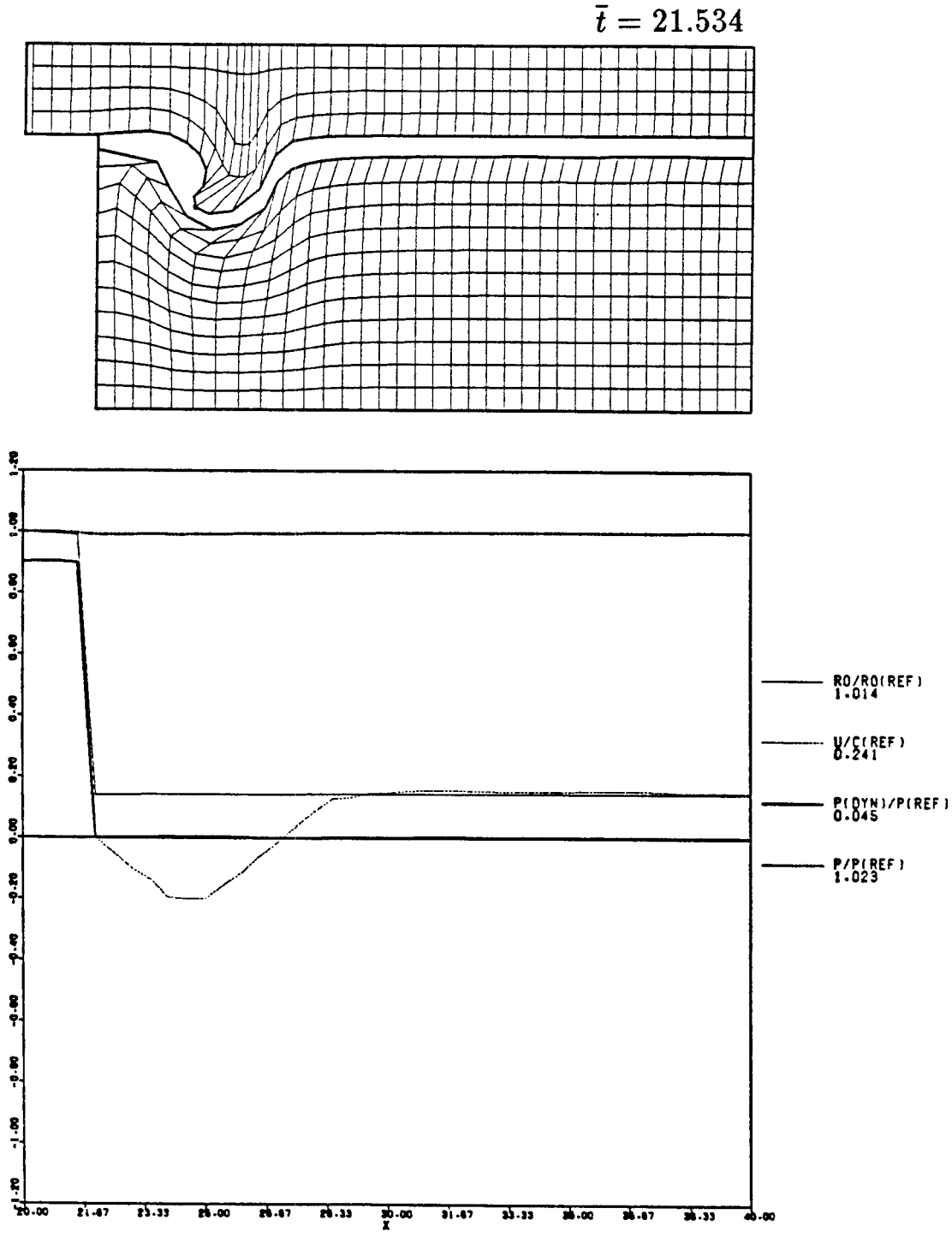

Figure (3.5) (a) Positions of Particles at $\bar{t} = 21.534$ for a Flow Field with Initial Conditions $\bar{u}_0 = 0.125$, $\bar{u}_1 = 0.0686$ and $\bar{\rho}_2 = \frac{1}{7}$.

(b) Flow Field Variables along the Lower Wall.

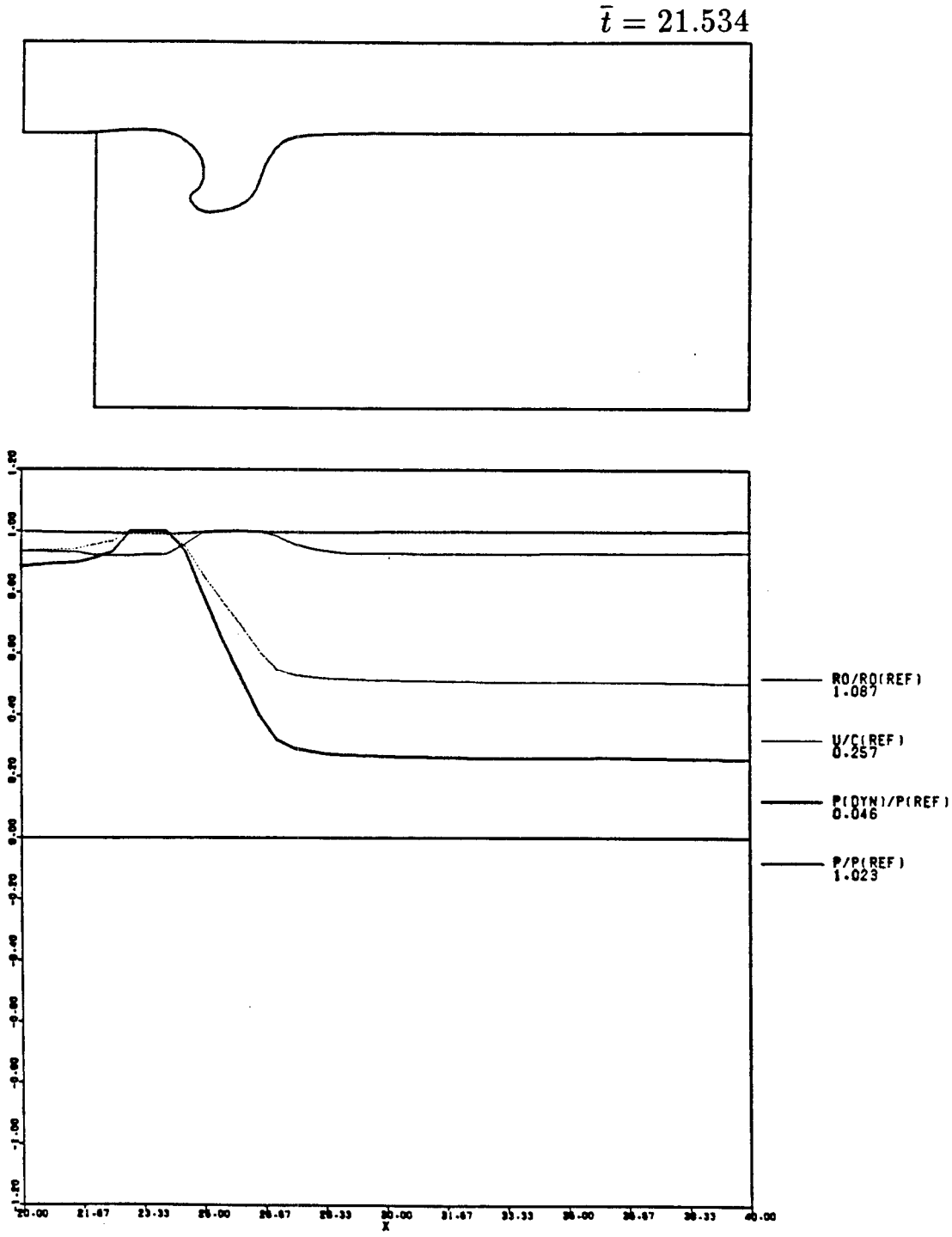

Figure (3.5) (c) Position of Interface Between High and Low Density Fluid.

(d) Flow Field Variables along the Upper Wall.

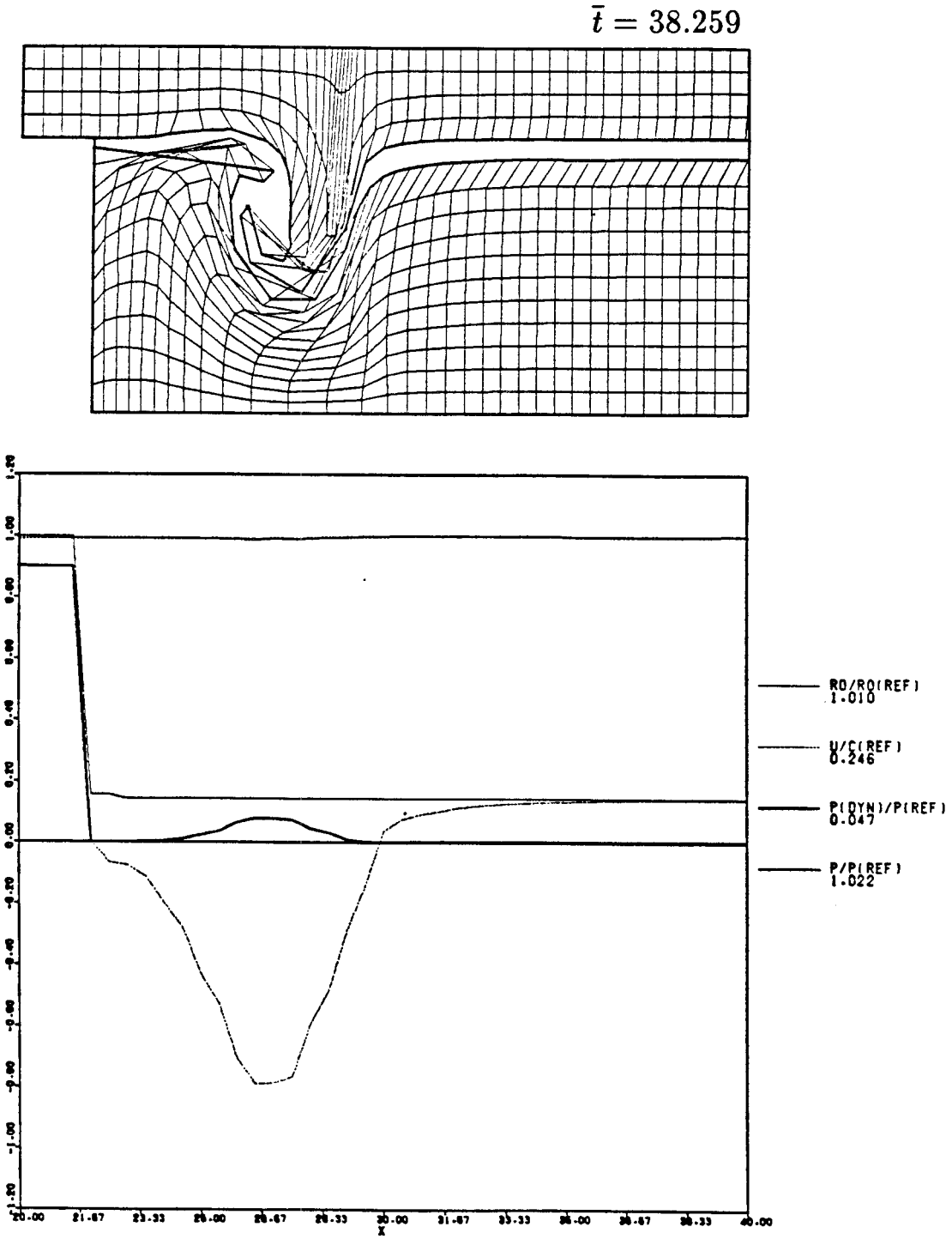

Figure (3.6) (a) Positions of Particles at $\bar{t} = 38.259$ for a Flow Field with Initial Conditions $\bar{u}_0 = 0.125$, $\bar{u}_1 = 0.0686$ and $\bar{\rho}_2 = \frac{1}{7}$.

(b) Flow Field Variables along the Lower Wall.

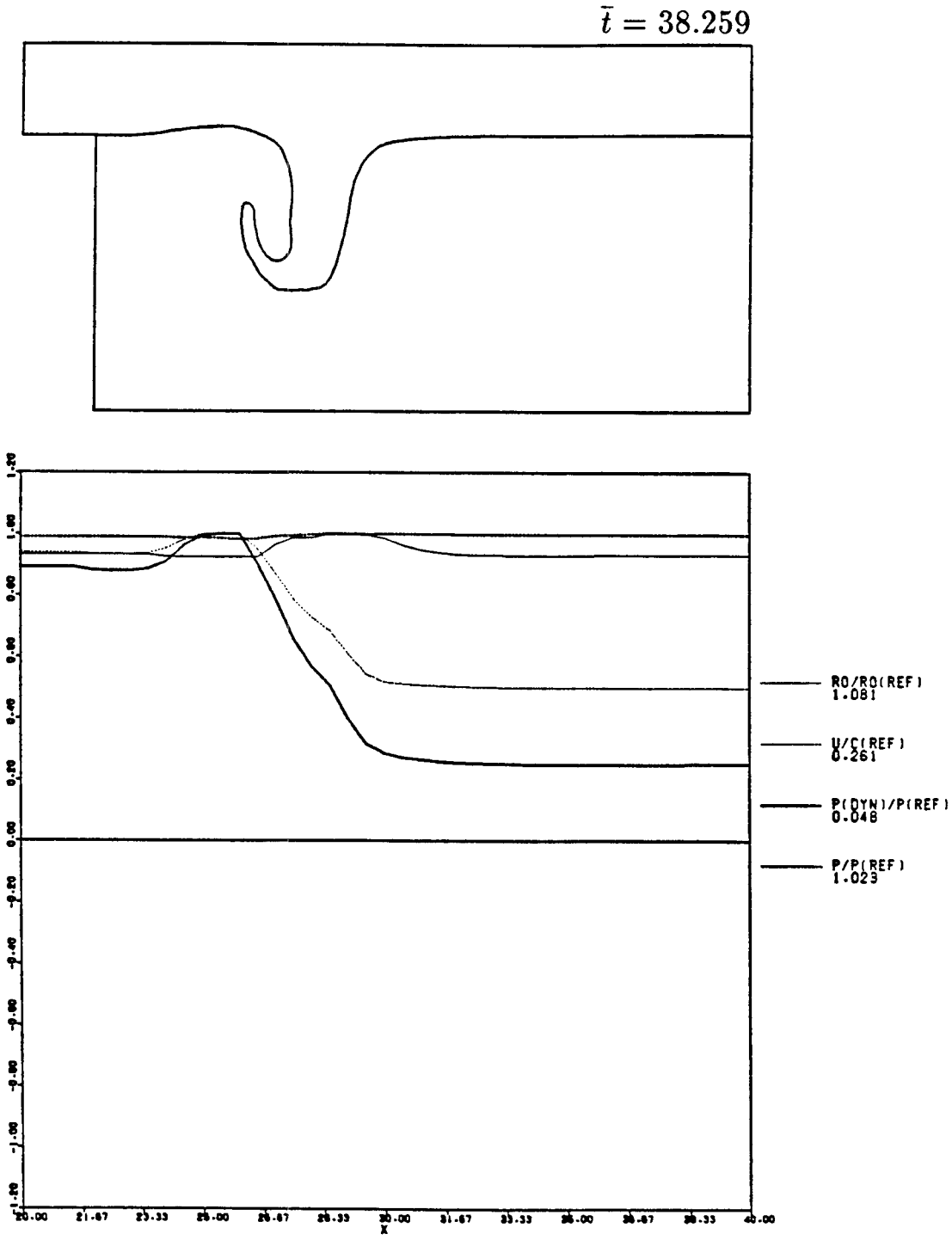

Figure (3.6) (c) Position of Interface Between High and Low Density Fluid.

(d) Flow Field Variables along the Upper Wall.

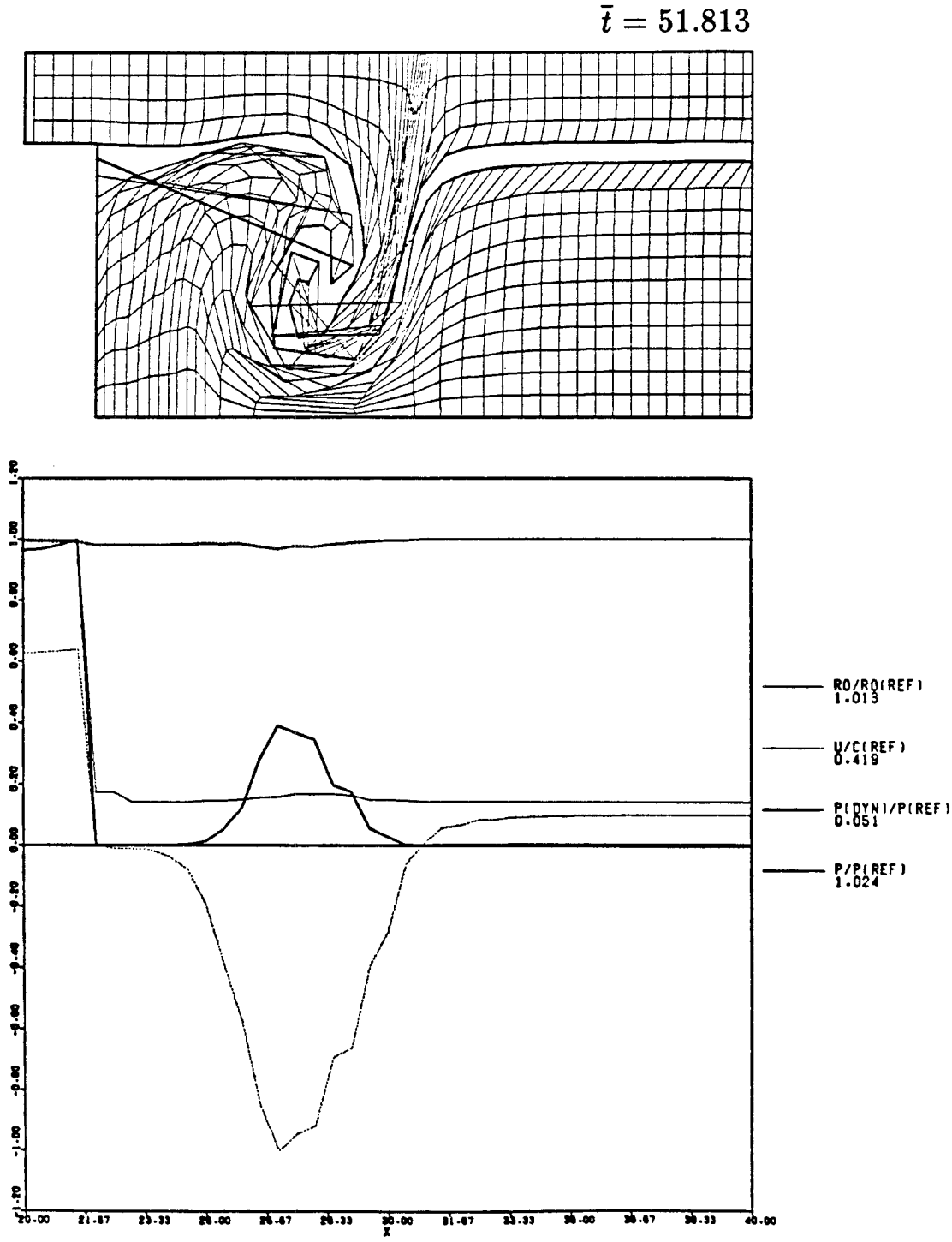

Figure (3.7) (a) Positions of Particles at $\bar{t} = 51.813$ for a Flow Field with Initial Conditions $\bar{u}_0 = 0.125$, $\bar{u}_1 = 0.0686$ and $\bar{\rho}_2 = \frac{1}{7}$.

(b) Flow Field Variables along the Lower Wall.

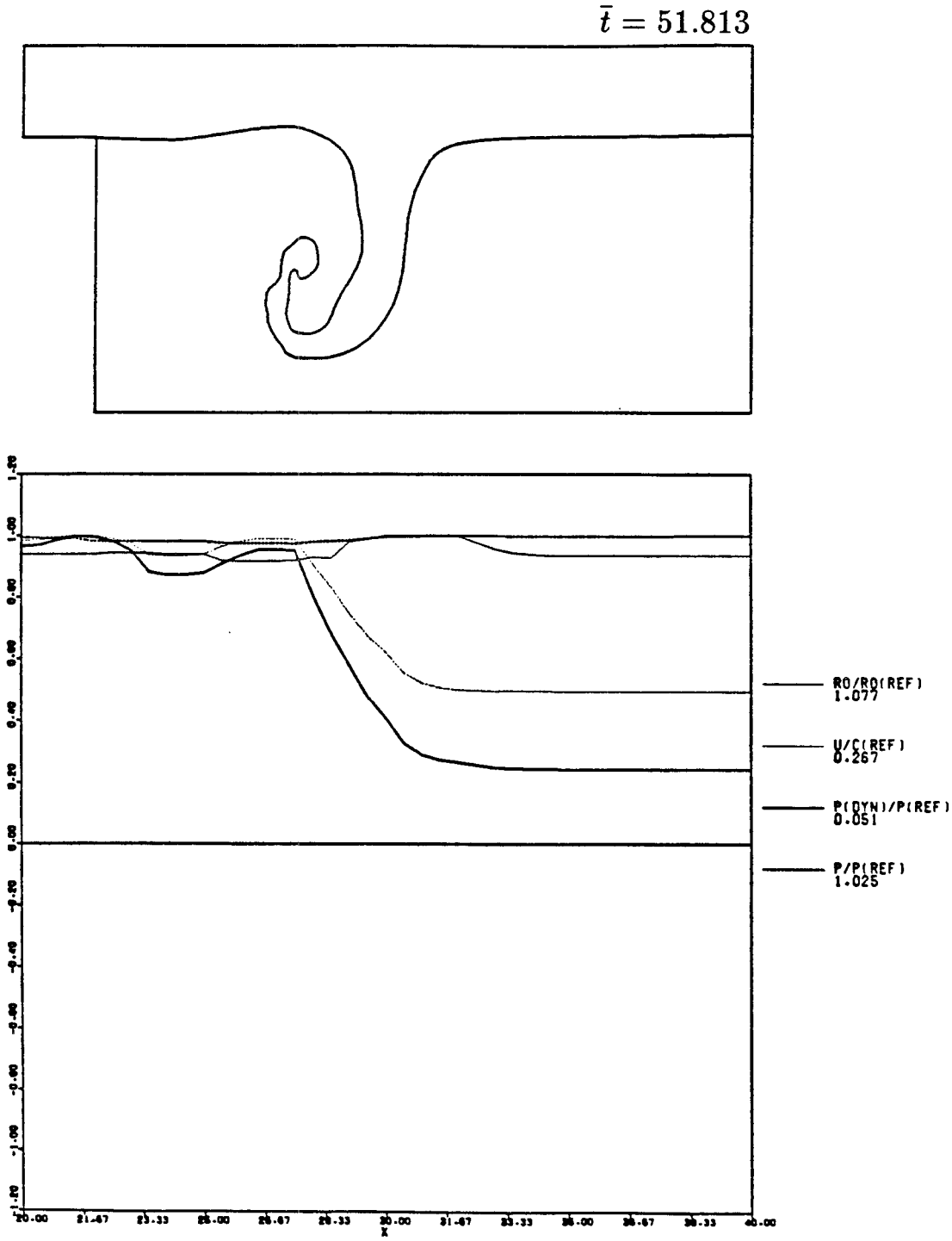

Figure (3.7) (c) Position of Interface Between High and Low Density Fluid.

(d) Flow Field Variables along the Upper Wall.

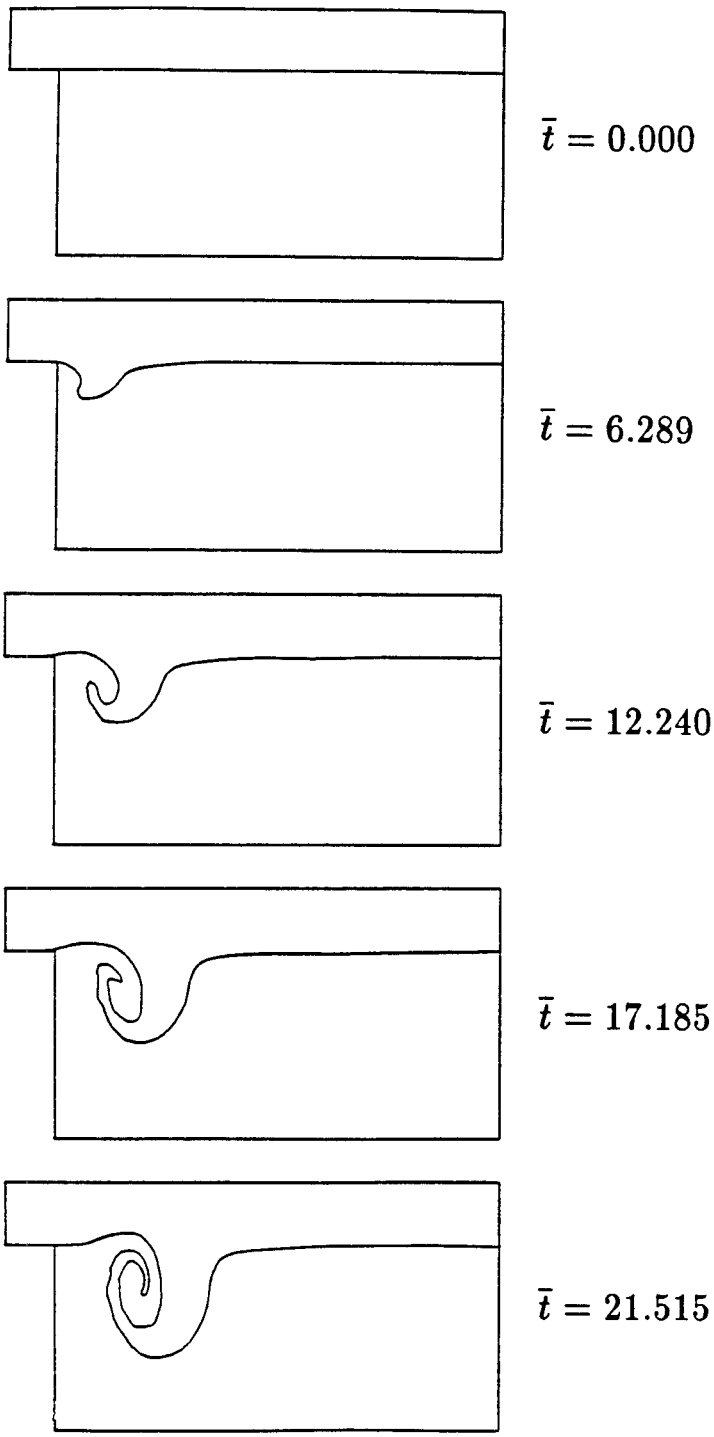

Figure (3.8) Flow Field Induced By the Surging Flow over the Rearward Facing Step for $\overline{u}_0 = 0.125$, $\overline{u}_1 = 0.247$ and $\overline{\rho}_2 = 1$.

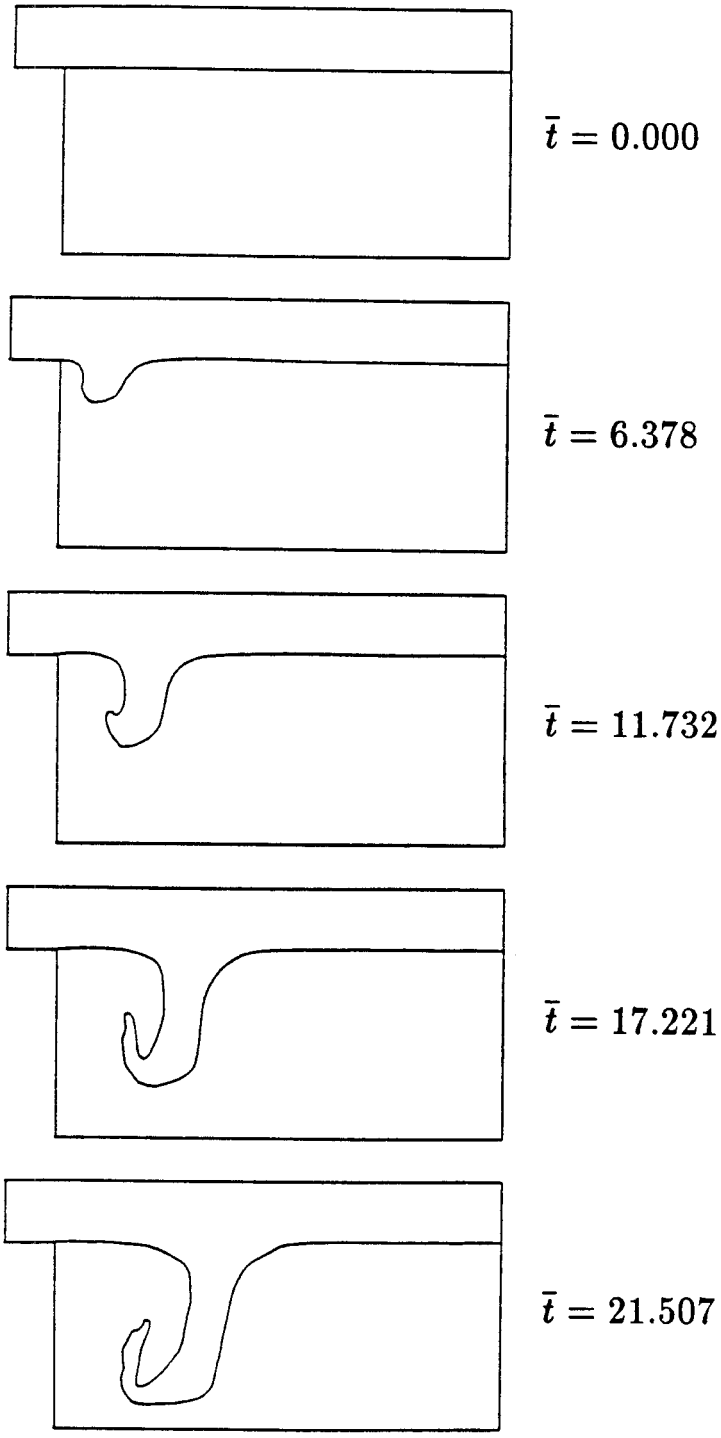

Figure (3.9) Flow Field Induced By the Surging Flow over the Rearward Facing Step for $\overline{u}_0 = 0.125$, $\overline{u}_1 = 0.247$ and $\overline{\rho}_2 = \frac{1}{7}$.

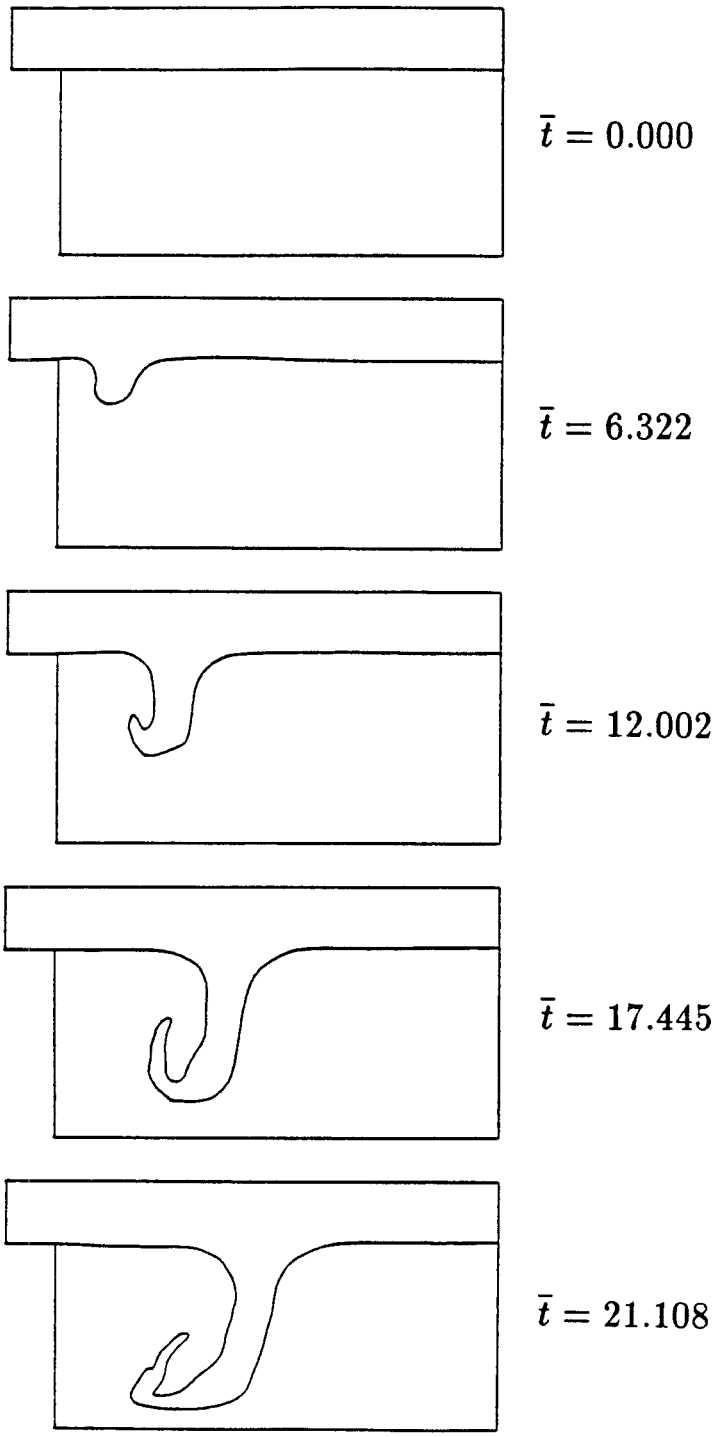

Figure (3.10) Flow Field Induced By the Surging Flow over the Rearward Facing Step for $\overline{u}_0 = 0.250$, $\overline{u}_1 = 0.247$ and $\overline{\rho}_2 = \frac{1}{7}$.

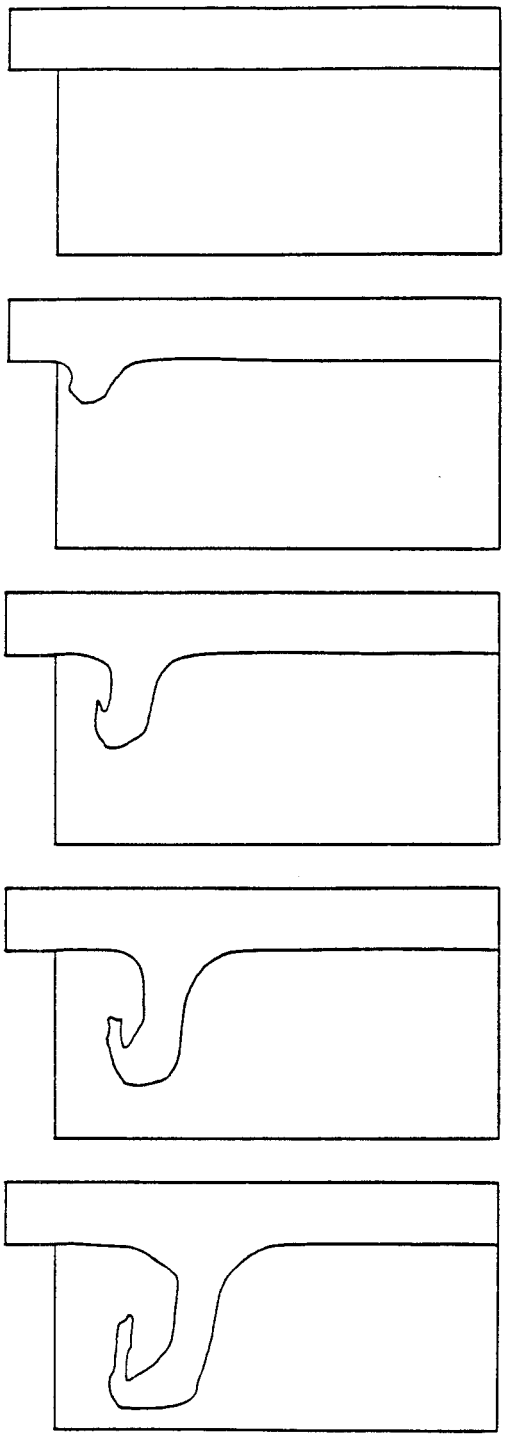

Figure (3.11) Flow Field Induced By the Surging Flow over the Rearward Facing Step for $\overline{u}_0 = 0.0625$, $\overline{u}_1 = 0.247$ and $\overline{\rho}_2 = \frac{1}{7}$.

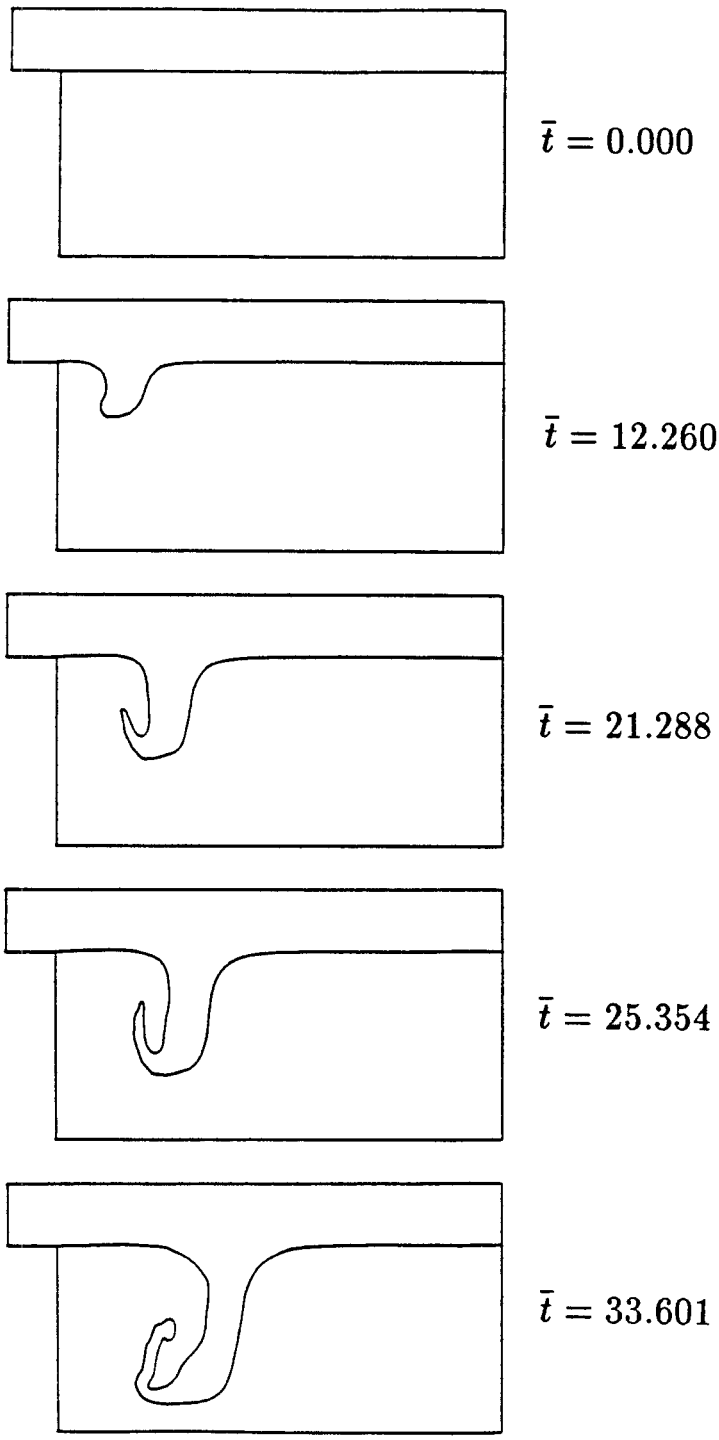

Figure (3.12) Flow Field Induced By the Surging Flow over the Rearward Facing Step for $\overline{u}_0 = 0.125$, $\overline{u}_1 = 0.182$ and $\overline{\rho}_2 = \frac{1}{7}$.

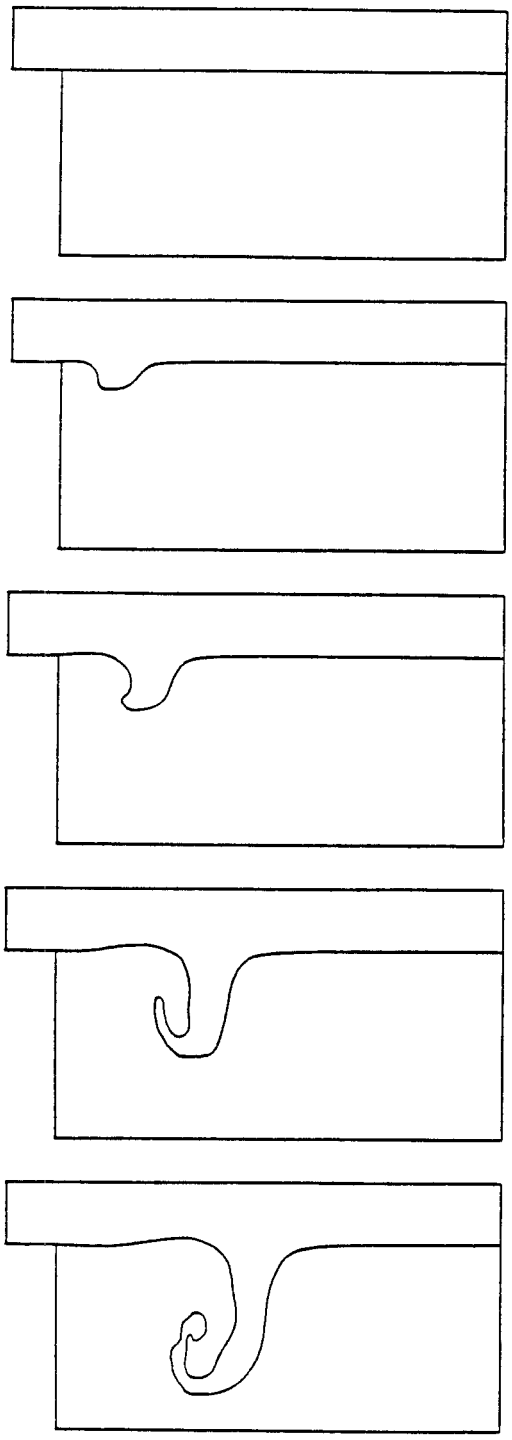

Figure (3.13) Flow Field Induced By the Surging Flow over the Rearward Facing Step for $\overline{u}_0 = 0.125$, $\overline{u}_1 = 0.0686$ and $\overline{\rho}_2 = \frac{1}{7}$.

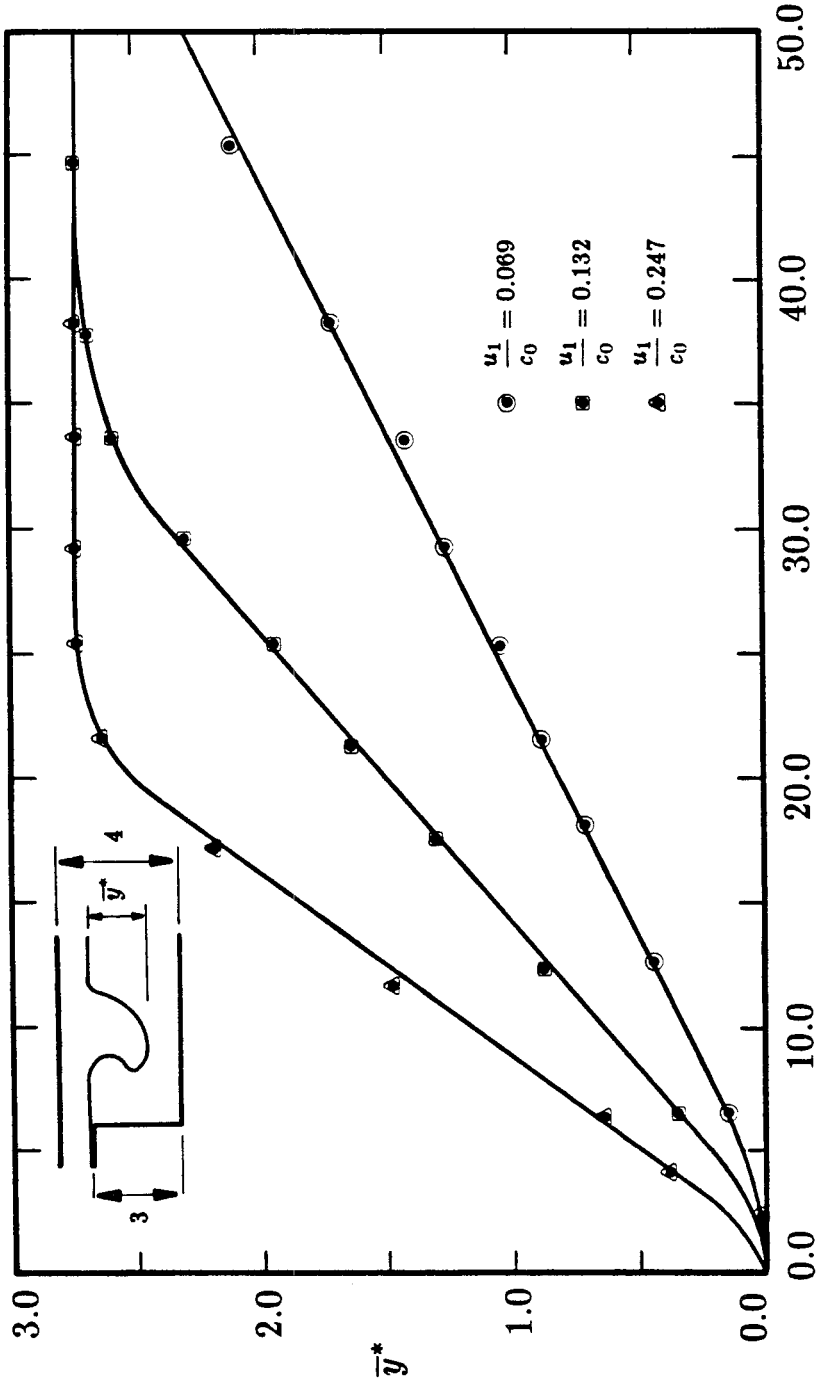

Figure (3.14) Position of the Lower Extremity of the High Density Fluid as a Function of the Dimensionless Time, $\bar{t}$ for $\bar{\rho}_2 = \frac{1}{7}$.

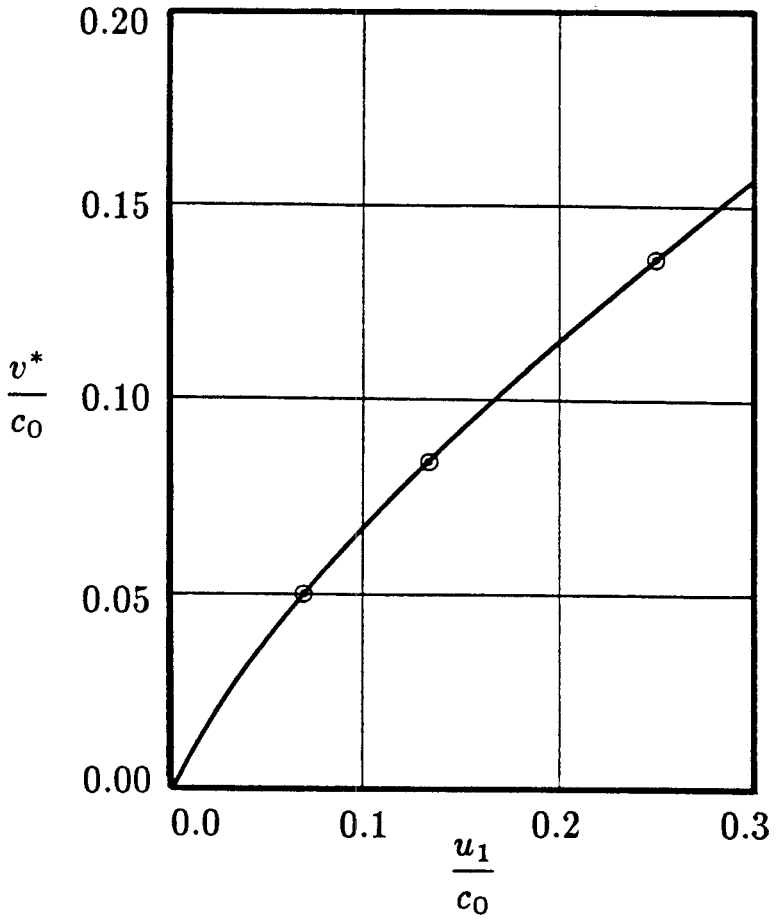

Figure (3.15) Dimensionless Vertical Velocity of the Lower Extremity of the High Density Fluid as a Function of the Dimensionless Surge Velocity, $\frac{u_1}{c_0}$ for $\overline{\rho} = \frac{1}{7}$.

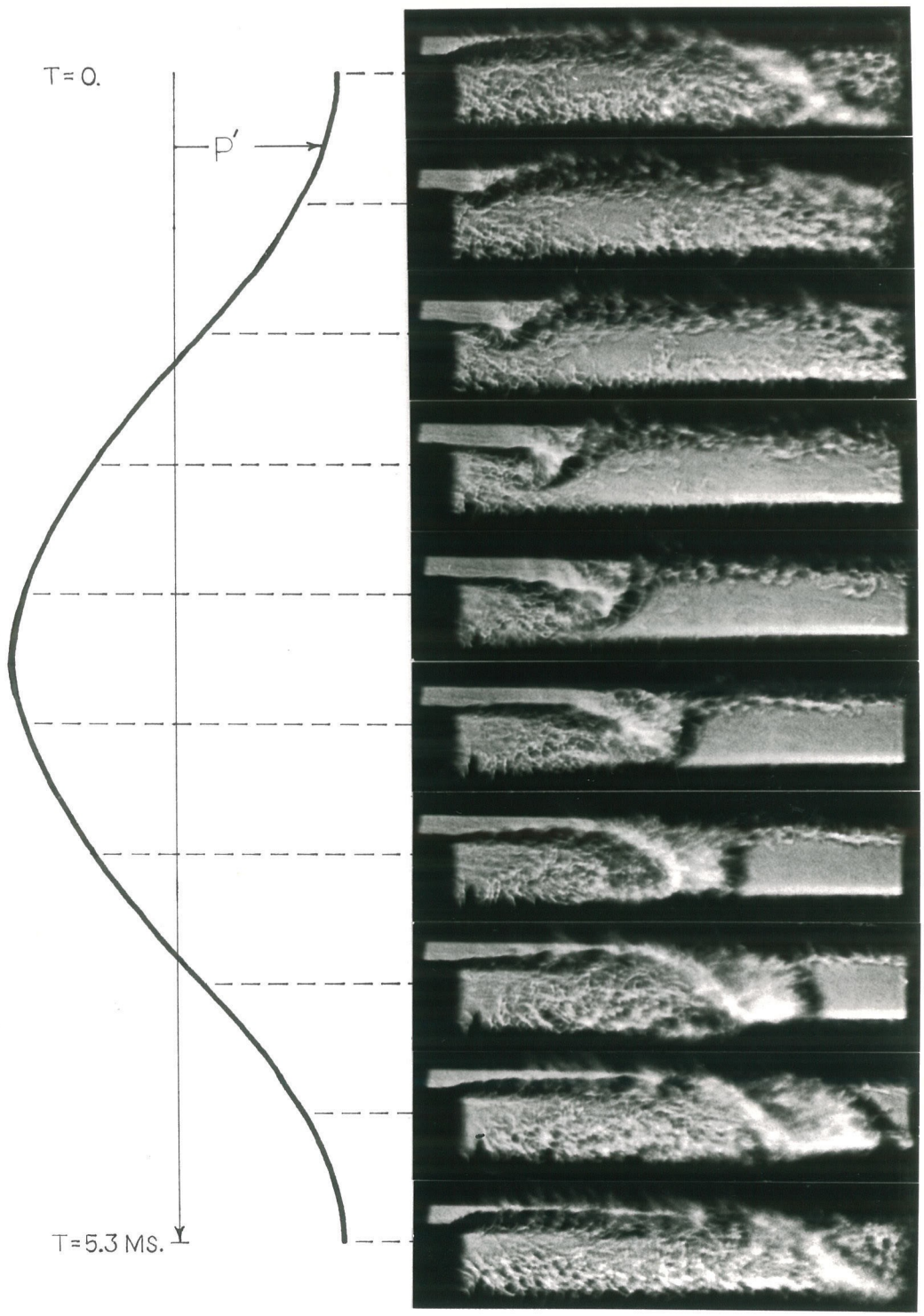

Figure (3.16) Vortex Evolution in the Combustion Chamber (188Hz).

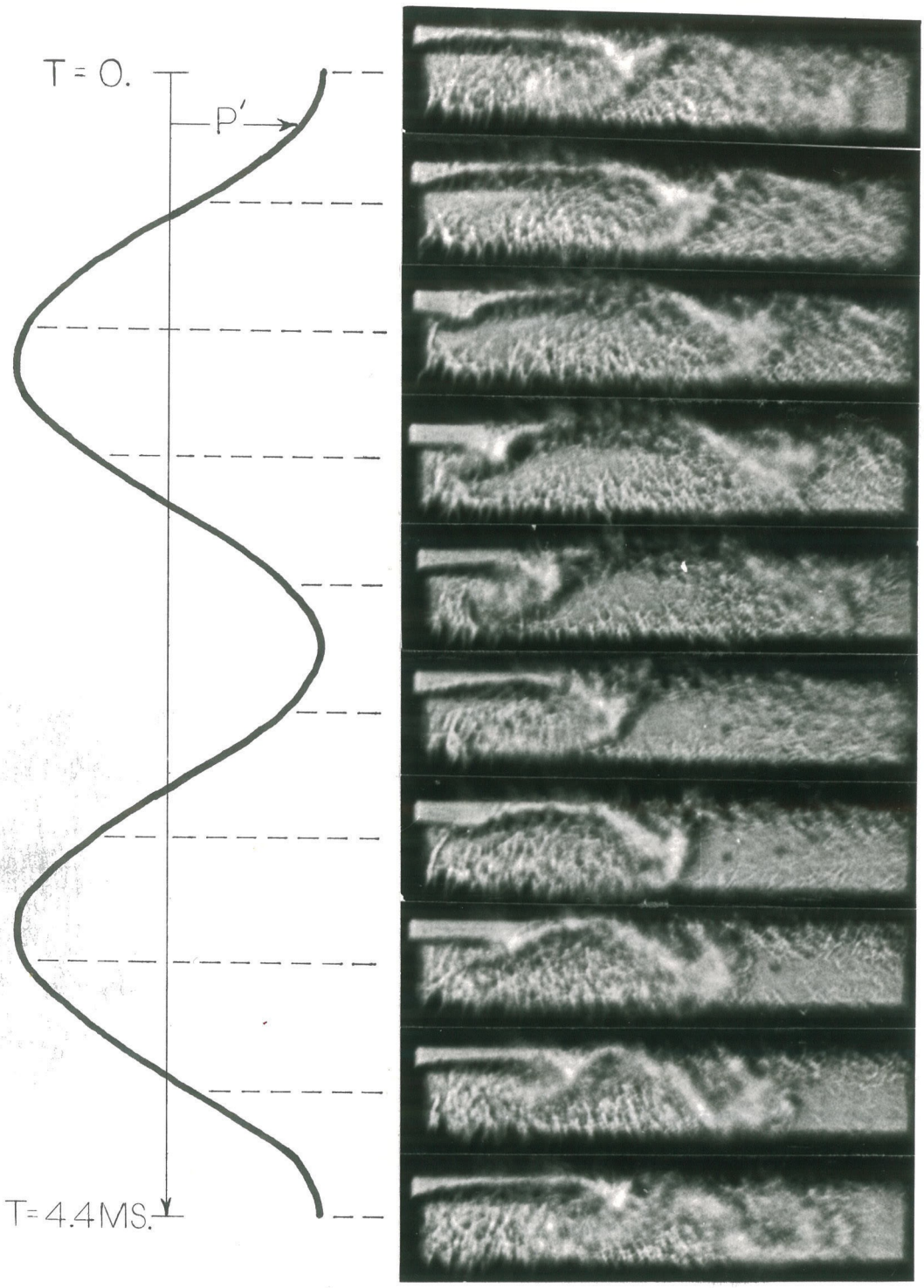

Figure (3.17) Vortex Evolution in the Combustion Chamber (446Hz).

Chapter 4

Concluding Remarks

Instabilities in combustion systems are sustained when the largest proportion of the heat release associated with the fluctuating combustion process occurs at a time close to the maximum of the pressure oscillation. A certain, appropriate phase difference therefore has to exist between the pressure oscillation and the fluctuating heat release. In the combustion system under consideration, the velocity fluctuation associated with the pressure oscillation causes a surging flow over the rearward facing step flameholder. The present study confirms that this surging flow causes the formation of a large vortex structure in the combustion chamber. The vortex induces a motion of the reactant toward the lower wall of the chamber. After the reactant impinges against the lower wall, it mixes vigorously with the hot combustion products present in the chamber, and reacts violently after a certain delay time associated with the chemical reaction kinetics. The heat release associated with the violent reaction reinforces the pressure oscillation if the two have the appropriate phase relationship. Very little combustion occurs before the reactant impinges against the lower wall. The time delay causing the phase difference between the pressure and combustion fluctuations is therefore derived from two processes; the motion of the reactant toward the lower wall, and the chemical reaction. The time delay associated with the chemical reaction kinetics is a function of the fuel–air equivalence ratio and is independent of the fluid mechanics of the flow field. It will therefore be assumed constant in the present discussion.

Results of the experimental study suggest that a certain vortex shedding frequency has a certain, constant pressure fluctuation magnitude associated with it. The magnitude is different for different shedding frequencies, higher frequencies generally corresponding to larger magnitudes. At present, the way in which these magnitudes are determined is not well understood, but the results of the present study suggest a possible mecha-

nism. The study has shown that the time delay associated with the motion of the vortex toward the lower wall decreases as the surge velocity (and therefore the magnitude of the pressure oscillation) is increased. Now if an acoustic analysis is done on the system, the heat release associated with the chemical reaction could be represented by a forcing function in the acoustic equations. Because the delay time associated with the heat release is determined, in part, by the magnitude of the pressure oscillation, a non–linear coupling exists between the pressure oscillation and the forcing function. This coupling could cause the pressure oscillation to reach a limit cycle in the following way. If the pressure oscillation starts off with a magnitude too large for a particular frequency, the time delay would be too small for the forcing function to have the appropriate phase relationship with the pressure oscillation for the oscillation to be sustained at that particular magnitude. The pressure fluctuation would therefore decrease in magnitude, and the delay time would show a corresponding increase until the forcing function and the pressure oscillation have the appropriate phase relationship for pressure oscillations of constant magnitude to be sustained. On the other hand, if the magnitude of the fluctuating pressure drops below this critical value, the time delay would increase. This would cause a phase relationship between the forcing function and the pressure oscillation that would feed energy into the system, increasing the magnitude of the pressure oscillation, and forcing it back to the limit cycle associated with that particular frequency. Because a higher instability frequency would need a shorter delay time for oscillations of constant magnitude to be sustained, the magnitude of the pressure oscillation associated with that limit cycle would be larger. This is in agreement with experimental observations.

5. References

Boris, J.P. and Book, D.L. (1973), Flux–Corrected Transport. 1.Shasta, A Fluid Mechanic Algorithm That Works, *Journal of Computational Physics*, **11**, 38

Boris, J.P., Book, D.L. and Hain, K. (1975), Generalizations of the Flux–Corrected Transport Technique, *Journal of Computational Physics*, **18**, 248

Gangi, A.T., and Sawyer, R.F. (1982), Turbulence, Combustion, Pollutant and Stability Characterization of a Premixed, Step Combustor, *NASA Contract Report 3230*

Keller, J.O., Vaneveld, L., Korschelt, D., Hubbard, G.L., Ghoniem, A.F., Daily,J.W. and Oppenheim, A.K. (1982), The Mechanism of Instabilities in Turbulent Combustion Leading to Flashback, *AIAA Journal*, **29**, 254

Liepmann, H.W. and Roshko, A. (1957), *Elements of Gasdynamics,* Wiley, New York, N.Y., Chapter 3

Pullin, D.I. (1978), The Large–Scale Structure of Unsteady Self–Similar Rolled–up Vortex Sheets, *Journal of Fluid Mechanics*, **88**, 401

Roache, P.J. (1972), *Computational Fluid Dynamics,* Hermosa Publishers, Albuquerque, N.M., 155

Rogers, D.E. and Marble, F.E. (1956), A Mechanism for High–Frequency Oscillations in Ramjet Combustors and Afterburners, *Jet Propulsion*, **26**, 456

Smith, D.A. (1985), An Experimental Study of Acoustically Excited, Vortex Driven, Combustion Instability within a Rearward Facing Step Combustor, *Ph.D Thesis, California Institute of Technology*

Smith, D.A. and Zukoski,E.E. (1985), Combustion Instability Sustained by Unsteady Vortex Combustion, *AIAA/SAE/ASME/ASEE 21st Joint Propulsion Conference, AIAA Paper No. 85-1248*

Vaneveld, L., Hom, K. and Oppenheim, A.K. (1984), Secondary Effects in Combustion Instabilities Leading to Flashback, *AIAA Journal*, **22**, 81